Karlsruhe Institute of Technology

Negative Momentum Compaction Operation and its Effect on the Beam Dynamics at the Accelerator Test Facility KARA

Zur Erlangung des akademischen Grades eines
DOKTORS DER NATURWISSENSCHAFTEN (Dr. rer. nat.)

von der KIT-Fakultät für Physik des
Karlsruher Instituts für Technologie (KIT)
genehmigte

DISSERTATION
von

M.Sc. Patrick Schreiber
aus Horb a.N.

Tag der mündlichen Prüfung:	10.06.2022
Referentin:	Prof. Dr. Anke-Susanne Müller
Korreferent:	Prof. Dr. Günter Quast

Contents

1 Introduction

The concept of negative momentum compaction operation of synchrotron light sources is a scarcely explored area in accelerator physics. The research in this thesis investigates the effects on the electron beam and examines benefits as well as shortcomings of this regime with regard to the ever evolving development of advanced synchrotron light sources. The so-called synchrotron radiation, electromagnetic radiation ranging from microwave to X-ray frequencies, is an important tool for research spanning a vast set of scientific disciplines. There are applications in material science, solid state physics, geology, medicine and many more research fields. Synchrotron light sources are particle accelerators dedicated to the production of this remarkable radiation. These machines exploit the fact that charged particles accelerated almost to the speed of light emit electromagnetic radiation. Due to their small mass, electrons radiate about 2000 times the power emitted by protons in a comparable accelerator and therefore synchrotron light sources use electrons as the particle of choice. It is no surprise that these accelerators are under active development to continuously improve the quality of the produced radiation in many aspects such as brightness, pulse duration, beam divergence and photon energy. Existing concepts are reaching their limits. While the intensity and spectrum can be improved with so-called insertion devices, reducing the source size requires improvements to the properties of the electron beam and therefore the magnetic lattice. One new approach is the usage of so-called multi-bend achromats [1], where each bending magnet is split into multiple magnets, leading to a more complex magnetic lattice. This has the potential to reduce the emittance of the electron beam and therefore increase the brilliance of the light beam. However, the downside of these structures is the necessity of strong sextupole magnets in order to correct chromatic aberrations (described by a parameter called chromaticity). These magnets introduce non-linear magnetic fields, that disturb the harmonic oscillations of the electrons. Especially at high magnet strengths, these non-linearities gain importance as they reduce the transverse area of stable beam storage. It would, in principle, be possible to drop the requirement of a slightly positive chromaticity. However, when the momentum compaction factor, a longitudinal parameter describing the energy dependence of the path length, and

the chromaticity possess opposite signs an instability called head-tail instability can arise leading to the loss of the stored electrons. Therefore, in order to safely operate with weaker sextupole magnets resulting in a negative chromaticity an optics with a negative momentum compaction factor has to be employed. Until now, operation with this condition has only scarcely been implemented in synchrotron light sources [2, 3, 4]. In order to qualify this mode as a valid option, it has to be tested further, and the implications have to be investigated.

With this in mind, an optics with a negative momentum compaction factor has been implemented in the course of this thesis for the first time at the Karlsruhe Research Accelerator (KARA) and the effects on beam dynamics have been investigated. The flexibility in terms of optics and available time slots for accelerator development as well as a multitude of available beam diagnostics devices render KARA, the electron synchrotron of the KIT light source located in Karlsruhe, an ideal environment for such studies.

To start off, the physics background and accelerator physics basics are introduced in Chapter 2. Furthermore, some concepts from transverse beam dynamics are explained followed by an introduction into the momentum compaction factor and phase focusing, which plays a vital role in steps necessary to implement the desired negative momentum compaction optics. Synchrotron radiation, radiation damping and the concepts of wakefields and impedances are introduced in this chapter as well. The implementation of the new optics with a negative momentum compaction factor is laid out in Chapter 3 together with a detailed description of the used strategy and an introduction to KARA. Also, as comparison to the new optics, existing standard and low momentum compaction factor operation modes are described and considerations of the beam energy as well as the energy ramping procedure, relevant for e.g. improved stability and beam lifetime, are presented. In Chapter 4 observed properties of the beam during operation with the newly implemented optics are reported including measurements to the second order of the momentum compaction factor, beam and bunch current limits as well as lifetime limitations. The tools and methods used for studies in this thesis are described in Chapter 5 introducing especially the measurement devices and techniques.

A validation on the head-tail evasion with negative momentum compaction factors and a negative chromaticity is given in Chapter 6 based on measurements of the horizontal beam position after a horizontal kick. Differences of the beam dynamics are predicted to manifest in a changed current-dependent behaviour of the bunch length. Therefore, studies of the current-dependent bunch length in the new mode were conducted and are presented in Chapter 7 together with a comparison to the

bunch length at positive momentum compaction factors including simulations based on collective effects. Finally, as measurements of the temporal variation in the emitted intensity in the THz frequency range can be used as indicator for the longitudinal beam dynamics, such measurements were used in Chapter 8 to investigate an arising longitudinal instability. Detailing similarities and differences in the behaviour at positive and negative momentum compaction factors in terms of instability threshold current, temporal behaviour and current dependency of the observed intensity fluctuations. Furthermore, the energy dependent behaviour is observed as well as the arrival time changes of the emitted synchrotron radiation pulses. Last but not least the emitted radiation intensities between the two signs of the momentum compaction factor during the instability are compared.

The expected differences in beam dynamics based on the measurements presented in the previous chapters during operation in the new optics are summed up in Chapter 9. Finally, a conclusion is drawn on the difficulties and challenges that have to be expected when implementing operation modes with negative momentum compaction factors and the potential benefits of such a mode for the operation of a synchrotron light source are highlighted.

2 Physics Background

Accelerator physics is a wide field based on fundamental concepts. This chapter aims to give a brief insight into the concepts relevant to this thesis. First a short overview over the basic physics behind particle accelerators is given. This is followed by an introduction to the most important concepts for this thesis, the momentum compaction factor and the longitudinal phase space. Subsequently, synchrotron radiation and important associated quantities are discussed followed by the description of radiation damping and other longitudinal parameters. Last but not least the interaction of a particle with its surrounding is described based on the concept of wakefields and impedances. As this thesis was conducted at the synchrotron light source KARA[1], this chapter focuses on ultrarelativistic electrons.

2.1 Basics of Accelerator Physics

This section outlines the basic physics behind charged particle acceleration [5, 6]. These particles are accelerated using electromagnetic fields. The force exerted by these fields on a particle is described by the Lorentz force [7]

$$\vec{F}_{\mathrm{L}} = \frac{d\vec{p}}{dt} = q\left(\vec{E} + \vec{v} \times \vec{B}\right) \tag{2.1}$$

with the momentum $\vec{p}$, the electric field $\vec{E}$, magnetic field $\vec{B}$, charge q and velocity $\vec{v}$. The force of a magnetic field on a particle is perpendicular to the movement direction and no energy gain can be achieved from magnetic fields. Therefore, electric fields are used for the acceleration, while magnetic fields are used for deflection and focusing. During this acceleration a particle gains the energy

$$E_{\mathrm{gain}} = \int_{\vec{r}_1}^{\vec{r}_2} \vec{F}_{\mathrm{L}} d\vec{r} = \int_{\vec{r}_1}^{\vec{r}_2} q\left(\vec{E} + \vec{v} \times \vec{B}\right) d\vec{r} = q \int_{\vec{r}_1}^{\vec{r}_2} \vec{E} d\vec{r} = q \cdot V \tag{2.2}$$

when moving from point $\vec{r}_1$ to point $\vec{r}_2$ with the acceleration voltage V.

[1] An introduction to KARA is given in Section 3.1

Historically, acceleration was achieved by static electric fields. However, soon the achievable field gradients did not provide enough energy for the particles. The solution was the usage of high frequency (radio frequency (RF)) electromagnetic fields. In linear accelerators this was achieved by using drift tubes. These tubes ensure the particles only experience the electric fields at phases where the field points in the correct direction by shielding the electric field for at least half a period of the high frequency. As the particles gain energy and speed the drift tubes need to increase in length with increasing particle speed. The energy gain of such an accelerator depends on the number of drift tubes which for high energies results in a large and expensive accelerator. This can be circumvented by using circular accelerators which use the same accelerating structure multiple times, once for each revolution. However, the radius of the particle trajectories increases with increasing momentum. To avoid large magnets that would allow for variable bending radii, the concept of synchrotrons can be used. In these accelerators the magnetic field strength is increased synchronously to the momentum of the particles which effectively keeps the radius constant. For some use-cases the machine only needs to operate at a fixed energy. These machines are called storage rings, as they store particles at a certain energy, and consist mostly of the same components used in synchrotrons. Here the particles only gain the energy they loose over one revolution.

Using RF electromagnetic fields it is not possible to accelerate or store a continuous stream of particles. In order to store a particle it needs to be supplied with a certain amount of energy. Too much or too little energy would result in this particle getting lost due to e.g. collisions with the vacuum chamber wall, as the particle guidance is designed for a certain particle energy. Since the field strength oscillates, only certain phases of the accelerating field supply the particles with the necessary energy.

It is, however, possible to perpetually accelerate a particle in a certain range of phases even though the particle might not exactly gain the same amount of energy that it lost. These ranges in phase for which acceleration is possible are called RF buckets. In these buckets, packets of particles are accelerated which are called bunches. The oscillating RF field is provided by so-called cavities.These are mostly hollow structures optimised for a certain resonance frequency of the RF fields. At each revolution the bunch needs to arrive at the same phase. If the frequency of the accelerating field matches the revolution frequency of particles this is only given for one single bunch. If however the RF frequency is a multiple of the revolution frequency multiple bunches can be used. This introduces the harmonic number

$$h = \frac{f_{\mathrm{RF}}}{f_{\mathrm{rev}}} \tag{2.3}$$

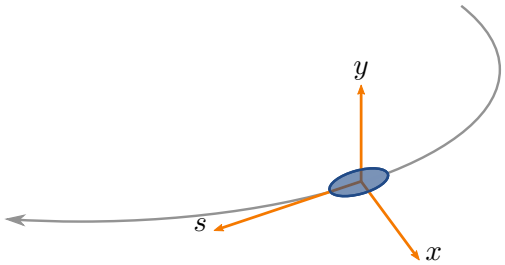

Figure 2.1: Depiction of the coordinate system used in accelerator physics.

with the RF frequency f_{RF} and the nominal revolution frequency f_{rev}. This number also defines the number of buckets and therefore the maximal possible number of bunches. The actual number of stored particles is often expressed via the beam current

$$I = \frac{Q}{t_{\mathrm{rev}}} = \frac{qNv}{C} \tag{2.4}$$

with the total charge Q, the single particle charge q, the revolution time t_{rev}, the number of particles N and the ring circumference C. For a lot of effects only the number of particles in a bunch N_{b} is important and thus the bunch current is used

$$I_{\mathrm{b}} = \frac{Q_{\mathrm{b}}}{t_{\mathrm{rev}}} = \frac{qN_{\mathrm{b}}v}{C}. \tag{2.5}$$

In Eq. (2.1) the force on a particle exerted by a magnetic field is enhanced by the factor c compared to the force exerted by an electric field. The Lorentz force therefore suggests a much more effective deflection by magnetic fields compared to electric fields. Thus, conventional accelerators use magnetic fields for beam guidance. The bending radius of a charged particle in a magnetic field is given by the equality of the centripetal force and the perpendicular part of the Lorentz force

$$\frac{mv^2}{R} = qvB \tag{2.6}$$

where R is the bending radius. This leads to

$$R = \frac{mv}{qB} = \frac{p}{qB}. \tag{2.7}$$

In accelerator physics mostly a right handed moving coordinate system is used. The origin is located at the position of the synchronous particle, which is the particle that gains exactly the same amount of energy it looses during one turn. A schematic of the coordinate system is shown in Fig. 2.1. The three coordinates are longitudinal s, horizontal x (plane of circular movement) and vertical y. The orbit of a particle is the path it takes around a circular accelerator.

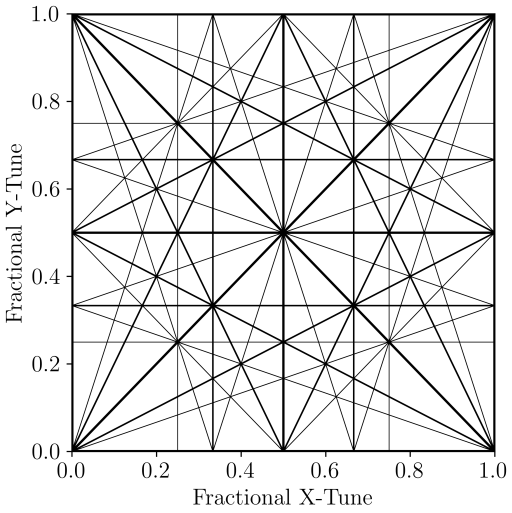

Figure 2.2: Tune resonances up to order 4.

2.2 Transverse Beam Dynamics

In order to prevent an uncontrolled transverse beam size increase the bunch is focused with quadrupole magnets. These magnets focus the beam transversally via a linear spacial gradient of the magnetic field. Thereby particles with a large deviation from the design orbit are deflected more strongly than particles with a small deviation.

The usage of focusing systems causes a transverse oscillation around the design orbit with a specific oscillation period. The number of oscillations per revolution in the horizontal and vertical plane is called vertical and horizontal tune Q respectively [5]

$$Q = \frac{1}{2\pi} \oint \frac{ds}{\beta(s)}, \tag{2.8}$$

where $\oint$ describes the integral over one revolution in the accelerator and $\beta(s)$ is the beta function which describes the shape of the transverse envelope of all particle trajectories in the accelerator. For stable operation the tune is kept at a non-integer number. This makes sure that kicks at one position in the ring, e.g. from unwanted magnetic fields, do not result in beam loss from in-phase kicks adding up. There are certain combinations of vertical and horizontal tune that result in such a resonances of varying strength

$$mQ_x + nQ_y = p \quad m, n, p \in \mathbb{Z} \tag{2.9}$$

where $|m| + |n|$ is the order of the resonance and generally the lower the order, the more severe the resonance is to the beam. The corresponding resonance lines up to the fourth

order are plotted in Fig. 2.2.

Since the effect of a magnetic field on a particle is also dependent on the particle's energy, the focusing strength of focusing magnets is not the same for each particle. This introduces focusing errors described by the chromaticity

$$\xi = Q' = p_0 \frac{dQ}{dp} \approx \frac{\Delta Q}{\Delta p/p}. \tag{2.10}$$

This is directly given by the change in tune for a change in particle momentum. The natural chromaticity without corrections in a storage ring is typically a large negative value. To control the chromaticity sextupole magnets can be added to the accelerator. The tune shift caused by the chromaticity for particles with a certain energy offset could cause these particles to reside on a tune resonance and the particles could subsequently be lost.

Equation (2.7) shows the dependence of the bending radius on the momentum of particles. As each particle has a slightly different momentum this results in slightly different particle paths. The offset of a particle from the design orbit (blue in Fig. 2.3) is described by the dispersion function $D(s)$

$$\Delta x = D(s) \cdot \frac{\Delta p}{p}. \tag{2.11}$$

The dispersion function grows in homogeneous magnetic fields such as in dipole magnets used for keeping the particles on a circular path. Magnets with a gradient in the magnetic field, however, can focus the particles and reduce the dispersion. Therefore, the dispersion can be modified which is exploited when varying the momentum compaction factor as seen in the next section.

2.3 Momentum Compaction Factor and Phase Focusing

Due to the dispersion each particle follows a different orbit resulting in a different path length for one revolution as shown in Fig. 2.3 on the left side. The relation between an offset in relative path length and an offset in relative momentum is called the momentum compaction factor [5]

$$\alpha_c = \frac{\frac{\Delta L}{L_0}}{\frac{\Delta p}{p_0}} \tag{2.12}$$

where L_0 is the nominal path length of the synchronous particle and p_0 the momentum of the synchronous particle, the particle which gains exactly the same amount of energy

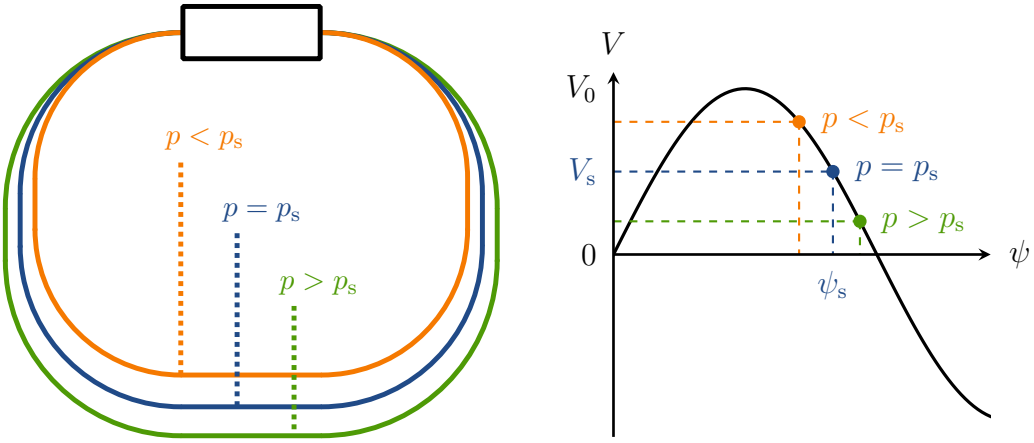

Figure 2.3: Sketch of the path dependence on momentum for a positive momentum compaction factor on the left side. Accelerating voltage and phases of particles with different momenta for a positive momentum compaction factor that result in phase focusing on the right. Particles with higher momenta travel on longer paths and arrive later in the cavity receiving less energy and vice versa.

as it has lost per turn. The momentum compaction factor can also be expressed in terms of the dispersion function

$$\alpha_c = \frac{1}{L_0} \oint \frac{D(s)}{R(s)} ds. \tag{2.13}$$

As the dispersion without additional focusing efforts in a circular accelerator is positive the "natural"[2] momentum compaction factor is positive as well.

The principle behind the momentum compaction factor inflicts an additional constraint on the possible phase of the synchronous particle for stable operation. This can be derived from the movement of particles around the synchronous phase as follows and is called phase focusing. The synchronous particle travels with a fixed path length and requires a fixed time for one revolution. Therefore, it always arrives at a fixed phase in the cavity, called the synchronous phase ψ_s. This phase corresponds to an energy gain that is equivalent to the loss of energy during one turn per particle. Due to the offset in path length and the fact that ultrarelativistic electrons move with approximately $v \approx c$ independent of the momentum, a change in momentum leads to an offset in arrival time and phase in the accelerating cavity. As noted before not every phase is suitable to accelerate a bunch of particles. For stable operation of a circular accelerator the synchronous phase is the phase, for which particles with higher momenta gain less energy in a cavity, since they arrive later, and vice versa for particles with less momentum. For

[2] Without focusing elements.

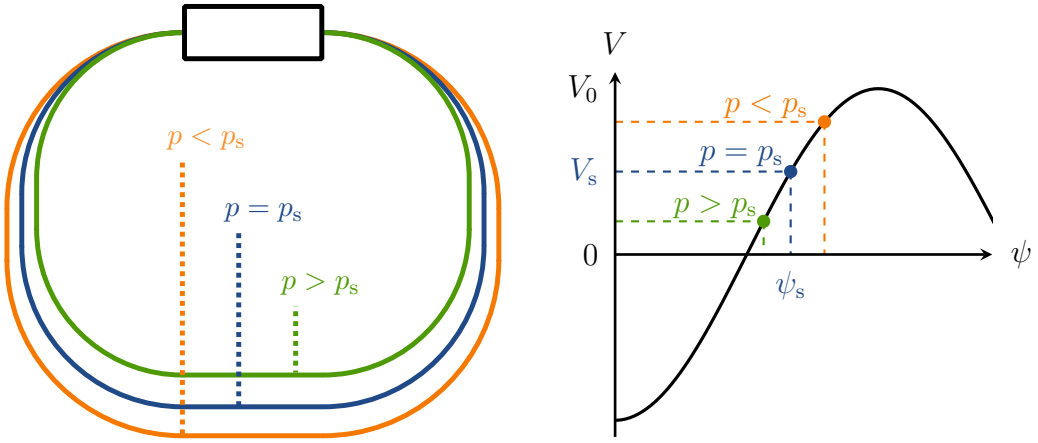

Figure 2.4: Sketch of the path dependence on momentum for a negative momentum compaction factor on the left. Accelerating voltage and phases of particles with different momenta for a negative momentum compaction factor that result in phase focusing on the right. Particles with higher momenta travel on longer paths and arrive later in the cavity receiving less energy and vice versa.

a positive value of α_c this is achieved by choosing the phase of the synchronous particle on the falling edge of the RF field. This is depicted in Fig. 2.3 on the right side. The momenta of off-momenta particles thus effectively approach the design momentum. This effect results in a net focusing and is therefore called phase focusing.

The momentum compaction factor can be altered by changing the dispersion through changes to the strengths of focusing magnets. Through these focusing magnets particles with momentum greater than the synchronous particle can be pushed to the inside of the design orbit (orbit of the synchronous particle). This results in a negative displacement and therefore a negative dispersion. If the negative contribution of the dispersion to the integral in Eq. (2.13) prevails the momentum compaction factor is negative. This means that particles with less momentum travel on longer paths and vice versa as sketched in Fig. 2.4 on the left side.

When switching from positive to negative α_c while keeping the phase of the bunch phase focusing would not be possible. Particles with a momentum surplus would arrive earlier and gain even more energy at the cavity. This would result in a longitudinal defocusing effect and ultimately in particle loss. Therefore, the acceleration phase for negative α_c is chosen on the rising edge of the RF voltage as seen in Fig. 2.4 on the right side. This way particles with a momentum surplus still arrive earlier but gain less energy than the synchronous particle which results again in phase focusing. The phase shift compared to positive α_c is roughly $\Delta\psi \approx \pi$. The exact phase for the synchronous

particle in a pure storage ring is given via the energy loss per turn (for a sinusoidal RF voltage) so the particle gains exactly the same energy it lost over one revolution

$$\psi_s = \pi - \arcsin\left(\frac{U_0}{eV_0}\right) \tag{2.14}$$

where U_0 is the energy loss per turn and particle, see Section 2.5. A phase shift of exactly π would result in a negative value of the RF voltage experienced by the synchronous particle. Therefore, the necessary shift in reference to positive α_c is slightly less than π

$$\psi_s|_{\alpha_c<0} = \psi_s|_{\alpha_c>0} - \Delta\psi \tag{2.15}$$

$$\Delta\psi = \pi - 2 \cdot \arcsin\left(\frac{U_0}{eV_0}\right). \tag{2.16}$$

2.4 Longitudinal Phase Space

The longitudinal phase space is the space spanned by longitudinal space and energy coordinates. It can be used to study the development of position and energy of a particle as well as the development of a bunch of particles. In the absence of perturbations the motion of a particle in phase space depends only on the accelerating voltage and the momentum compaction factor. When only considering a linear accelerating voltage and first order momentum compaction factor the motion follows a harmonic oscillator given by the phase focusing. This motion can simply be described with Fig. 2.5. A particle starts with a random position in phase space, e.g. in position (a) when it is just after the cavity in the ring. When travelling around the ring it arrives later, for positive α_c, at the cavity since it has more energy than the synchronous particle. It will therefore move towards the tail of the bunch and in phase space to position (b) until it arrives just before the cavity in the ring. Since it gains less energy at this position in phase space when traversing the cavity it will lose energy relative to the synchronous particle and move to position (c) in phase space when it exists the cavity. By continuation of these steps a circular motion in phase space will be described. At negative α_c the rotation direction is reversed. Particles with more energy arrive earlier and gain less energy, due to the reversed RF voltage. The ensemble of particles in a bunch is often represented through a charge density. An example of the charge density of a bunch in the longitudinal phase space at negative α_c is shown in Fig. 2.6 for a simulation with a short bunch.

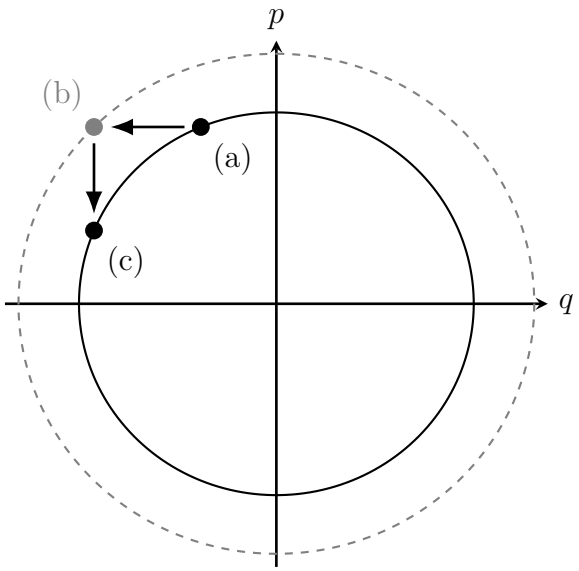

Figure 2.5: Motion of a particle in the longitudinal phase space without energy loss due to radiation. q and p are the canonical space and energy coordinates respectively. A particle starts at position (a), moves to position (b) and ends in position (c) after one revolution in the ring. Note: The grey dashed circle as well as the grey point (b) depict the phase space position of a particle at times just before entering the cavity. The solid black circle and points depict the phase space position of a particle at times just exiting the cavity.

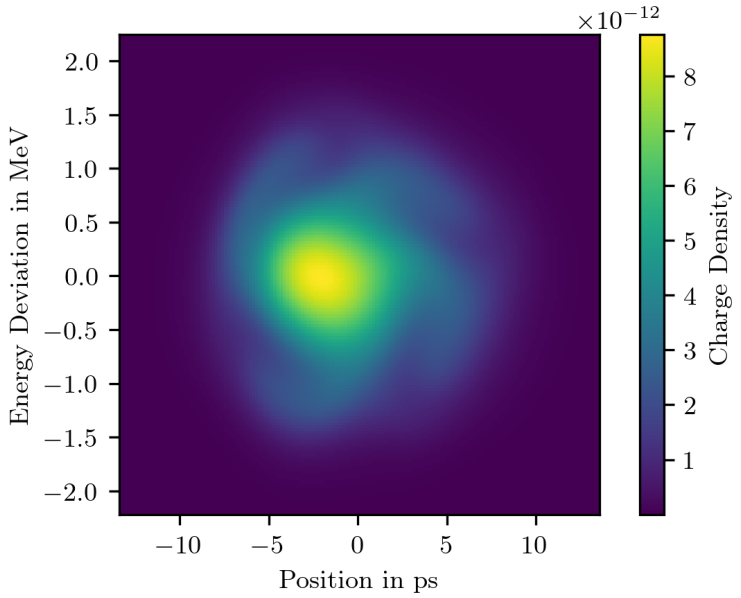

Figure 2.6: Example charge density in the longitudinal phase space at negative α_c for short bunches. The data was simulated with Inovesa [Sch19a].

2.5 Synchrotron Radiation

A charged particle that is accelerated, whether transversally or longitudinally, emits electromagnetic radiation. For the case of particles in an accelerator this radiation is called synchrotron radiation as it was first observed at a synchrotron. This thesis was performed at an electron accelerator and thus the following sections will mostly focus on the case of accelerated electrons. Longitudinal as well as transverse acceleration in a synchrotron leads to synchrotron radiation. The emitted power can be expressed for both acceleration planes individually [5]

$$P_{\mathrm{s}}^{\parallel} = \frac{e^2 c}{6\pi\varepsilon_0 (m_0 c^2)^2} \left(\frac{dE}{ds}\right) \tag{2.17}$$

for longitudinal acceleration and

$$P_{\mathrm{s}}^{\perp} = \frac{e^2 c}{6\pi\varepsilon_0 R^2} \left(\frac{E}{m_0 c^2}\right)^4 \tag{2.18}$$

for transverse acceleration with the vacuum permittivity ε_0. The radiated power for the longitudinal acceleration $P_{\mathrm{s}}^{\parallel}$ is not depending on the energy of particles, just on the acceleration gradient. The power for transverse acceleration $P_{\mathrm{s}}^{\perp}$, however, depends on the energy to the fourth power. Therefore, the radiation due to transverse acceleration prevails over the longitudinal acceleration.

Equation (2.18) also shows the dependence on the particle mass. With the ratio between the mass of an electron and a proton of $m_p/m_e \approx 1836$ it is clear why electrons are used in synchrotron light sources, especially considering the fourth power in Eq. (2.18).

The energy loss over a full turn in the accelerator is given as the integral of the momentary energy loss

$$U_0 = \oint P_{\mathrm{s}}^{\perp} dt = \frac{e^2 E^4}{3\varepsilon_0 R (m_0 c^2)^4}. \tag{2.19}$$

This means an energy loss of $U_0 \approx 45\,\mathrm{keV}$ for electrons at an energy of 1.3 GeV at KARA with a bending radius of $R = 5.559\,\mathrm{m}$.

For ultrarelativistic electrons the synchrotron radiation is emitted tangentially to the movement with a half opening angle of

$$\tan\Theta \approx \frac{1}{\gamma} \tag{2.20}$$

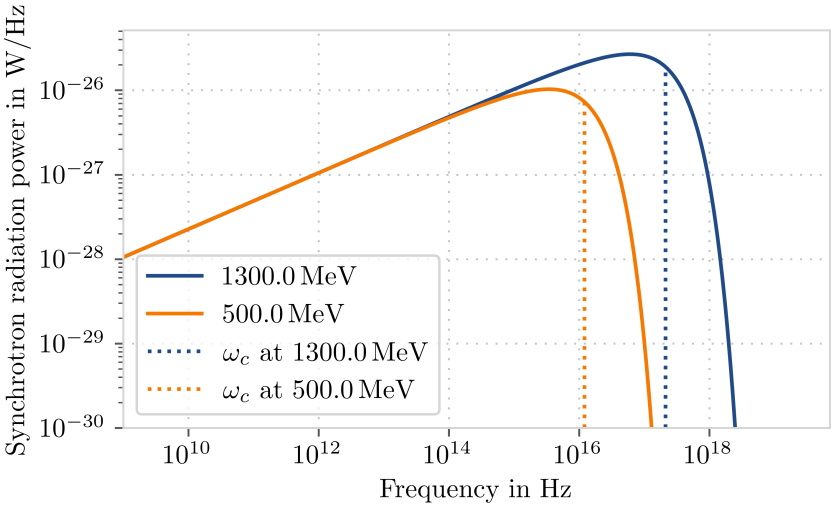

Figure 2.7: Spectrum of radiated synchrotron power of one electron at energies of 0.5 GeV and 0.5 GeV. Vertical dashed lines show the critical frequency ω_c at the respective energy.

with the Lorentz factor γ. For relativistic particles this simplifies to

$$\Theta \approx \frac{1}{\gamma} \tag{2.21}$$

which is a quite narrow emission cone. Together with the high speed of the particles this narrow cone results in a short light pulse seen by a static observer at a single point along the ring. This results in a broad frequency spectrum [8]

$$P(\omega) = \frac{P_s}{\omega_c} S\left(\frac{\omega}{\omega_c}\right) \tag{2.22}$$

with the critical frequency

$$\omega_c = \frac{3}{2}\frac{c\gamma^3}{R} \tag{2.23}$$

and the normalised spectral power density S

$$S(\zeta) = \frac{9\sqrt{3}}{8\pi}\zeta \int_{\zeta}^{\infty} K_{5/3}(\zeta^*)d\zeta^*. \tag{2.24}$$

$K_{5/3}$ here denotes a modified Bessel function [8]. The radiated spectrum can be seen in Fig. 2.7 calculated for energies of 0.5 GeV and 0.5 GeV with a bending radius of 5.559 m.

An additional effect is present for wavelengths longer than the emitting structure. In this case the radiation is emitted coherently and the power is amplified by the number

of emitting particles. The spectrum for the total emitted radiation is then [6]

$$P(\omega) = \underbrace{N P_\mathrm{s}(\omega)}_{\text{incoherent}} + \underbrace{N(N-1) F(\omega) P_\mathrm{s}(\omega)}_{\text{coherent}} \tag{2.25}$$

where $F(\omega)$ is the form factor obtained as the absolute squared Fourier transform of the normed longitudinal charge distribution. This shows the linear dependency of the incoherent power on the number of particles and the squared dependency of the coherent power. Due to the nature as Fourier transformed bunch profile, the form factor only contains significant values for frequencies where the bunch profile contains structures with the corresponding size. The presence of the form factor in Eq. (2.25) therefore implicates the emission of coherent radiation only for shorter structures than the wavelength of the radiation.

2.6 Radiation Damping and Longitudinal Parameters

In an electron storage ring the emission of synchrotron radiation leads to effects, that damp the particle motion with respect to the synchronous particle. Particles radiate tangentially to their path and therefore lose momentum in the longitudinal as well as transverse direction. In the cavities, however, they are accelerated purely longitudinally. This means the transverse component of the particle momentum is reduced. This effect is called transverse radiation damping and is dependent on the ratio between the particle momentum and the loss due to radiation.

In the longitudinal direction a similar mechanism exists. From Eq. (2.18) it follows that particles with different momenta radiate a different amount of power. This means particles with a surplus of momentum lose more than particles with a deficit. The longitudinal momentum differences get damped down similar to the transverse case.

Both damping mechanisms depend on the same basic principle of radiated power. The characteristic damping time

$$A_i = A_{i,0} e^{-t/\tau_{\mathrm{d},i}}, \tag{2.26}$$

where A_i is the amplitude and $i \in \{x, y, s\}$ is the direction of the momentum offset, can be expressed as [8]

$$\frac{1}{\tau_{\mathrm{d},i}} = \frac{1}{2t_\mathrm{rev}} \frac{U_0}{E_0} \cdot J_i \tag{2.27}$$

where J_i is the so-called damping partition number. For the longitudinal plane the damping partition number is roughly[3] $J_s \approx 2$ and in the transverse plane $J_{\{x,y\}} \approx 1$. Therefore, the longitudinal damping is about twice as strong as the transverse one.

From the effects of damping and phase focusing the longitudinal equation of motion can be derived [9]

$$\Delta\ddot{E} + \frac{2}{\tau_\mathrm{d}}\Delta\dot{E} - \omega_\mathrm{s}^2\Delta E = 0 \tag{2.28}$$

with the synchrotron frequency

$$f_\mathrm{s} = \frac{\omega_\mathrm{s}}{2\pi} = f_\mathrm{rev}\sqrt{-\frac{\alpha_\mathrm{c} h e V_0 \cos\psi_\mathrm{s}}{2\pi E}}. \tag{2.29}$$

The synchrotron frequency is the frequency of longitudinal particle oscillations around the synchronous phase.

The natural bunch length describes the longitudinal size of an almost zero current bunch. Mostly it is given as either standard deviation or full width half maximum of the longitudinal charge distribution. It results from the equilibrium between radiation damping, excitation due to the statistical emission of photons and therefore energy loss, and the energy gain in the cavities [10]

$$\sigma_{\mathrm{z},0} = \frac{c\sigma_{\delta,0}|\alpha_\mathrm{c}|}{2\pi f_\mathrm{s}\beta} \tag{2.30}$$

where $\sigma_{\delta,0}$ is the natural energy spread, which is the equivalent to the natural bunch length for the charge distribution in the energy dimension of the longitudinal phase space. While the natural bunch length is mostly given as absolute value the natural energy spread is often expressed as relative quantity $\sigma_{\delta,0} = \frac{\sigma_{E,0}}{E_0}$. The natural bunch length can be also expressed by using the synchrotron frequency Eq. (2.29)

$$\sigma_{\mathrm{z},0} = \frac{c\sigma_{\delta,0}|\alpha_\mathrm{c}|}{2\pi\beta f_\mathrm{rev}\sqrt{\frac{h\eta}{2\pi\beta^2 E} e \left.\frac{dV}{d\psi}\right|_{\psi_\mathrm{s}}}} = \frac{c\sigma_{\delta,0}\sqrt{E|\alpha_\mathrm{c}|}}{f_\mathrm{rev}\sqrt{2\pi h e \left.\frac{dV}{d\psi}\right|_{\psi_\mathrm{s}}}}. \tag{2.31}$$

It is directly dependent on the momentum compaction factor, the energy and the acceleration voltage.

[3] This is not valid for new and complex machines using e.g. combined function magnets.

2.7 Wakefields and Impedances

A moving charged particle will interact with its surroundings and create electric fields that can either act on itself or on surrounding particles. The shape of the electric field created by a single particle is called wake function $W(\mathrm{t})$. These fields obtained their name from their vague similarity to the wake of a ship in water. Their shape depends on the type of interaction between the particle and its surrounding. As in general multiple particles are stored a certain potential develops. This potential is the result of the sum of all the individual electric fields. In general, this potential, called wakepotential, can be described as the convolution of the charge distribution ρ with the wake function W of each particle

$$V_{\mathrm{Wake}}(t) = \int_{-\infty}^{\infty} W(\tau)\rho(t-\tau)d\tau. \tag{2.32}$$

They describe the energy gain of a particle depending on its position and are in general not linear in contrast to the RF potential. While the RF potential leads to an approximately harmonic motion in phase space the wakepotential leads to a disturbance of this harmonic motion. This can lead to sub-bunching of electrons which in turn results in a deformation of the wakepotential.

The wakepotential can also be calculated in frequency domain by multiplication of the Fourier transformed charge distribution $\tilde{\rho}(f)$ with the so-called coupling impedance Z

$$V_{\mathrm{Wake}}(t) = \int_{-\infty}^{\infty} \tilde{\rho}(f)Z(f)e^{i2\pi ft}df. \tag{2.33}$$

The impedance Z is used in analogy to impedances in electronics and is given as the Fourier transform of the wake function

$$Z(f) = \mathcal{F}(W(t)). \tag{2.34}$$

Especially for numerical calculations the determination of the wakepotential in frequency domain is useful as it substitutes the expensive calculation of the convolution in Eq. (2.32) with a set of less expensive Fourier transforms and a multiplication.

There are multiple sources of impedances. A change in diameter of the beam pipe, for example, leads to electric fields left behind a bunch and therefore contributes to the impedance of the ring. Impedances from geometric sources are called geometric impedances. Additionally, through the finite resistance of the beam pipe mirror charges

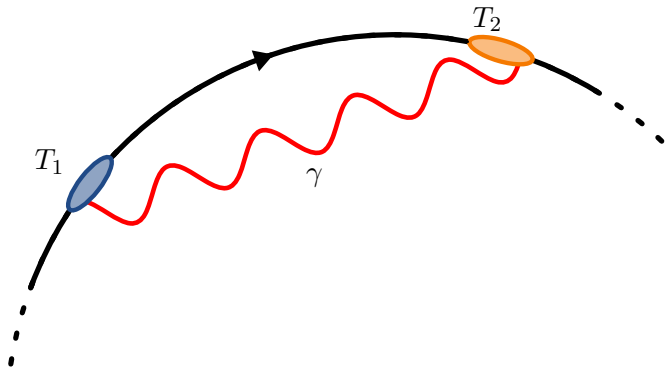

Figure 2.8: Coherent synchrotron radiation (CSR) is not affected by magnetic fields and moves on a straight line. It can therefore "overtake" the bunch. A photon emitted at time T_1 at the back of the bunch can interact with an electron at the front of the bunch at time T_2 and therefore circumvent causality.

are slowed down resulting in wakefields as well. The corresponding impedance is called resistive wall impedance.

In general, due to causality the wakefields are located strictly behind the source particle. There are however exemptions such as the impedance caused by the emission of coherent synchrotron radiation. Due to magnetic fields, the particles in a circular accelerator are forced on circular paths. The radiation, however, is unaffected by magnetic fields and moves on a straight line. Thus, the radiation can "overtake" the bunch, as illustrated in Fig. 2.8 and a potential in front of the original source particle can exist.

This longitudinal effect is typically described by one of two impedances depending on whether the bunch moves through vacuum or far away from surroundings or if the bunch moves in a vacuum pipe. In the first case, the impedance models the interaction of the bunch with its own radiation when moving on a circular path. It is called free space CSR impedance. In the second case, the pipe is modelled as two parallel perfectly conducting plates. That is why this impedance is called parallel plates CSR impedance. These plates result in a shielding effect, where long wavelengths are suppressed and do not propagate. Both cases are displayed in Fig. 2.9, where for the calculation of the parallel plates CSR impedance a gap height of $g = 32\,\mathrm{mm}$ was used. In the parallel plates case the suppression of low frequencies through the shielding effect can be seen. A further aspect visible is the convergence of the parallel plates CSR impedance to the free space CSR impedance for high frequencies. While the parallel plates model is an approximation to the real shape of the beam pipe, several studies showed its applicability (e.g. [11, 12]). The wakepotential corresponding to a Gaussian shaped bunch under the influence of the parallel plates CSR impedance is shown in Fig. 2.10.

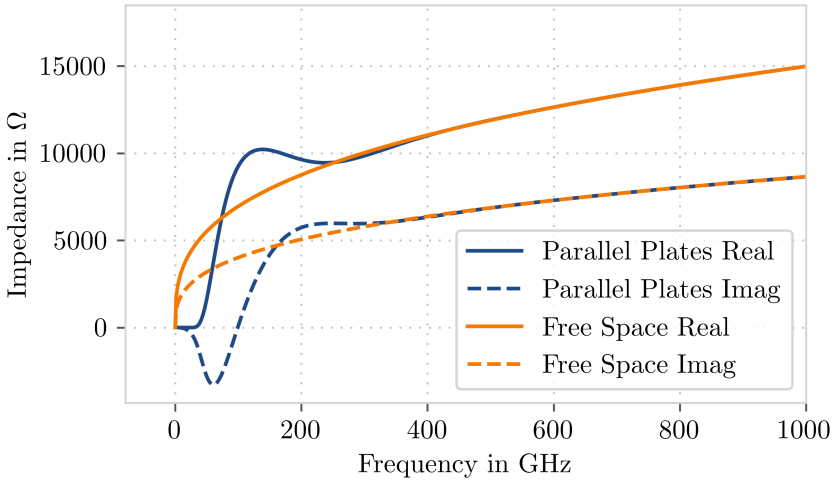

Figure 2.9: CSR impedances for free space and parallel plates. The gap height for the calculation of the parallel plates CSR impedance is $g = 32\,\mathrm{mm}$ and the bending radius for both impedances is $R = 5.559\,\mathrm{m}$

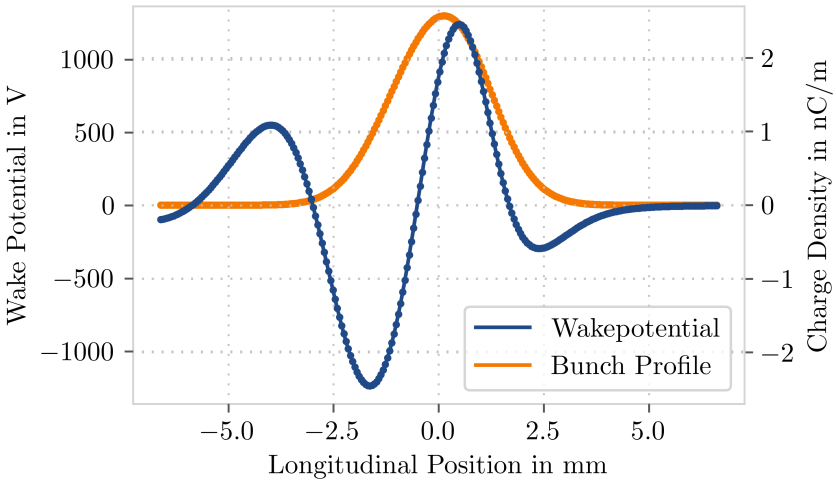

Figure 2.10: Wakepotential (blue) for a Gaussian bunch (orange) with $I_\mathrm{b} = 0.02\,\mathrm{mA}$ and a natural bunch length of 3.67 ps under the influence of the parallel plates CSR impedance displayed in Fig. 2.9.

3 KARA & Negative Momentum Compaction Factor Operation

This chapter first introduces the electron synchrotron KARA, Section 3.1, where the work in this thesis was performed. The already implemented operation modes will be mentioned with a detailed focus on the low alpha mode used for short bunch operation in Section 3.2.

The main focus of this thesis is the study of dynamics at operation with a negative momentum compaction factor. Therefore, such an operation mode first had to be implemented at KARA. This was possible due to the flexibility of KARA as an accelerator test facility in terms of optics, beam position and time slots available for such experiments. The changes to the optics performed to achieve negative α_c operation in the framework of this thesis as well the method used will be described in Section 3.3. The implementation status has been published in [Sch19b, Sch20, Sch21]. The last section discusses the beam energies available for the different operation modes.

3.1 Karlsruhe Research Accelerator - KARA

The Karlsruhe Research Accelerator (KARA) is the storage ring of the KIT light source and located at Campus North of the Karlsruhe Institute of Technology (KIT) in Karlsruhe [13] [1]. It is an electron synchrotron with a variable beam energy from 0.5-2.5 GeV. A pre-accelerator chain consisting of three systems is used before the electrons are injected into the main accelerator ring. The electrons are produced with a thermionic gun and are subsequently accelerated from 90 keV to an energy of about 53 MeV using a racetrack microtron. The last stage is a booster synchrotron that accelerates the electrons to 0.5 GeV followed by the actual injection into KARA where the electrons are accumulated until the desired beam and bunch currents are reached. This injection process is pulsed with 1 Hz repetition rate. Now the electron energy can be increased up to a maximum energy of 2.5 GeV depending on the experiments. Currently, defined operation modes at 0.5 GeV, 0.9 GeV, 1.3 GeV, 1.6 GeV and 2.5 GeV are available. The filling pattern

[1] Please note, KARA is the storage ring of the KIT light source, formerly known as ANKA

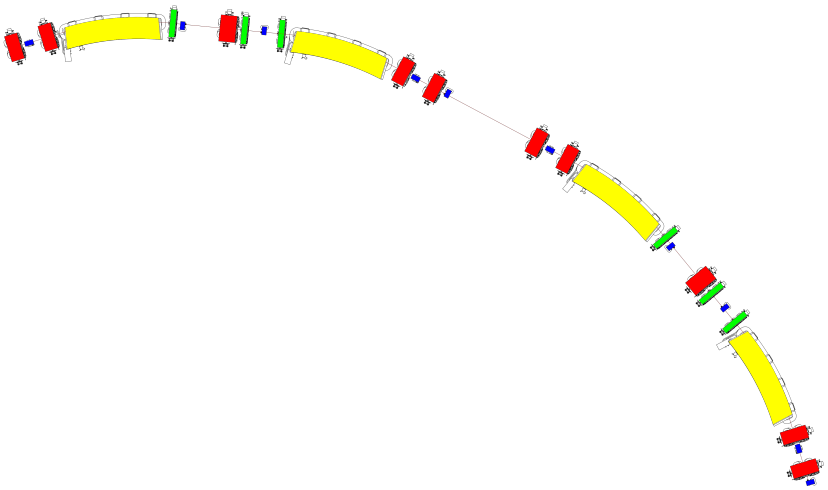

Figure 3.1: Part of the magnetic lattice of KARA. This corresponds to one quarterof the four-fold symmetric storage ring. Yellow elements represent bending dipole magnets, red elements are quadrupole magnets and green elements represent sextupole magnets. The thin visible line shows the beam pipe. Image modified, original courtesy of KIT/IBPT.

(distribution of electrons over different bunches) can be chosen quite flexibly. The booster synchrotron injects roughly 33 bunches at user definable positions into KARA where individual bunches can be partially or completely kicked out using the Bunch-By-Bunch Feedback system resulting in a user defined filling pattern [14]. Alternatively, a single bunch injection from the gun to KARA is possible, however during the time this thesis was conducted this mode was temporarily not available.

The magnetic lattice consists of bending dipoles and quadrupole and sextupole magnets arranged as double bend achromat structure and is shown in Fig. 3.1. Magnets of the same type and function in KARA are aggregated into families. There are five quadrupole families (Q1-Q5) used for focusing and two sextupole families (SV, SH) used for chromaticity correction. KARA has of a four-fold symmetry with symmetry cells consisting of two double-bend-achromat (DBA)[2] structures and a bending radius in the dipole magnets of $R = 5.559\,\mathrm{m}$. In two straight sections a total of four RF single-cell cavities with a resonance frequency of 499.654 MHz are located. Additional components are amongst others corrector dipoles and insertion devices[3] beam position monitors and special magnets used for injection.

[2] See e.g. [6].

[3] Devices inserted in straight sections. At KARA they are used to produce enhanced synchrotron radiation in specific frequency ranges.

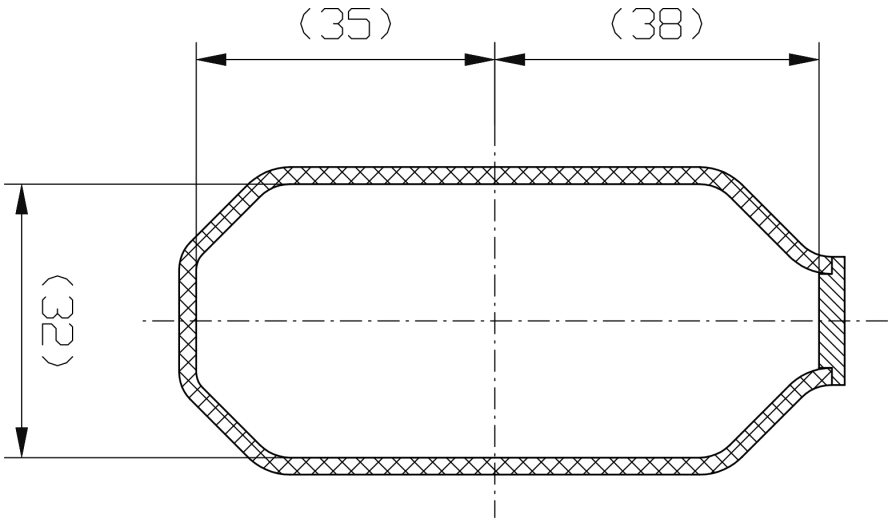

Figure 3.2: Cross-section of the beam pipe used at KARA. Courtesy of IBPT-CAD.

Table 3.1: Basic parameters of KARA.

Property	Value
Circumference	110.4 m
Nominal RF Frequency	499.654 MHz
Harmonic Number	184
Bending Radius	5.559 m
Injection Energy	0.5 GeV
Maximum Energy	2.5 GeV
Accelerating Voltage for 2.5 GeV	1.6 MV

The vacuum pipe is approximately elliptical with a cross-section shown in Fig. 3.2. It has a height of 32 mm and a width of 72 mm in most parts. At locations of additional components the dimensions of the beam pipe can vary. The beam pipe dimensions restrict the maximum transverse position deviations of particles as well as the propagation of radiation for certain wavelengths. The so-called cut-off wavelength defines above which wavelength the propagation is suppressed [15]

$$\lambda_c \approx \sqrt{4g^3/R}, \tag{3.1}$$

where g is the vacuum chamber height and R is the bending radius. The shape of the beam pipe influences the impedance sampled by the beam, e.g. the suppression of emitted wavelengths is considered in the CSR parallel-plates impedance.

The basic parameters of KARA that have been discussed above and are relevant in the context of this thesis are summarised in Tab. 3.1.

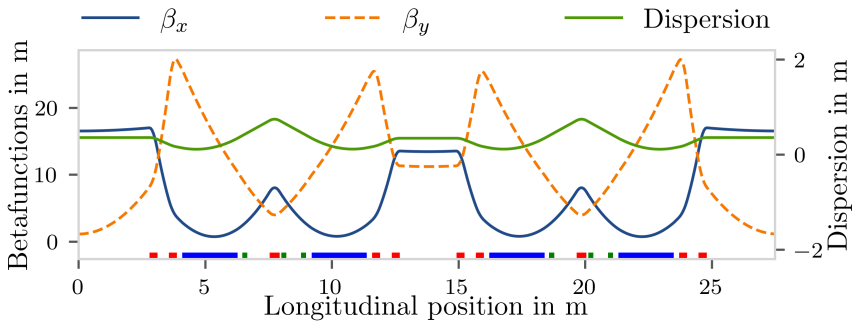

Figure 3.3: Calculated optics used for standard operation at $\alpha_c = 9 \times 10^{-3}$. The bottom depicts the most important magnets, quadrupoles in red, sextupoles in green and bending magnets in blue.

3.2 Standard and Low Momentum Compaction Factor Operation

At KARA multiple operation modes exist [Pap21a, 16, 17]. The most commonly used mode is the so-called "User Mode" or standard operation mode where the experimental stations, stations connected to light transport pipes (beamlines) that are used to extract the synchrotron radiation from the accelerator, have the best conditions for their experiments. This mode uses the maximum energy of 2.5 GeV to provide radiation up to hard X-ray frequencies. For insertion devices with low vertical gap height, an optics with low vertical beta function at the long straight sections of the ring is used [18, 19]. To achieve a high lifetime the momentum compaction factor is set to about 9×10^{-3} as it results in long bunches (about 50 ps). The optics used in this mode is shown in Fig. 3.3. The beam in this mode is stable with a rough maximum current of 200 mA. This stability is achieved with the bunch-by-bunch feedback system to damp instabilities, such as the coupled bunch instability [14].

Besides the standard operation mode there is a dedicated short bunch mode called "Low Alpha Mode" at 1.3 GeV where the focus is not on beam stability or transverse size but more on shorter bunch lengths. Short bunches are useful for experiments requiring short pulses and the creation of coherent synchrotron radiation (Section 2.5). The energy of 1.3 GeV has been chosen due to the shorter bunch lengths compared to the normal energy of 2.5 GeV and a higher lifetime compared to lower energies. The reduction is realised by manipulating the momentum compaction factor in a process referred to as "squeezing". This process uses synchronised changes in quadrupole magnet currents to achieve a lower momentum compaction factor, while keeping the stored electron beam, resulting in shorter bunches. Thereby the centre quadrupole (Q3) in each

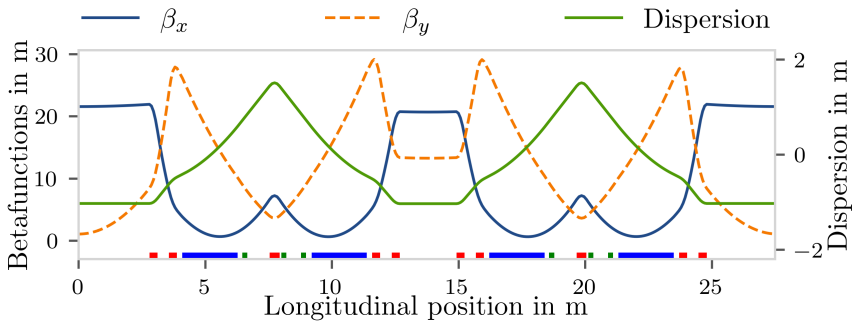

Figure 3.4: Calculated optics used for short bunch operation at α_c=1 × 10^{-4}.

DBA cell influences the momentum compaction factor as well as the tunes which are synchronously kept constant using the other four quadrupole magnets. Figure 3.4 shows an example of the used optics in this mode. One focus of usage in this mode is the study of beam dynamics and instabilities, most prominently the micro-bunching instability [20]. Therefore, the feedback system is not as often used as in the user mode as it can alter the beam dynamics and therefore alter the results of experiments. The minimum value of α_c in this mode is roughly $\alpha_c \approx 2 \times 10^{-4}$ where the most prominent limiting factor is a drastic reduction of lifetime with reduced α_c, as e.g. the losses caused by the Touschek effect increase due to the increased charge density for shorter bunches. This reduction might be even increased by fluctuations (ripples caused by the power supply) in the current powering the magnets and therefore even further unwanted temporal reduction of α_c and lifetime. This could, in extreme cases, even lead to values of $\alpha_c \leq 0$ at which point the phase focusing stops and the beam would be lost.

The momentum compaction factor in this operation mode can be chosen quite freely resulting in a variable bunch length. Furthermore, as the RF system is designed for beam energies up to 2.5 GeV the range of usable RF voltage is large at an energy of 1.3 GeV. It is therefore a second parameter that can be used to modify the bunch length. Taking both measures into account, the natural bunch length can be varied in a wide range from roughly 30 ps down to 2 ps.

3.3 Negative Momentum Compaction Operation & Implementation

The lattice at KARA not only allows the low alpha mode but even allows optics with negative values of α_c provided the absolute value of α_c is large enough, so the lifetime reduction is not too severe.

Operation with negative α_c has been implemented in the course of this thesis for the first time at KARA. The status has been published at multiple stages [Sch19b, Sch20, Sch21]. Various values of negative α_c between -8×10^{-3} and -3.5×10^{-4} are available now at multiple energies. The filling pattern can be chosen freely, which is used for various measurements as explained in Section 5.4.

Reaching negative α_c was done by first lowering α_c at injection energy until no injection was possible any more. While low-α_c optics are available at 1.3 GeV at KARA the necessary optics at injection energy of 0.5 GeV had to be implemented first. Starting from the magnet values in the lower α_c state the values for negative α_c were extrapolated based on OPA [21] simulations.

According to Eq. (2.13), $\alpha_c = \frac{1}{L_0} \oint \frac{D(s)}{R(s)} ds$, the momentum compaction factor α_c can be influenced by modifying the dispersion function. With the magnetic lattice of KARA the most efficient way to change dispersion is to adjust the strength of the field lens quadrupole Q3 in the centre of the DBA structure seen in Fig. 3.1. In order to reduce α_c the dispersion function needs to be stretched into negative values in areas where the bending radius is finite. To do this the strength of Q3 is increased. The strategy used during this thesis to increase Q3 and reduce α_c will be described below. It is important to note, that the adjustment of magnet strengths is performed by modifying the current through the magnets. A conversion to translate magnet currents into magnet strengths based on measurement data exists [22]. However, due to several effects such as ageing and alignment errors the translated magnet strength was used as starting point and small adjustments to the magnet currents were made in order to compensate.

Starting from the usual injection optics at $\alpha_c \approx 8 \times 10^{-3}$ the momentum compaction factor can be reduced with the injection running to reduce the value of α_c while having direct feedback if injection is still possible. In order to still enable a significant injection rate the tunes had to be kept constant and away from resonances, by adjusting the strengths of the other 4 quadrupole families, where the outer two mostly control the horizontal tune and the inner two the vertical tune. Furthermore, the injection septum and kicker magnets need to be adjusted as well to enable injection and avoid beam loss due to wrongly dimensioned kicker strengths which cause the beam to effectively be kicked out. Some fine tuning can be performed by tuning the corrector magnets to increase injection rate. At first a low α_c optics has been calculated using OPA [21] at injection energy. According to the results the quadrupole magnet currents were scaled and step-wise adjusted to slowly approach the simulated end values. During the procedure, the strengths of the injection septum, kicker magnets, corrector magnets as well as the RF-frequency and voltage were manually adjusted in order to keep

the injection rate high and stabilise the beam. Once the significantly lower value of $\alpha_c \approx 7 \times 10^{-4}$ was reached and injection was still possible the performed changes to reach this point were used to extrapolate the changes necessary to reach a new optics with a negative momentum compaction factor. Based on these new calculations the quadrupole magnet currents were scaled for negative momentum compaction injection and the phase of the injection booster was switched by roughly 180 deg to guarantee phase focusing. However, from turn-by-turn BPM data it was determined that after only a few turns the injected beam was lost. Further adjustments to the additional elements were necessary. These were amongst others the RF-phase of the booster synchrotron to best match the phase of the injected bunches with the already stored bunches, kicker magnets and injection septum to optimise the injection bump, RF-frequency for energy matching and RF-voltage and corrector magnets to increase the lifetime of the stored bunches. Furthermore, the sextupole magnet strength was reduced resulting in a negative chromaticity. These optimisations resulted first in a longer storage of the injected beam and finally to accumulated current in the storage ring.

It is important to note that implementing a low-α_c optics at KARA can be achieved by gradually lowering α_c with stored beam while crossing $\alpha_c = 0$ results in immediate beam loss. Therefore, the aforementioned procedure was used to directly inject into an optics with a negative value of α_c.

In order for the bunch-by-bunch feedback system [23] to pick up the tunes correctly the acquisition times needed to be switched by about 1 ns, which is half the bunch spacing and corresponds roughly to the change in acceleration phase.

The tunes measured for this initial optics turned out to not be what they were expected. Therefore, as the injection efficiency was quite low, the tunes were moved to the same transverse working point as the usual injection in order to benefit from the already established settings of the bunch-by-bunch feedback system [23] as setting up the feedback system for a new working point can be cumbersome. While the change of the working point was beneficial for beam lifetime and injection rate without the feedback system turned on, the feedback itself did not significantly increase the injection rate or beam lifetime.

Figure 3.5 shows an example orbit used for injection into negative α_c optics. The deviations from the reference orbit reach up to 8 mm, which is large compared to the orbit for standard injection which is below 2 mm. Various different injection orbits are possible. However, all of them show large deviations. Multiple optimisations reducing these deviations such as correction with corrector magnets or kicker magnets were performed. As the deviations seem to follow a dispersive orbit the reason behind the

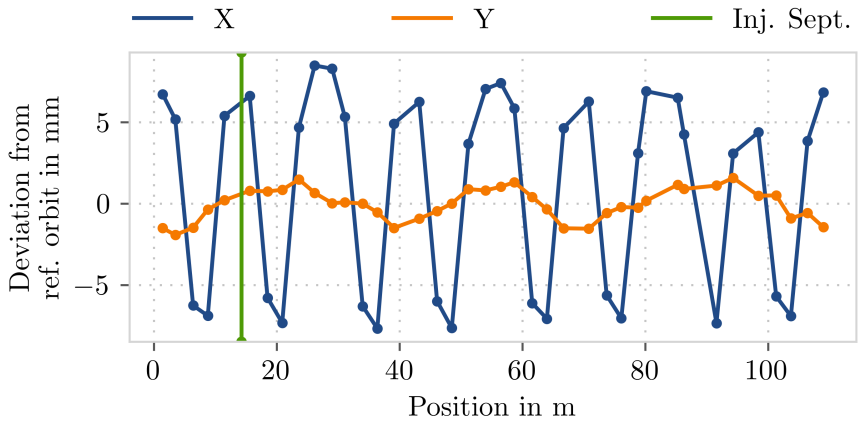

Figure 3.5: Orbit deviations at injection into negative momentum compaction. The green vertical line indicates the position of the injection septum.

orbit deviations could be an energy mismatch between injection booster and storage ring. Therefore, the strength of the main bending magnets in the storage ring were adjusted to compensate such a potential energy mismatch. While these optimisations were successful in reducing the orbit deviations they lead to a reduced injection rate or even to total loss of any injection rate. Therefore, large orbit deviations seem beneficial for injection at negative α_c, at least for the optics used at KARA. Large offsets in the magnets could lead to increased higher order magnetic fields (such as octupole components, otherwise missing at KARA) resulting in adjustments to the optics that might be necessary for efficient injection. For the injections in the framework of this thesis such large deviations were used.

After injection the orbit can be corrected to a certain degree via corrector magnets and the RF frequency without significant beam loss. As the amount of correction possible at injection energy was not sufficient the beam was ramped to higher energies where it is more stable. This allowed for a good correction at 1.3 GeV with deviations below 0.5 mm. More considerations for the beam energy will be discussed in the next section.

To compare the resulting optics with simulations the magnet currents used in operation can be converted into magnetic field strengths [22] and the resulting optics can be calculated using various software codes. For establishing the negative α_c mode OPA was used and the resulting calculated optics are shown in Fig. 3.6. In comparison, the optics calculated from simulations using ocelot [24] are shown in Fig. 3.7. While the shape of the optics functions is the same there are some small discrepancies about the values, tunes and α_c are summarised in Tab. 3.2. Both calculations use the same converted magnet currents and result in roughly the same value of $\alpha_c = -2.12 \times 10^{-3}$ for OPA and $\alpha_c = -2.31 \times 10^{-3}$ for ocelot. Both simulations result in tunes that differ from

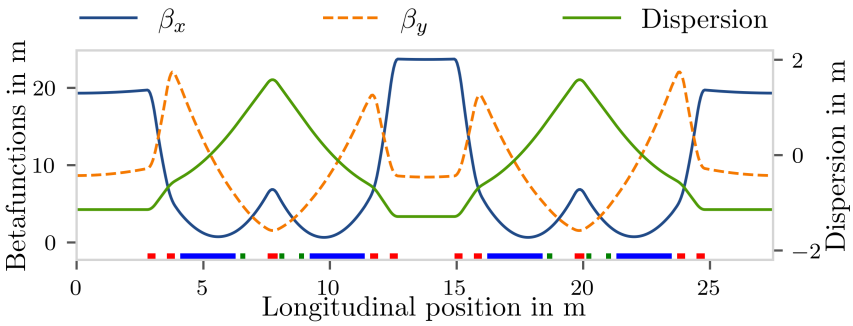

Figure 3.6: Optics calculated with OPA [21] for magnetic field strengths used at KARA for one symmetry cell. The resulting momentum compaction factor is $\alpha_c \approx -2 \times 10^{-3}$.

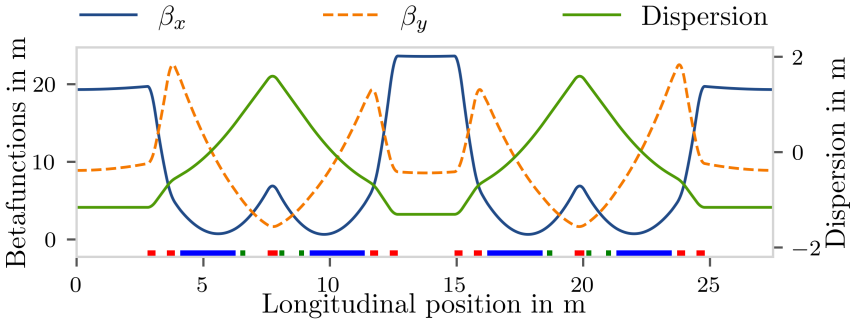

Figure 3.7: Optics functions calculated with Ocelot for negative α_c

Table 3.2: Tunes and α_c for the used simulation tools and measurements for the implemented negative α_c optics, the simulations are based on.

	Q_x	Q_y	$\alpha_c/10^{-3}$
OPA	6.84	2.75	−2.12
Ocelot	6.85	2.64	−2.31
MAD-X	6.85	2.64	−2.29
Measurement	6.75	2.82	−1.28

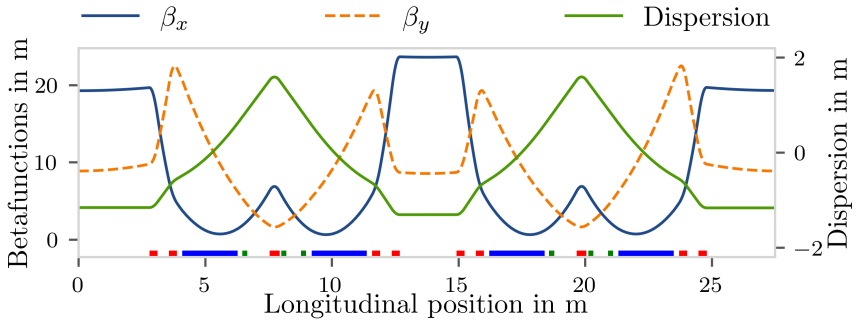

Figure 3.8: Optics functions calculated with MADX for negative α_c for one symmetry cell.

each other and what is seen at the real machine with the OPA being slightly closer to the measured values (see Tab. 3.2). In addition to these codes optics calculations using MAD-X [25] were performed as well. The results are shown in Fig. 3.8. The shapes of the optical functions are again in agreement, while the exact values slightly differ. Furthermore, the momentum compaction factor α_c is calculated to be compatible to the results of the other two simulation tools at $\alpha_c = -2.29 \times 10^{-3}$. The lattices used for the simulations are not necessarily identical, as pre-existing lattices were used[4]. This could be one reason for the observed slight differences between the simulation tools. The difference to the measured parameters could be caused by the large orbit deviations present for the measurements that were not modelled in the simulations. Another reason could be the approximated conversion of the magnet currents to magnet strengths. The differences were deemed to be sufficiently small for the purpose of this thesis.

The results for α_c, the most important parameter for this thesis, differ slightly between the three simulation tools with a maximum deviation of 9 % (Tab. 3.2). While the simulated values for α_c show a discrepancy to the measured value at $\alpha_c \approx (-1.28 \pm 0.02) \times 10^{-3}$ with about a factor of two, the simulation tools confirm the order of magnitude and the negative sign of the momentum compaction factor for the implemented optics. The measured value of α_c is determined by acquiring the synchrotron frequency with the BBB system, with an estimated absolute uncertainty of 100 Hz [26], and calculating α_c via Eq. (2.29).

The successful implementation of the negative α_c optics in the framework of this thesis enabled measurements of different beam parameters, such as chromaticity (Section 4.1), α_c (Section 4.2) and lifetime (Section 4.4). Further beam dynamics studies using this

[4] As the simulation tools are not compatible regarding their input files, different pre-existing files were used. The lattice files for the used tools were built with different objectives and could therefore slightly differ.

newly implemented operation mode were performed and will be presented in detail in this thesis.

3.4 Beam Energy & Ramping at Negative Momentum Compaction Factor

For positive α_c operation modes at various energies at KARA exist. For standard operation an injection optics at 0.5 GeV with $\alpha_c \approx 9 \times 10^{-3}$ is used. To provide hard X-Ray radiation to the users the beam is subsequently ramped to 2.5 GeV with the same α_c. Additionally, multiple specialised short bunch optics exist with a reduced value of α_c. The most experiments in short bunch mode are performed at an energy of 1.3 GeV [17, 20, 27, 28]. Here the bunch length is decreased as described in Section 3.2. Further stable working points at energies of 0.9 GeV and 1.6 GeV are used as well.

During the implementation of negative momentum compaction optics at KARA optics at multiple energies were established. First at 0.5 GeV an injection optics was established and optimised, as described in the previous section. The lifetime at injection energy was only about 10 min compared to typical 30 min at user injection settings for about 0.3 mA bunch current in both cases. To increase the lifetime and allow for comparison between new measurements at negative α_c and existing ones at positive α_c at 1.3 GeV, a ramping routine was developed for the negative α_c optics up to 1.3 GeV. A main contribution to the particle losses and therefore reduction of lifetime is the Touscheck scattering of particles. This results in transversal momentum contributions that lead to large angles between the movement direction of particles and the movement direction of the synchronous particle and therefore leads to particle losses. At higher energies the particles are boosted more strongly and the angle between scattered particles and the synchronous particle is reduced and less particles are lost which increases the lifetime. Furthermore, since the emitted radiation of electrons with higher energy is increased compared to lower energies the damping time is shorter and transverse momenta are damped away more efficiently. This reduces particle losses further and increases lifetime. This effect is comparable at negative and positive α_c showing that handling of negative α_c beams is similar to positive α_c beams in some aspects.

During the energy ramp at a negative momentum compaction factor the already large orbit deviations at injection energy increase. As mentioned before, it was not possible to apply an automated orbit correction at negative α_c and 0.5 GeV. It was therefore not possible to apply such a correction during the energy ramp. Due to this

the corrector magnets are static during the ramp. This means they are not adjusted according to the beam energy. Likewise, an automated compensation for imperfections in the ramping table[5] is not performed during the ramp and potential mismatches in the magnet strengths could lead to energy offsets and therefore an increased dispersion orbit. Optimising the ramping table could alleviate part of these problems. Therefore, during the ramp a stop at 0.9 GeV is introduced at which the orbit deviations are reduced via a multistep procedure consisting of alternating orbit corrections and tune compensations. This resulted in a quite stable operation point at an energy of 0.9 GeV which was subsequently also used for experiments at various values of α_c. Finally, after orbit correction and further energy ramp an optics at 1.3 GeV was established and optimised. At this energy orbit correction was possible and it was possible to reduce the orbit deviations to good values below 0.5 mm. Similar to positive α_c at 1.3 GeV the momentum compaction factor can be reduced at negative α_c via "squeezing" as described in Section 3.2.

At all three energies (0.5, 0.9 and 1.3 GeV) experiments and investigations were conducted. The energy influence on the dynamics will be described in Section 8.6.

[5] Ramping tables are tables of magnet currents defining the strength of the magnets during the ramp.

4 Electron Beam Properties at Negative α_c

After successful implementation of negative α_c operation, described in the previous chapter, this chapter presents measurements of relevant beam parameters during negative α_c operation.

As mentioned in the previous chapter a negative chromaticity is necessary for injection into negative α_c optics. The chromaticity used for operation with negative α_c presented in this thesis is discussed in Section 4.1. This is followed by observations of higher order terms in α_c influenced by changes to sextupole magnet strength in Section 4.2.

The achievable beam and bunch currents at negative α_c were observed to be limited. This is discussed in Section 4.3 followed by a description of lifetime measurements and effects in Section 4.4.

4.1 Chromaticity

The chromaticity in a storage ring is the tune change for a momentum offset as described in Section 2.2 and Eq. (2.10). In a bunch each particle has a slightly different momentum due to the inherent energy spread. Together with the chromaticity this results in a tune spread. As described in Section 2.2 certain tunes lead to unstable conditions due to resonances. The working point has to be chosen in a way that most particles stay clear of these resonances. To estimate the size of the tune spread the chromaticity has to be known. Furthermore, some instabilities depend on the chromaticity such as the Head-Tail instability, see Chapter 6. Therefore, it is important to measure and control the chromaticity. It can be measured by varying the momentum of the beam while recording the coherent tune (average tune of all particles). According to the momentum compaction factor Eq. (2.12) the relative momentum offset is given as

$$\frac{\Delta p}{p_0} = \frac{1}{\alpha_c} \cdot \frac{\Delta L}{L_0}. \tag{4.1}$$

The path length L can be expressed in terms of revolution time t_{rev} and it follows

$$\frac{\Delta p}{p_0} = \frac{1}{\alpha_c} \cdot \frac{\Delta t_{rev}}{t_{rev,0}} = -\frac{1}{\alpha_c} \cdot \frac{f_{rev} - f_{rev,0}}{f_{rev}}. \tag{4.2}$$

With the frequency of the RF system as $f_{RF} = h \cdot f_{rev}$ it is apparent that the momentum can be varied by modifying the frequency of the RF system. Therefore, the chromaticity can be determined from measurements of the tune for different values of the frequency of the RF system. The chromaticity is the slope of the resulting curve of tune as a function of $\frac{\Delta p}{p_0}$ as seen from Eq. (2.10).

At negative α_c multiple adjustments and measurements of the chromaticity were performed. As expected, it was found (see Chapter 3) that a negative chromaticity was necessary for successful injection. A slightly positive chromaticity around 0.2 or higher resulted in zero injection rate. However, with stored beam it was possible to increase the chromaticity to these slightly positive values while keeping the beam stable. After ramping the beam energy with negative α_c optics to 1.3 GeV the chromaticity was varied as well. However, the exact value was not a significant factor for the lifetime, and an optics with chromaticies of $\xi_x = -3.1$ and $\xi_y = -3.7$ was used for the experiments in this thesis.

The effect of different chromaticities was not found to be significant as long as they are negative at negative α_c. For positive chromaticities at negative α_c no injection was possible and further effects are likely to be present, as described in Chapter 6. Therefore, it seems that any negative value can be chosen to fit individual needs without regards to the lifetime.

4.2 Higher Orders of α_c

For the implementation low values of the sextupole magnet strength were helpful as described in the previous section, since they reduce the chromaticity to negative values. However, the sextupoles can also affect the higher orders of the momentum compaction factor. While at positive α_c the higher orders are quite small [29], the changed sextupole magnet strength leads to different and most likely non-negligible higher orders at negative α_c.

The dispersion introduced before, see Eq. (2.11), is a simplification neglecting higher orders due to chromatic effects. The complete dispersion is given as

$$D(s, \delta) = D_0(s) + D_1(s)\delta + D_2(s)\delta^2 + ... \tag{4.3}$$

where $D_1(s), D_1(s), ...$ are the higher order terms of the dispersion. This subsequently leads to terms in the momentum compaction factor including higher orders (α_0 (first), α_1 (second), α_2 (third), ...) when using Eq. (4.3) in Eq. (2.13). These higher order terms of the momentum compaction factor can have an influence on the beam dynamics.

It is therefore interesting to determine these values for the different operation modes at KARA.

A setup to directly measure the higher orders of the momentum compaction factor was available at KARA in the past [29]. However, this setup is not available anymore and other methods for the determination of higher orders of α_c need to be employed. Similar to the determination of the chromaticity the higher orders of the momentum compaction factor can be determined as an approximation from the synchrotron frequency change when varying the beam momentum by changing the frequency of the RF system. When considering the higher orders of the momentum compaction factor up to the second order (α_1), the synchrotron frequency is given by [Pap21b]

$$f_s = f_{rev}\sqrt{\frac{heV\cos\psi_s}{2\pi\beta_0^2 E}}\cdot\sqrt{\frac{\alpha_0}{2}+\sqrt{\frac{\alpha_0^2}{4}-\alpha_1\frac{\Delta f_{RF}}{f_{RF}}}} \tag{4.4}$$

with $\beta_0 = \frac{v}{c}$. By fitting Eq. (4.4) to the measurement data the first and second orders of the momentum compaction factor can be extracted. Multiple such measurements were performed at positive and negative α_c for different values of the vertical sextupole magnet strength, achieved through different currents through the magnets, in order to evaluate the effect of these magnets on α_c. The measurement of the synchrotron frequency as function of change in frequency of the RF system at 1.3 GeV for positive and negative α_c is shown in Fig. 4.1. The absolute value of α_c chosen for the negative α_c measurement is quite large compared to the value chosen for the positive α_c measurement. A smaller absolute value at negative α_c would not allow these time-intensive measurements, due to the relatively low lifetime at these conditions. Furthermore, a reduction of the frequency of the RF system for the measurements lead to beam loss at low absolute values of α_c.

The plots in Fig. 4.1 show a slope of the f_s values hinting at a non-zero second order $\alpha_1 \neq 0$. In Fig. 4.2 the resulting values for α_0 and α_1 from fits of Eq. (4.4) to the measurement data are shown. The value of α_0 for positive and negative α_c is linearly dependent on the sextupole strength. For positive α_c for the shown change in sextupole magnet current of about 10% the value of α_0 changes by about 4% and for negative α_c for the shown change in sextupole magnet current of about 8%, α_0 changes by about 1.25%. The first order α_0 therefore seems to be less dependent on the sextupoles at negative α_c than at positive α_c. In both cases the absolute value of α_0 reduces for increasing sextupole magnet strength. From Fig. 4.2 is also visible that for positive α_c the value of α_1 varies linearly with the sextupole magnet current. At negative α_c the value of α_1 is not as linear in sextupole magnet current as for positive α_c, however a dependency is visible as well. For positive α_c the second order α_1 is negative while it is

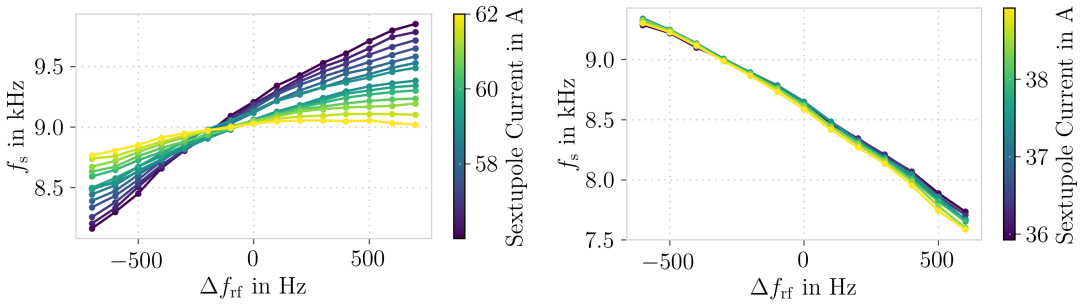

(a) 1.3 GeV at positive $\alpha \approx 5 \times 10^{-4}$.

(b) 1.3 GeV at negative $\alpha \approx -1.1 \times 10^{-3}$.

Figure 4.1: Synchrotron frequency for different vertical sextupole values over the frequency of the RF system for positive (a) and negative (b) α_c at 1.3 GeV. The measurements at negative α_c were done at a significantly larger absolute values of α_0 since the lifetime did not allow for the long measurements at low values of α_0.

positive at negative α_c. Furthermore, while the absolute value of α_0 decreased for both signs of α_c the value of α_1 increases in both cases meaning the absolute value decreases at positive α_c and increases at negative α_c. Note, due to stability restrictions the used sextupole magnet current range at negative α_c is smaller resulting in a smaller absolute α_1 deviation shown in the plot.

Corresponding measurements were also conducted at 0.5 GeV and the resulting measurements at positive and negative α_c are shown in Fig. 4.3. At this energy the measurements at positive and negative α_c were done at comparable absolute values of the first order $|\alpha_0| \approx 1.4 \times 10^{-3}$. The data shown looks quite similar to the data taken for 1.3 GeV shown in Fig. 4.1. Again the slope hints at a non vanishing second order α_1 and the effect of the sextupole on the second order seems larger for positive α_c. Figure 4.4 shows the values for α_0 and α_1 from fits of Eq. (4.4) to the data. For positive α_c the first order of α_c in Fig. 4.4a decreases with increasing sextupole current in the left half of the plot but increases again in the second. The second order α_1 increases over the whole covered sextupole current range seen in Fig. 4.4b. Apart from the first order α_0 at positive α_c the behaviour at 0.5 GeV is quite similar to the behaviour at 1.3 GeV for both positive and negative α_c. The second order α_1 at positive α_c increases with sextupole current as well as the first and second orders at negative α_c. At negative α_c due to stability reasons only a few points could be recorded without loosing the beam.

In principle, it can be concluded that changes in the sextupole strength influence the higher orders of the momentum compaction factor. The direction of changes in both orders of α_c was observed to be the same at both energies 0.5 GeV and 1.3 GeV, which

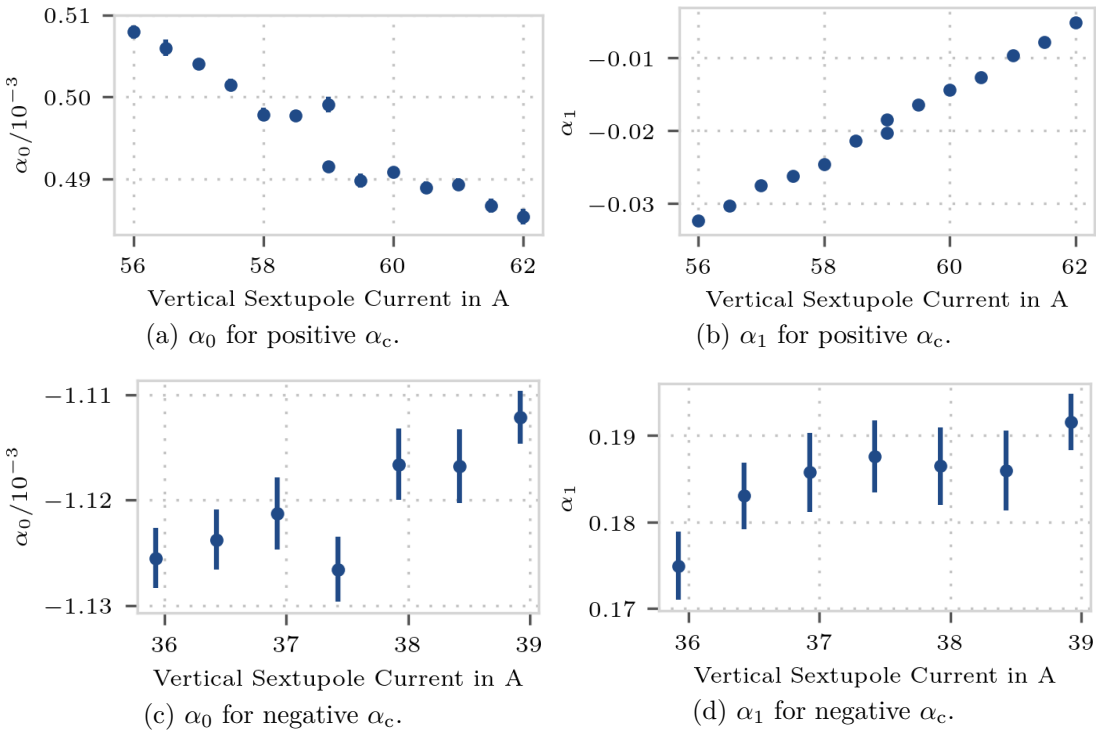

(a) α_0 for positive α_c.

(b) α_1 for positive α_c.

(c) α_0 for negative α_c.

(d) α_1 for negative α_c.

Figure 4.2: First and second order α_c values for positive and negative α_c at an energy of 1.3 GeV from fits on data shown in Fig. 4.1. The shown error-bars represent the errors on the fit including the uncertainty of the synchrotron frequency estimated in [26] as 100 Hz.

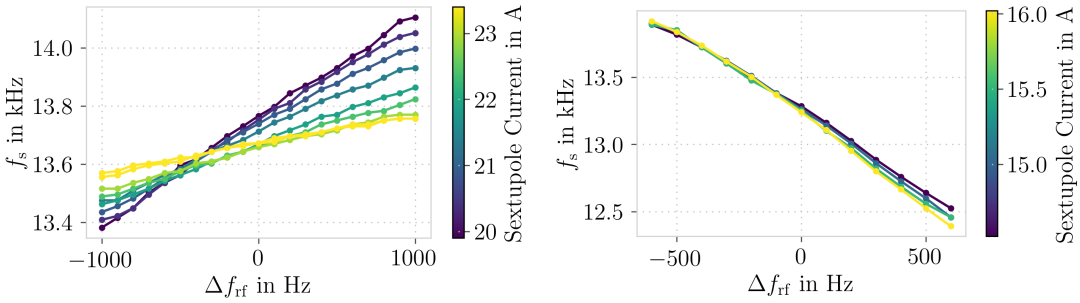

(a) 0.5 GeV at positive $\alpha \approx 1.4 \times 10^{-3}$.

(b) 0.5 GeV at negative $\alpha \approx -1.35 \times 10^{-3}$.

Figure 4.3: Synchrotron frequency for different vertical sextupole values over the frequency of the RF system for positive (a) and negative (b) α_c at 0.5 GeV.

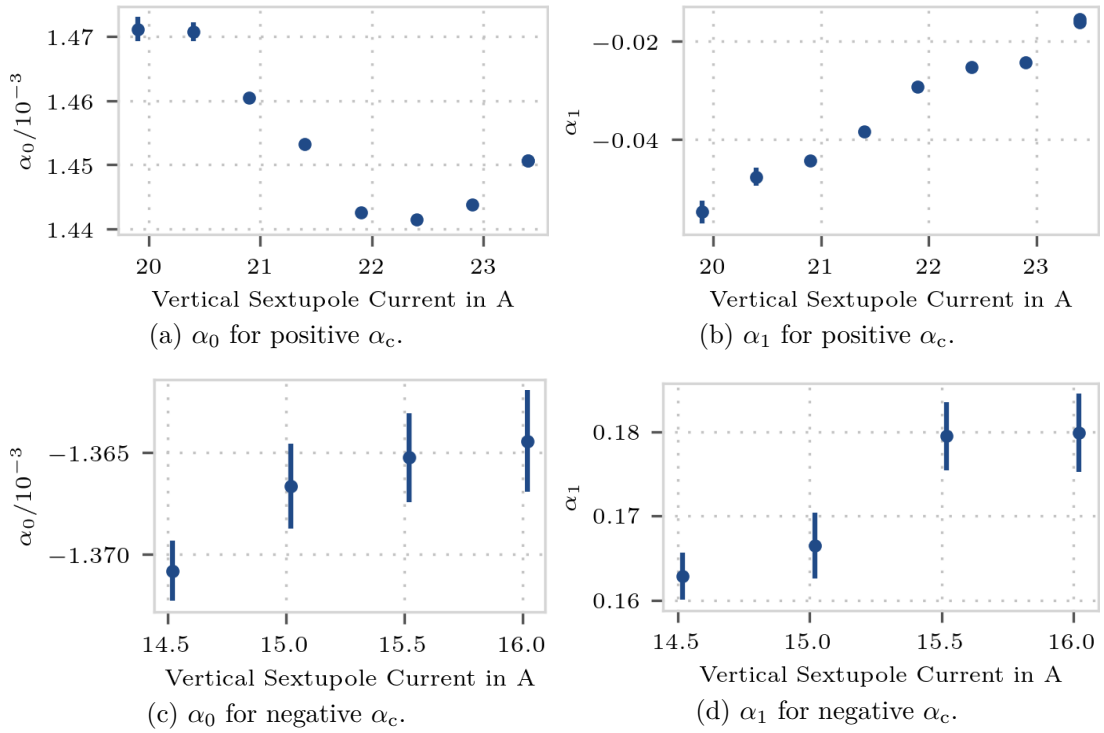

(a) α_0 for positive α_c.

(b) α_1 for positive α_c.

(c) α_0 for negative α_c.

(d) α_1 for negative α_c.

Figure 4.4: First and second order α_c values for positive and negative α_c at an energy of 0.5 GeV from fits on data shown in Fig. 4.3. The shown error-bars represent the errors on the fit including the uncertainty of the synchrotron frequency estimated in [26] as 100 Hz.

is expected as the optics should be independent on energy. These measurements confirm that the efforts to keep the optics fixed before and after the ramp were successful. At positive α_c the first order α_0 decreases in nominal and absolute values while at negative α_c it increases in nominal and decreases in absolute value for an increase in sextupole strength. So in both cases the first order changes in the direction towards zero. This is different for the second order α_1. Here for positive α_c the second order is negative and for negative α_c the second order is positive. In both cases the value increases. This means the absolute value shrinks for positive α_c and increases at negative α_c.

While in the previous section it was concluded that any negative chromaticity can be used, it has to be noted that a change in chromaticity by changes of sextupole strengths will affect the momentum compaction factor including higher orders. The potential of higher order terms in α_c can be seen for example in the study of α-buckets. A discussion for α-buckets at KARA was published in [Pap21b, Pap21c].

4.3 Beam- and Bunch Current Limits

KARA was designed for a maximum beam current of 400 mA [30] with 180 bunches. However, during normal user operation only 160-200 mA is reached with a filling of four bunch trains, consisting of roughly 33 bunches each, resulting in roughly 130 bunches. At negative α_c the maximum accumulable beam current is not easily determined. The beam during injection is sensitive to fluctuations and the same set values in the machine settings, e.g. corrector magnet strengths and quadrupole strengths, do not necessarily result in exactly the same beam conditions for each measurement day. The following tests were performed during a single measurement day to circumvent these problems.

The results are shown in Fig. 4.5. At first the injection into a single train was started and optimised until a limit of 8.7 mA in the accumulated beam current was reached. Then the current decreased to zero and afterwards the injection was adjusted to inject into a second train synchronously. During the injection the conditions were again optimised and a current limit of 10.3 mA was reached with both trains peaking at roughly the same maximum current of 5.5 mA. The total beam current, the sum of both trains, was slightly higher than the total beam current reached with only a single train. During this test both trains were located around the ring 180° opposite to each other. The current decreased to zero again and then the injection was adjusted to inject into four bunch trains distributed evenly along the ring. Then the same procedure was used as before, the conditions were optimised and a maximum beam current of 26.9 mA was reached. The current for each train was slightly higher than the trains for a two train fill but lower

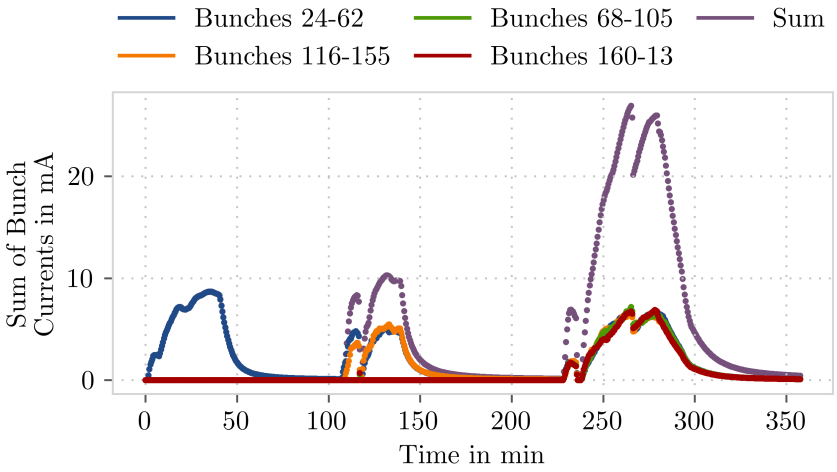

Figure 4.5: Different injection current limits for different number of trains for injection with negative α_c at $\alpha_c \approx -1.5 \times 10^{-3}$. The shown measurement was obtained in a single measurement campaign in order to circumvent the non-perfect reproducibility of machine conditions.

than for the single train fill. The sum current of all four trains however was significantly higher than for any of the other two cases. One reason for this phenomenon could be beneficial long-lasting wakefields that persist for roughly half the revolution time. By filling four trains the gaps between the trains are reduced and the wakefields do not decay as far which could result in a higher current limit for the total beam current. Of course, as the conditions for these tests were manually tuned, it could simply be that there is a single bunch current limit and the differences in train currents for different numbers of trains occurred due to differently optimised conditions.

The maximum beam current reached at negative α_c was approximately 27 mA distributed across 120 bunches. For most measurements a filling pattern with a single train was used. In these cases typical values between 7 mA and 12 mA were possible. About 0.3 mA could be injected during single-bunch operation.

4.4 Lifetime and Limitations

The observed lifetime during negative α_c operation at KARA is systematically lower than the observed lifetime for positive α_c with corresponding machine parameters (mainly $|\alpha_c|$ and acceleration voltage). The lowest lifetime was observed at injection and at very low values of $|\alpha_c|$.

Assuming an exponential current decrease with lifetime τ and an initial current I_0

$$I(t) = I_0 \cdot e^{-t/\tau} \tag{4.5}$$

the lifetime can be calculated from the equality of the derivation and the difference quotient with an infinitesimally small time offset $\varepsilon \to 0$

$$I'(t_0) = \left(\frac{-1}{\tau}\right) \cdot \underbrace{I_0 \cdot e^{-t_0/\tau}}_{I(t_0)} \stackrel{!}{=} \frac{I(t_0-\varepsilon) - I(t_0)}{(t_0-\varepsilon) - t_0}. \tag{4.6}$$

The lifetime is then given as

$$\Rightarrow \tau = \frac{t_0 - (t_0-\varepsilon)}{I(t_0-\varepsilon) - I(t_0)} \cdot I(t_0) \tag{4.7}$$

which is exact for $\varepsilon \to 0$ and an approximation otherwise.

At KARA the lifetime is approximated from the beam current decrease over one minute with $\varepsilon = 60\,\mathrm{s}$

$$\tau(t) = \frac{t - t_1}{I(t_1) - I(t)} \cdot I(t) \tag{4.8}$$

where t is the time of calculation, $t_1 = t - \varepsilon$ and $I(t)$ is the beam current at time t.

Using the above approximation the reconstructed lifetime is underestimated compared to the lifetime of an assumed perfect exponential current decrease by approximately $\varepsilon/2$. For typical values at KARA, $\tau \in [1000\,\mathrm{s}, 100\,000\,\mathrm{s}]$, $I_0 \in [0.1\,\mathrm{mA}, 200\,\mathrm{mA}]$, $t \in [30\,\mathrm{s}, 100\,000\,\mathrm{s}]$ and $\varepsilon = 60\,\mathrm{s}$, numerical tests using randomised values result in an underestimation of $\varepsilon/2 - x$ with $x \in [0\,\mathrm{s}, 0.3\,\mathrm{s}]$ which is 30 s at most. The observed lifetime at KARA increases with decreasing current. This indicates that the current decrease at KARA is not purely exponential. Therefore, the calculated lifetime is to be taken as an estimation rather than an approximation to the exact mathematical lifetime τ.

With regards to the acceleration voltage the lifetime was determined at injection energy and is shown in Fig. 4.6 for positive α_c and Fig. 4.7 for negative α_c. The acceleration voltage was varied with stored beam. The lifetime was estimated using the above method for the entire beam by measuring the beam current with a PCT[1] [31]. This was done in a multi-bunch environment with one train of roughly 33 bunches filled in the storage ring. After each time the acceleration voltage was set a delay of 40 s was used to allow the lifetime to settle. After that the mean of the lifetime was taken over a time of at least 40 s in order to minimise lifetime calculation errors due to jitter on the PCT. Due

[1] Parametric Current Transformer

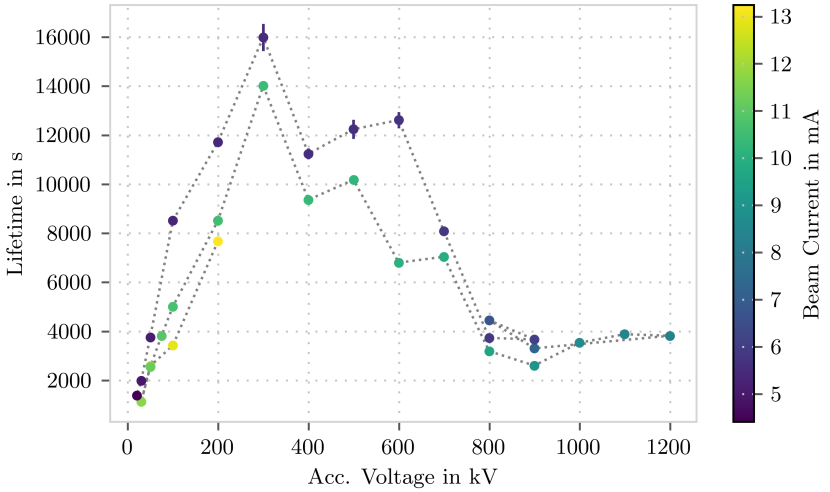

Figure 4.6: Mean lifetime over voltage at positive $\alpha_c \approx 8 \times 10^{-3}$. The measurement was taken during the natural decrease of beam current and the current at the individual measurements is displayed via its colour. The values were calculated as mean over at least 40 s after a delay of 40 s after the acceleration voltage was reached. The error bars indicate the spread of the lifetime during the measurement as standard deviation.

to the low lifetime the beam current decreased noticably over the measurement duration. To minimise the effect of different beam currents on the lifetime, the measurements for each voltage was conducted twice at different beam currents where possible.

For positive α_c the results shown in Fig. 4.6 show a clear maximum at 300 kV with a sharp drop towards lower voltages. Higher voltages show a plateau between 400 and 600 kV and a drop of lifetime until 800 kV. Above 800 kV the lifetime was determined to be constant with acceleration voltage. The drop towards low accelerating voltages can be explained by the shrinking RF acceptance of the ring, which describes the range in RF voltage that support stable operation. Furthermore, the decrease above 300 kV can be explained by the shrinking bunch length that leads to increased Touschek scattering due to a higher particle density and therefore to higher particle losses. The Touschek effect is the transfer of transversal momentum to longitudinal momentum through coulomb scattering of particles in the bunch. The scattering rate for this process is approximately given by [32]

$$\tau_T \approx \frac{48\gamma^2\pi\sigma_x\sigma_y\sigma_z}{Nr_0^2c}\left(\frac{\hat{\Delta p}}{p}\right)^3 \tag{4.9}$$

where $\sigma_{x,y}$ is the bunch dimension in the transversal directions and σ_z is the dimension in the longitudinal direction. r_0 is the classical electron radius and $\hat{\Delta p}$ is the height of the RF bucket with respect to the momentum.

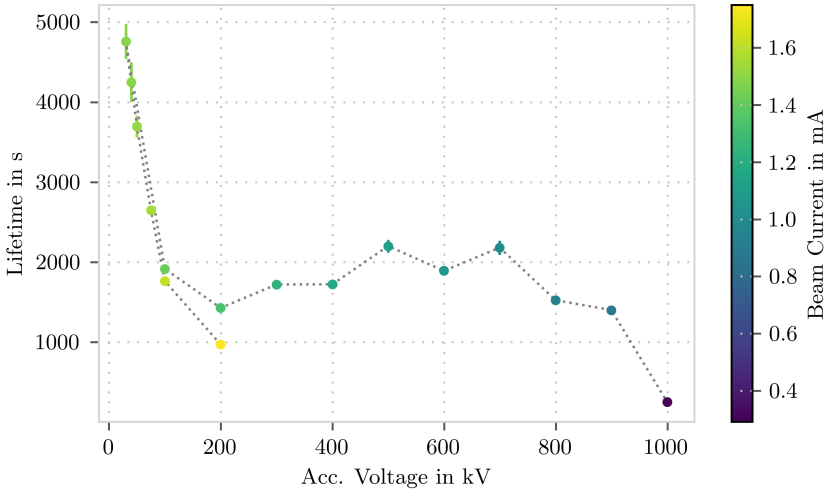

Figure 4.7: Mean lifetime over voltage at negative $\alpha_c \approx -4 \times 10^{-3}$. The measurement was taken during the natural decrease of beam current and the current at the individual measurements is displayed via its colour. The values were calculated as mean over at least 40 s after a delay of 40 s after the acceleration voltage was reached. The error bars indicate the spread of the lifetime during the measurement as standard deviation.

The same measurements were also conducted for negative α_c, and the results are shown in Fig. 4.7. Here low values of the accelerating voltage lead to high lifetime values with the highest values for these measurements at an accelerating voltage of 30 kV. Previous tests have shown that lower accelerating voltages lead to total beam loss. The measurements showing the high lifetime values were done at high bunch currents which makes these values even more significant as the calculated lifetime generally increases with lower bunch currents due to the nature of the calculation and the not purely exponential current decrease.

Tests to inject with very low accelerating voltages in the range of 30-100 kV were however not successful as, despite the good lifetime, only a very low injection rate was achieved. This is suspected to be due to the additional kicker magnets firing during injection which were turned off during the lifetime measurements.

In comparison to positive α_c the lifetime at negative α_c is significantly lower and shows a different trend over the acceleration voltage. Due to the highly stretched dispersion, see Fig. 3.6, in combination with the finite horizontal apertures the momentum acceptance is greatly reduced for the negative α_c case as off-momentum particles move on an extreme dispersive orbit. Through Touschek scattering, which can lead to an additional momentum offset, this can lead to particle loss and therefore to a reduction in lifetime.

Additional negative impacts on the llifetime at negative α_c could be caused by the large horizontal orbit deviations of almost 8 mm from the reference orbit shown in Fig. 3.5. Compared to injection into normal positive α_c optics where the largest horizontal deviation of about 2 mm is around the injection septum, the negative α_c deviations are quite large. Due to multiple finite horizontal apertures, e.g. scrapers in front of insertion devices, the probability of loosing particles increases. These large deviations combined with the stretched dispersion decrease the momentum acceptance even further resulting in a further decrease in lifetime.

As seen from Eq. (4.9) the Touschek scattering rate increases for shorter bunches. In the framework of this thesis, measurements of the bunch length at negative α_c were performed, see Chapter 7. They show shorter bunches compared to the positive α_c bunch length at the same absolute values of α_c and the acceleration voltage. Therefore, the Touschek scattering rate is increased which results in more particle losses and a shorter lifetime. In the framework of this thesis the injection into negative α_c optics was performed at lower absolute values of the momentum compaction factor compared to what is used for injection at positive α_c. It would be possible to increase the absolute value of α_c at negative α_c and therefore reduce the Touschek losses. However, in order to do that the dispersion needs to be stretched even more which results in larger orbit deviations and again increased particle losses. Therefore, for each synchrotron light source interested in using negative α_c the optimum needs to be found individually. From the measurements and observations in this thesis a lower lifetime is expected for negative α_c compared to positive α_c in any case.

5 Tools and Methods

A working negative α_c mode at KARA allows to observe and investigate the beam dynamics of this new operation mode in order to evaluate it for use in future synchrotron light sources. As described in the introduction, Chapter 1, α_c as parameter has great influence on the longitudinal beam dynamics. It affects the movement of particles in the longitudinal phase space, especially due to the required RF phase change by approximately 180 deg for negative α_c. Combined with the negative sign of α_c this leads to a reversed rotation of the charge density in the longitudinal phase space (Section 2.4). However, some effects such as the generation of radiation or wakefields are not directly affected by the sign of α_c. These act back on the longitudinal phase space in the same way as they do at positive α_c, which changes the dynamic behaviour of a bunch even further. For these reasons investigations on the longitudinal dynamics of the negative α_c regime at KARA were performed by observing the current-dependent bunch length and longitudinal instabilities. These observations were conducted at an energy of 1.3 GeV if not stated otherwise. This section introduces the measurement methods used to observe the change in dynamics.

5.1 Horizontal Kick and Damping Time Measurements

In order to assess the transverse stability of the negative α_c mode compared to positive α_c, the horizontal position response of the beam after a transverse kick has been recorded. The results are discussed in Chapter 6. The kick was achieved by deactivating all injection magnets except for one of the horizontal kicker magnets. By activating the injection trigger this magnet was kicking the beam once every second for a few turns. Simultaneously the turn-by-turn acquisition of certain beam position monitors was activated and the data read out. This results in 2^{17} recorded turns, where the initial kick is recorded after the first few turns. These measurements were conducted at injection energy of 0.5 GeV. In the injection optics at positive α_c as well as at negative α_c the position of a stable beam might not be zero. Therefore, to ease the comparison between positive and negative α_c the mean beam position was subtracted from the data. This highlights the actual position oscillations as offsets.

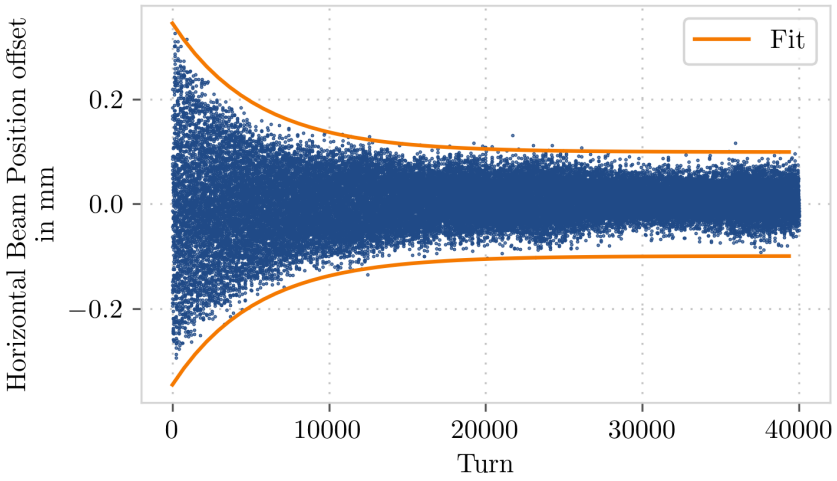

Figure 5.1: Position offset data after a horizontal kick. The solid orange line shows the exponential fit to the envelope used to extract the damping time. The data was taken at $\alpha_c = -1.5 \times 10^{-3}$ with negative chromaticities $\zeta_x = -3.1$ and $\zeta_y = -3.7$.

Furthermore, the effects of damping can be seen in the data as a reduction in beam position offset over time. As the damping effects are expected to be slower at lower energies, the measurements described in this section were performed at injection energy of 0.5 GeV. By fitting an exponential function to the data a characteristic damping time can be extracted. As the horizontal position oscillates with various frequencies, such as the betatron and synchrotron frequencies, the mentioned fit was performed on an envelope of the position offset. The damping process affects the offset independently of the sign, therefore, the envelope was determined on the absolute of the measurement data. A least square fit of the equation

$$f_{\text{fit}}(t) = a \cdot e^{-b \cdot t} + c_{\text{offset}} \tag{5.1}$$

was used, where a and b are the free fit parameters. The parameter c_{offset} is constant per measurement and determined as offset of the envelope at the end of the measurement (after about 2^{17} turns), where the position offset is fairly constant. The damping time τ can then be calculated as inverse of b: $\frac{1}{\tau} = b$. A resulting fit for an example dataset is shown in Fig. 5.1, where the beam position offset as well as $+f_{\text{fit}}(t)$ and $-f_{\text{fit}}(t)$ is shown to highlight the fit as envelope.

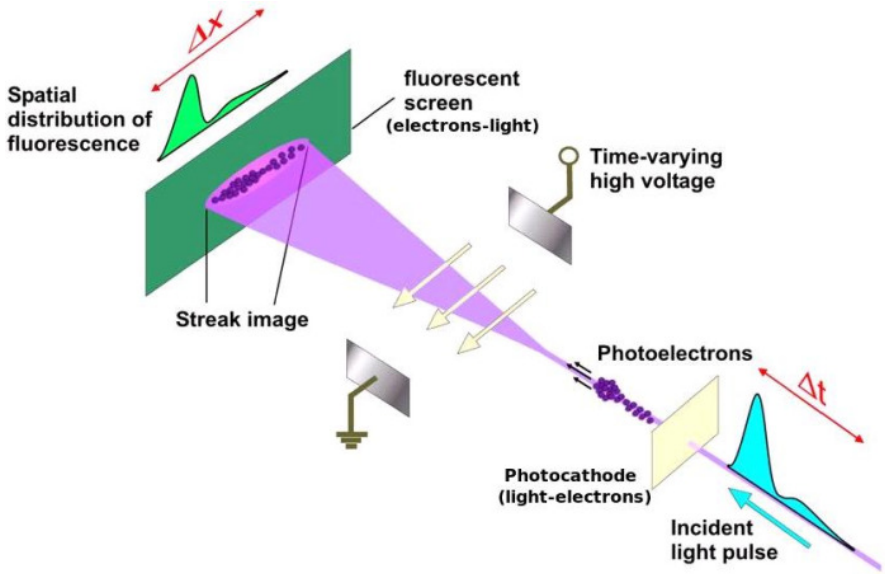

Figure 5.2: Working principle of a streak camera. Photons are converted to electrons that are accelerated. A time varying electric field is applied perpendicular to the movement direction, that transforms longitudinal properties into transversal properties. [33]

5.2 Bunch Length Measurement Method

The bunch length at KARA can be measured with a dual sweeping streak camera[1] using light pulses emitted by the electron bunch. A streak camera is a device used to measure the longitudinal, i.e. temporal, properties of a light pulse. The incoherent synchrotron radiation emitted at a bending magnet has the same longitudinal properties than the bunch that emitted the radiation. Therefore, a streak camera sensitive to visible radiation can be used to characterise the longitudinal particle distribution of a bunch and hence to measure the bunch length. The working principle of such a device is visualised in Fig. 5.2. It uses a photo cathode that creates electrons from incoming photons. These electrons are then accelerated longitudinally to a defined speed. Perpendicular to the movement direction of the electrons a time varying electric field is applied, which transforms the longitudinal distribution into a transversal distribution. This process is called streaking. The electrons then hit a fluorescence screen, which is recorded with a CCD camera. The transverse dimension of the image therefore corresponds to the longitudinal dimensions of the bunch. With the knowledge of the speed of the electrons in the streak camera and the electric field used for streaking, the original bunch length can be calculated.

The CCD camera takes longer to acquire an image than the temporal distance of consecutive bunches. Therefore, during the acquisition of the image multiple bunches

[1] Model: Hamamatsu C5680

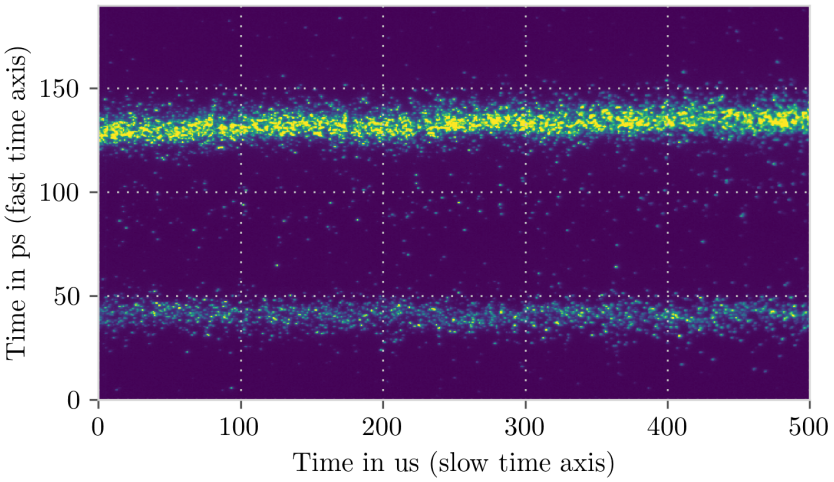

Figure 5.3: Example streak camera image. Visible are two stripes representing the evolution of bunches over time. The vertical axis is the fast time axis encoding the longitudinal properties of a bunch. The horizontal axis is the slow time axis used to observe time evolution of the longitudinal bunch properties. The two stipes are due to the internal working of the streak camera showing every other bunch on top and the other bunches on bottom.

arrive and their picture gets overlaid in the final image taken. To avoid the overlay, some streak cameras have the possibility to streak in two directions with different streaking speeds. The repeated fast streak allows to resolve the longitudinal properties of the bunch and the slower streak allows to seperate multiple bunches. The images of multiple bunches are separated in the direction of the slower streak. If only a single bunch is filled in the accelerator the slow streaking axis can be used to record the temporal evolution of the longitudinal bunch properties over turns. The resulting image with fast time axis in the y-direction and slow time axis in the x-direction is shown in Fig. 5.3. This image was recorded in a fill with multiple even bunches and one odd bunch[2] at negative α_c. Due to the up and downwards sweep in the used streak camera the even and odd bunches are separated in the upper and lower half of the resulting image.

For measurements in this thesis the fast time axis is used to resolve the bunch length. Due to the low absolute values of α_c used, which result in short bunches, the streak time was set to the smallest value of 190 ps. The slow time axis is used to resolve the evolution of the bunch length over time. Its value is set in such a way that multiple synchrotron oscillations can be resolved while an adequate intensity of the streak image is still kept and varies depending on the machine settings used.

[2]When numbering each bucket with a natural number the bunches in buckets with an even number are referred to as even bunches and the bunches in buckets with an odd number as odd bunches.

During the natural decrease of bunch current a measurement sequence consisting of 100 pictures with a duration of around 8 s per sequence was taken every 10 s. For the measurements in the framework of this thesis the following analysis was implemented. After correcting for center-of-mass movements, due to e.g. synchrotron motion, the longitudinal profiles resulting from the images are averaged and a full width half maximum bunch length is calculated. At very low currents the signal-to-noise ratio can be quite low and for the centre-of-mass correction a trade-off has to be found between movement correction that follows fast oscillations and high statistics necessary for accurate centre-of-mass determination.

In [28] the accuracy of the determined bunch length was determined to be better than $\Delta l < 0.3\,\mathrm{ps}$ and a similar accuracy is expected here as well.

5.3 CSR Measurement Method

The coherent synchrotron radiation for the conditions at KARA for short bunches is mostly emitted in the low part of the THz frequency range (0.1 THz to $\geq$ 1 THz). At KARA, it is possible to measure synchrotron radiation at IR beamlines which allow the propagation of radiation in this frequency range. Measurements of the temporal variation in the emitted intensity in the THz frequency range can be used as indicator for the longitudinal beam dynamics, which will be discussed in Section 8.2.

Using fast THz sensitive Schottky barrier diode detectors [34] combined with the fast readout system KAPTURE [35] it is possible to record the THz radiation intensity bunch-resolved and turn-by-turn. KAPTURE, KArlsruhe Pulse Taking and Ultra fast Readout Electronics, is a dedicated data acquisition system that focuses on speed and data efficiency. With KAPTURE it is possible to digitise detector pulses with a repetition rate of up to 500 MHz, which corresponds to the RF frequency and bunch repetition rate at KARA. For this, KAPTURE uses up to 4 channels consisting of a separate track-and-hold and a 12 bit ADC each. A new version of KAPTURE (KAPTURE-2) can operate at 1 GHz and 8 channels [36]. There are two modes in which KAPTURE can be operated. By connecting a single detector to a fast signal splitter it is possible to sample the same detector pulse at four different points in time using an individually configurable track-and-hold delay for each channel. This was also used with KAPTURE-2 and 8 channels for pulse reconstruction, published in [37]. For the second mode from one up to a maximum of four detectors can be connected, and their signal synchronously sampled at a single point in time per detector pulse. In the framework of this thesis most measurements of the CSR intensity focus on the temporal fluctuations over the

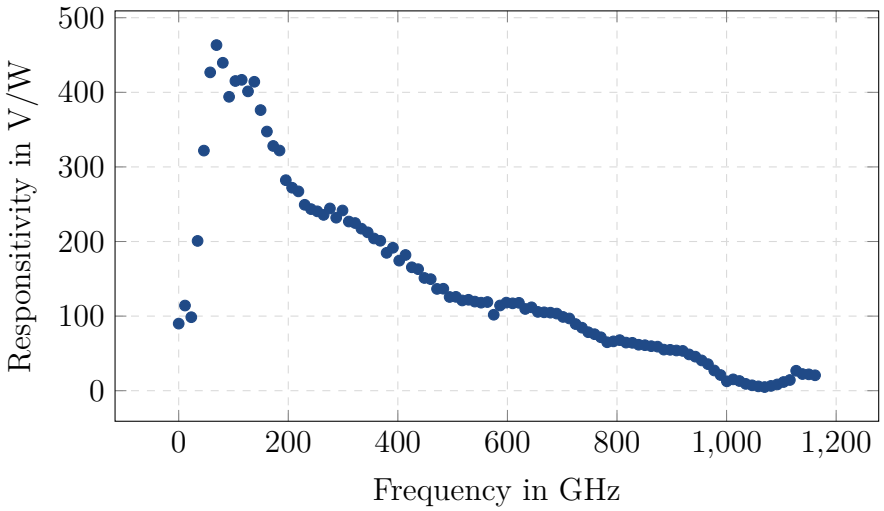

Figure 5.4: Frequency responsivity of the used Schottky barrier diode. Data courtesy of ACST GmbH.

entire emitted frequency range in order to investigate the longitudinal beam dynamics. Therefore, it was chosen to use the system with a single broadband detector connected to a single channel with the sampling time of KAPTURE synchronised to the revolution clock of KARA. As detector a Schottky barrier diode system[3] from ACST [34] was used with a broad sensitivity range from approximately 50 GHz to 1 THz, the frequency responsivity is shown in Fig. 5.4. The sample time was set to the peak of the detector pulse allowing the detection of the signal amplitude. Due to the single sampling point this setup is in theory susceptible to arrival time variations of the THz pulse. However, the detector system uses an internal 4 GHz amplifier that acts as a low-pass filter for the signal and effectively broadens the pulse. The resulting pulse is broad enough so usual arrival time variations[4] do not affect the sampled signal value significantly. Results in Section 8.7 confirm this assumption.

With the described setup KAPTURE is able to record each bunch at each turn for a time duration depending on the memory capabilities. In order to reduce the amount of generated data the THz intensity at every 10th turn was sampled for each bunch. For a good resolution of the temporal properties of the dynamics in the THz radiation, a duration of 1 s was chosen for each acquisition, resulting in a frequency resolution of 1 Hz. As KAPTURE is capable to digitise negative input voltages, the zero voltage ADC count is 2048 by design (half of the 12 bit ADC maximum). Therefore, the ADC count is 2048 when no radiation intensity is detected and this value is subtracted from the

[3] Model: 2DL 12C LS 1200 A2
[4] For negative α_c arrival time variations were observed in the order of low tenths of ps.

measurement values in post-processing in order to evaluate the data with respect to zero radiation intensity.

While this setup is routinely used for studies at positive α_c [38] the setup was used the first time at negative α_c settings in the framework of this thesis. The flexible timing capabilities of KAPTURE provided the possibility to implement the necessary shift of the sampling time, by half an RF period to match the position of the bunch at negative α_c, directly in the KAPTURE system.

5.4 Snapdecay Measurement

The temporal development of the measured THz intensity serves as indication for the dynamics on the longitudinal bunch profile. These dynamics depend on the bunch current. In the context of this thesis a new method to measure this current dependence was developed that reduces the measurement time while keeping a reasonable current resolution. The standard technique and new method will be discussed in the following.

In order to observe the current-dependent temporal dynamics of the bunches, measurements over a wide range of bunch currents are necessary. In the standard technique the current decrease of one bunch is observed over a few hours by acquiring the CSR intensity at regular intervals. The number of acquisitions over the desired beam current range defines the resolution in beam current of the measurement in this approach. Due to the rather long measurement duration the number of measurements conducted at different conditions is limited. Therefore, a different measurement method called snapshot method [27], originally implemented and used at low positive α_c settings, was applied for some measurements. This method can circumvent the time requirements by sacrificing current resolution for speed. It exploits custom filling patterns, where the desired current range is spread over different bunches. One example of such a filling pattern is shown in Fig. 5.5, but in general any filling pattern where the desired bunch current range is covered can be used. A single measurement is taken consisting of data for each bunch. As each bunch has a different bunch current all bunches together form a sort of fingerprint for the current-dependent dynamics, where each bunch represents the dynamics at a different bunch current. The resolution in bunch current for this method is given by the number of bunches with bunch currents in the desired current range. For the applicability of this method it needs to be considered, whether the resulting lowered resolution is able to resolve the current dependency of the observed dynamics. In general, this measurement method is possible as it was shown for positive α_c that the presence of multiple bunches does not strongly influence the individual bunch behaviour [26]. The validity for negative

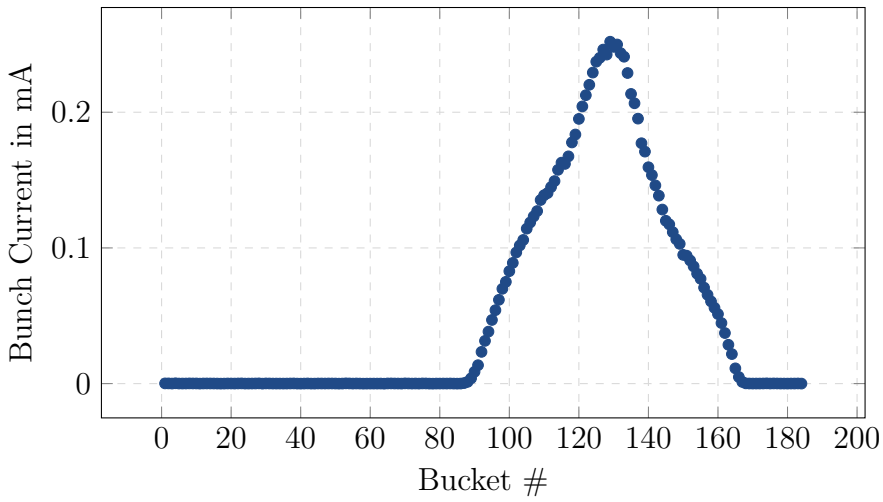

Figure 5.5: Example filling pattern used for snapshot and snapdecay measurements. The bunches in the machine are almost evenly distributed over the desired bunch current range.

α_c was confirmed at random sample points for both voltages shown thought this thesis by comparing results in single and multi-bunch environments.

In the framework of this thesis a new measurement method based on snapshot measurements was developed to regain some current resolution. This method combines the traditional measurement technique of letting the current naturally decrease with the snapshot technique using a special filling pattern by merging multiple snapshot measurements into one. Due to this combination the newly developed measurement method will be referred to as *snapdecays* in this thesis. For this method multiple snapshot measurements are acquired where the bunch current decreases between the individual snapshots. The signals for one bunch now represent the dynamics at multiple bunch currents in this set of snapshot measurements.

By combining all bunches and snapshot measurements similarly to what is done for pure snapshot measurements, a higher resolution in bunch current can be achieved, where the gaps between the bunch currents in the first measurement are filled by the decreased bunch currents in the subsequent measurements. This is illustrated in the sketch shown in Fig. 5.6. The resolution is approximately given by the amount of bunches involved multiplied by the number of snapshot measurements acquired.

Such a measurement takes in the order of a few minutes. As the lifetime in negative α_c mode at KARA is rather low ($\approx 30\,\text{min}$ at negative α_c and 0.1 mA bunch current vs. $\approx 90\,\text{min}$ at positive α_c and also 0.1 mA bunch current) the current range, necessary to fill the gaps in the available bunch currents from the filling pattern, is quickly traversed. Therefore, an increased current resolution is achieved with only a slightly

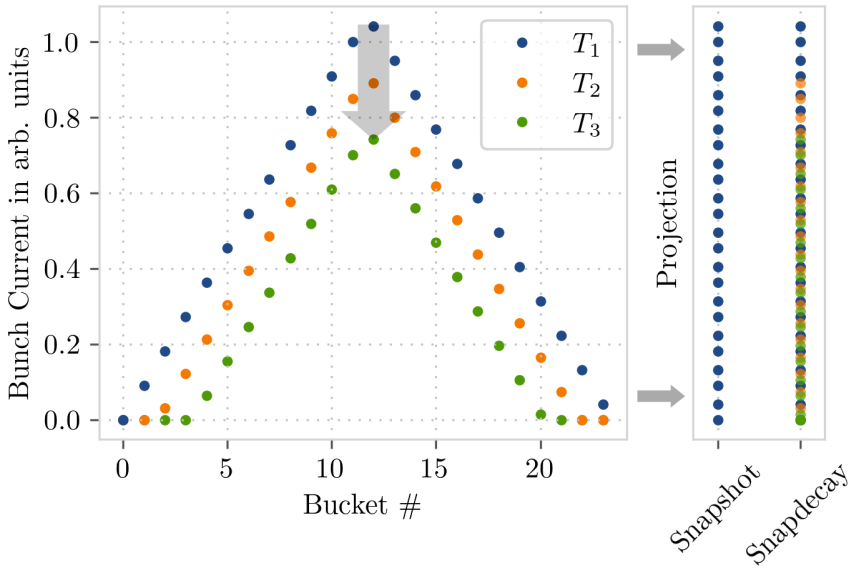

Figure 5.6: Sketch of the improvement in bunch current resolution achieved by snapdecay measurements. In the left panel in blue is the initial filling pattern displayed. Over time the bunch current of each bunch decreases. In this example at three different times (T_1, T_2, T_3) snapshot measurements are taken, the corresponding filling patterns are shown in blue, orange and green. In the right panel projections to the y-axis are displayed. This shows the bunch current resolutions for the two methods, snapshot and snapdecay. For a single snapshot measurement this results from the initial filling pattern. In the case of the snapdecay measurements, resulting from all three filling patterns, the resolution is visible finer.

longer measurement duration in comparison to bare snapshot measurements. This improved method now allows for measurements at multiple conditions within a short time while keeping a high current resolution.

5.5 Bunch Current Measurement Method

As the snapshot and snapdecay measurement methods employ custom multi-bunch filling patterns a detailed knowledge of the individual bunch currents is crucial. In order to assign a current for each bunch at each measurement a time correlated single photon counting setup is used [39]. This method uses incoherent synchrotron radiation in the visible light range emitted by each bunch. The amount of photons emitted is proportional to the number of electrons in a bunch. A Single-Photon Avalanche Diode[5] (SPAD) is used to detect single photons. In front of the diode a small iris lens is mounted to enforce

[5] idQuantique — id100-20 ULN [40]

a small angular acceptance and reduce the miscounting of photons due to background light. The SPAD is connected to a histogramming device[6] with a bin width of 8 ps to cover one revolution period of 368 ns in the available 65 536 bins. The histogramming device is synchronised to the revolution trigger of KARA. By means of its internal clock it sorts the arriving signals from the SPAD into bins starting at bin 0 after the revolution trigger. This results in roughly 46 000 usable bins. These bins are then divided into 184 sections, corresponding to the 184 buckets of KARA. A symmetric area of 50 bins around the maximum bin in each section is summed up. The resulting values are normalised to a sum of 1 and represent the relative filling pattern. To reduce statistical errors the histogramming is run for a certain amount of time. For the measurements in this thesis an acquisition duration of 30 s was used. By multiplication of the filling pattern with the total beam current measured with a PCT[7] [31] the individual bunch currents are acquired. A PCT is a type of current transformer that uses the beam as primary winding and measures the induced current in the secondary winding.

When the time between photons is too short a distortion of the filling pattern is possible. This is due to the dead-time of the diode as well as the PicoHarp device during which new photons cannot be processed. To mitigate this problem a dead-time correction scheme is applied in post-processing. This scheme is described in [39].

Due to construction work at KARA this setup was temporarily located at an IR beamline instead of the visible light diagnostics port [42] resulting in lower count rates and therefore slightly higher statistical errors. The photon counting follows a Poisson distribution, hence with a typical count rate of 3000 counts this results in a relative current error of $\delta = \frac{1}{\sqrt{3000}} = 0.018 = 1.8\%$. For a bunch current of 0.08 mA this would result in an absolute error of $\Delta = \pm 1.46\,\mu\text{A}$. When sorting the signals of multiple bunches for a snapdecay measurement these errors could result in uncertainties on the sorting order of the signals.

5.6 Arrival Time Measurement Method

With the previously described setup of digitising the detector signal at a single point using KAPTURE the detector pulse arrival time cannot be determined. While it is possible to reconstruct the arrival time using all four available channels of KAPTURE together with a signal splitter the reached resolution is limited. Therefore, a different method was used employing an oscilloscope in so-called segmented mode that digitises the detector pulse with its sampling frequency. This mode repeatedly records a waveform

[6] PicoHarp 300 [41]
[7] Parametric Current Transformer

synchronised to an additional trigger input. These measurements were performed using a 4 GHz Agilent[8] oscilloscope. This allows to record the detector response with 20 GS/s. The same detector system as for the THz intensity measurements described in Section 5.3 consisting of the detector element and an internal amplifier is used. As the amplifier has a video bandwidth of 4 GHz the pulse is effectively passed through a low-pass filter that affects the shape of the pulse. This should however not affect the recorded relative arrival time of the detector pulse. Post-processing the data by interpolating the data points via the Whittaker-Shannon interpolation scheme[9] [44] allowed to reconstruct the actual peak value and time of the peak and therefore the arrival time. This is done by determining the amplitude and time of the maximum in the interpolated data. By splitting the detector signal and feeding it simultaneously to KAPTURE and the oscilloscope it is possible to compare the results (cf. Section 8.7).

5.7 Longitudinal Beam Dynamics Simulations

Accompanying the measurements, simulations of the longitudinal beam dynamics were performed using Inovesa[10][Sch19a]. Inovesa is a longitudinal Vlasov-Fokker-Planck (VFP) solver, routinely used at KARA to study the longitudinal beam dynamics [26, 45, 11, Bro19a, 37]. The VFP equation [46] describes the temporal evolution of a charge density under conservative and non-conservative forces such as damping and synchrotron radiation. By choosing the correct Hamiltonian used in the VFP equation collective effects can also be considered. Inovesa iteratively solves the VFP equation for each time step based on the previous step. By doing that, the temporal evolution of the charge density in the longitudinal phase space is acquired. It uses a grid of user definable size chosen for this thesis as a grid of 256×256 cells and a phase space size of $\pm 6\,\sigma_{z,0}$ in the space dimension and $\pm 6\,\sigma_{\delta,0}$ in the energy dimension was used. Inovesa is heavily parallelised via OpenCL [47] that enables intensive simulations on desktop PCs in a reasonable time. During the calculation the wakepotential is frequently required, which Inovesa calculates by multiplying the impedance with the bunch spectrum followed by a reverse fast Fourier transform. This speeds up the calculation since no explicit time intensive convolution of the wakefield with the bunch profile is necessary and also enables Inovesa to operate on predefined and user provided impedances. While Inovesa can work with arbitrary impedances the most dominant, due to the short bunches at KARA, is

[8] Model: MSO9404A
[9] Using the python implementation fsinc by Hope [43]
[10] Inovesa Numerical Optimized Vlasov-Equation Solver Application

the parallel plates CSR impedance. Inovesa simulations using this impedance have been shown to fit well to the measurements at positive α_c [45].

In order to simulate with negative values of the momentum compaction factor some modifications to the Inovesa code were necessary. Due to the change in RF phase necessary for negative momentum compaction as well as the inverted path length change compared to positive momentum compaction the rotation direction in the longitudinal phase space is reversed. Therefore, the most notable change to the source code was the negation of the rotation angle. Other methods to implement negative momentum compaction were also evaluated but were more drastic and resulted in the same results. The code was checked for incompatibilities with the inverse rotation as well as negative momentum compaction factor in general. None such incompatibilities were discovered in the framework of this thesis. Comparisons of simulated THz data to measurements, which will be discussed in later sections of this thesis, showed a similar difference between positive and negative α_c data and the changes to the source code were therefore deemed valid.

Since Inovesa simulates a given time range for a fixed bunch current the current dependency of effects was simulated by performing multiple simulation runs with different bunch currents distributed evenly over the desired current range. As Inovesa works on the longitudinal phase space density any measurable quantities can be derived from these simulations. In general these simulations were done for the same machine settings as used for the measurements.

6 HeadTail Instability

The reason for the need to operate storage rings with positive momentum compaction optics with positive values of the chromaticity, is the so-called head-tail instability. During this instability the head and tail of a bunch perform transversal oscillation with an arbitrary phase between the two.

Particles in a bunch cause wakefields that can act on other particles in the bunch. While later on mostly longitudinal wakefields are considered in this thesis, this chapter will focus on transverse wakefields. The wakefield caused by a leading particle (A) can kick a following particle (B) in transverse direction. Depending on the phase relation between this kick and the betatron oscillation of the following particle (B) this kick can amplify or damp the oscillation amplitude. As the particles additionally perform a synchrotron oscillation the particles will switch positions and the leading particle will become the following particle (AB $\rightarrow$ BA). Depending on the phase relation between the kick (now caused by particle B) and the betatron oscillation of the now following particle (A) again an amplification or damping of the oscillation amplitude of particle A happens. If the phase relation of the initially following particle (B) leads to an amplification and this relation holds after a second switch in position (AB $\rightarrow$ BA $\rightarrow$ AB, the originally following particle is again the following particle), and the amplified oscillation amplitude is not damped through effects such as transversal radiation damping, the oscillation amplitude increases even further. This can lead to particle loss and is called head-tail instability. The mentioned phase relation is mainly determined by the chromaticity and the momentum compaction factor and therefore the growth rate for the instability is strongly dependent on these two quantities. Depending on the phases between the individual particles multiple oscillation modes of the bunch can result, where the zeroth mode, corresponding to a centre of mass oscillation, is the strongest. Theoretical descriptions describe the growth rate β_n of the n^{th} head-tail mode as [48]

$$\beta_n = \frac{1}{\tau} = \frac{NS}{\pi^2 c\gamma m_\text{e}} \frac{\xi}{\alpha_\text{c}} \frac{\sigma_\text{z}}{4n^2 - 1}, \tag{6.1}$$

where τ is the corresponding damping time, N is the number of particles in a bunch, S is the strength of the wakefield and σ_z is the bunch length. The electron mass is denoted

with m_e, the chromaticity with ξ and γ is the relativistic Lorentz factor. Previous experiments show, as expected, a suppression of the instability for $\frac{\xi}{\alpha_c} > 0$ and an amplification for $\frac{\xi}{\alpha_c} < 0$ [48, 49]. The next section will discuss the observations at KARA and show corresponding measurements for both signs of α_c.

To detect intra-bunch motion (head-tail modes $n \neq 0$) for short bunches a high bandwidth of the detectors is required. In theory, it is possible to detect this using beam-position-monitors (BPMs) and for long bunches this has also been done, e.g. in [50]. For short bunches as is the case at KARA, however, this is quite difficult. For a bunch with a bunch length of for example $\sigma_z = 12\,\mathrm{ps}$ the bandwidth of a BPM to differentiate between head and tail needs to be

$$B \geq \frac{1}{12\,\mathrm{ps}} = 83.33\,\mathrm{GHz}. \tag{6.2}$$

At KARA the bandwidth of the BPMs is about 4 GHz. It is therefore not possible to detect intra-bunch head-tail motion using the BPMs at KARA. The following section will therefore discuss observations of the head-tail motion of the zeroth mode $n = 0$, that is the dipole mode visible as centre of mass motion on the BPM signal. Subsequently, the damping rate for stable beams after a kick will be discussed and analysed regarding its current-dependent behaviour caused by the head-tail effect.

6.1 Transverse Coherent Motion

As explained in the previous section the head-tail effect can lead to a damping of transverse oscillation amplitudes. If the relative sign between the chromaticity and the momentum compaction factor is positive $\xi/\alpha_c > 0$, excessive particle positions, e.g. after a kick, are damped with a specific head-tail damping rate $\frac{1}{\tau}$, Eq. (6.1).

An observation of the head-tail effect is therefore possible by measuring the damping effect via the BPM signal after an artificial displacement, as described in Section 5.1. This displacement was caused with an injection kicker, that kicks the beam once every second transversally. Technically this was done by turning off all injection magnets except the one injection kicker and the injection trigger was used to fire it. For 2^{17} turns turn-by-turn beam position data was taken including the initial kick. These measurements were performed at injection energy of 0.5 GeV as the head-tail damping rate is expected to be higher, as seen in Eq. (6.1), and therefore easier to observe, at lower energies.

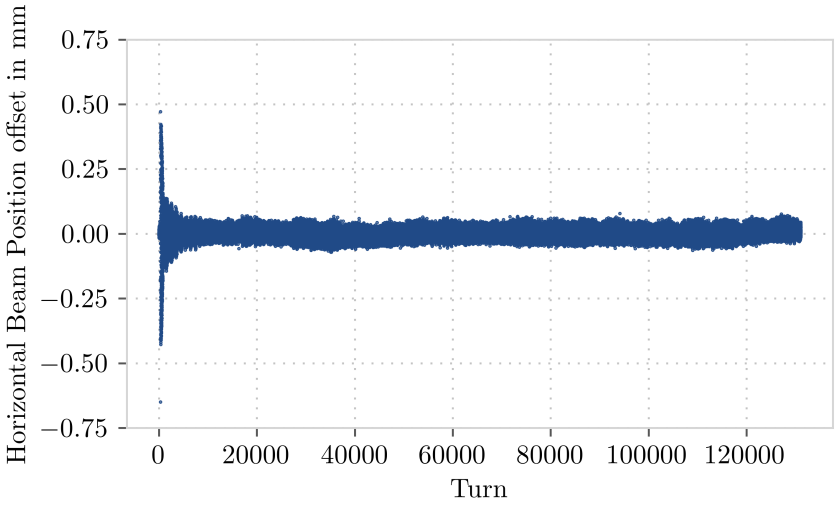

Figure 6.1: Beam position data after a horizontal kick with one of the injection kickers measured at a dispersive position for positive α_c. The horizontal chromaticity for this measurement is 0.6, which is the value currently used for normal injection. Shown is the offset of the beam position data as offset from the mean position over the full 2^{17} turns. A clear damping process is visible, followed by a relatively smooth beam that only shows effects consistent with coherent synchrotron motion.

At positive $\alpha_c \approx 9 \times 10^{-3}$ and 0.5 GeV the initial displacement of the kick results in a fast oscillation that is damped down to the level of regular oscillations present without a kick. A sample measurement for these settings is shown in Fig. 6.1.

In this case the chromaticity as well as the momentum compaction factor are positive resulting in the damping visible through the reducing position offset up to about 5000 turns. The remaining oscillations with an amplitude of about ± 0.05 mm result from synchrotron oscillations that lead to a slight shift of energy as well as the usual betatron oscillations. Together with the dispersion of about 0.17 m at the point of the recording BPM the energy shift leads to the visible horizontal position offsets.

The same kick has been recorded with reduced sextupole strengths that cause a negative horizontal chromaticity. This measurement is shown in Fig. 6.2a. After the strong initial oscillations directly after the kick are quickly damped no further reduction in oscillation amplitude is present. This is a clear difference to the previous case with positive chromaticity shown in Fig. 6.1. Furthermore, relatively strong oscillations of varying amplitude are visible that are not linked to coherent synchrotron motion. These oscillations could indicate additional effects that could be caused by non-damped head-tail motion as these arise for $\xi/\alpha_c < 0$.

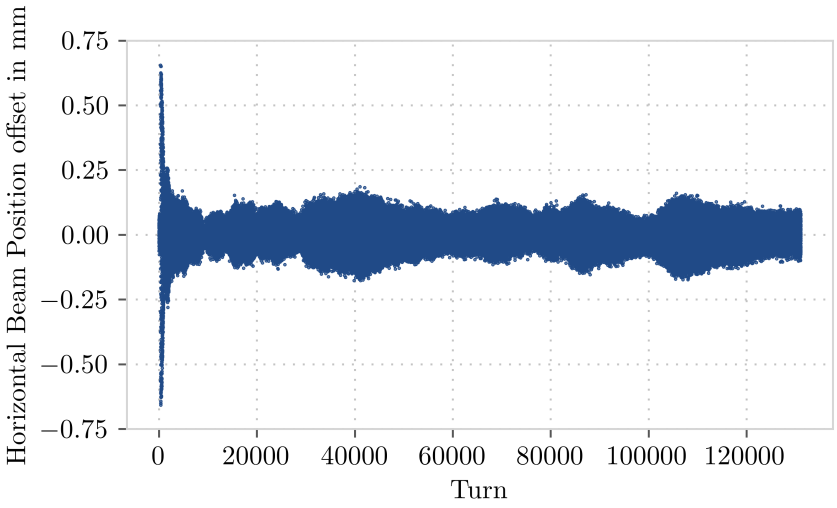

(a) With kick

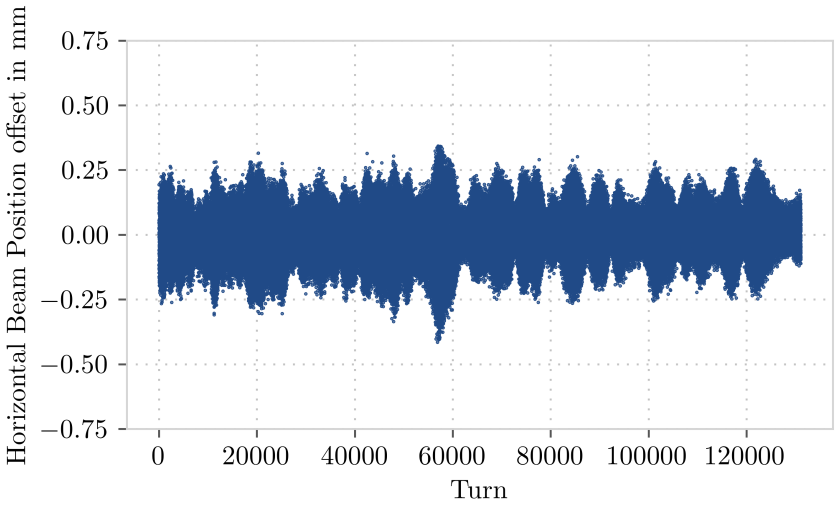

(b) Without kick

Figure 6.2: Beam position data after a horizontal kick with one of the injection kickers (top) and without a kick (bottom) measured at a dispersive position for positive α_c. The horizontal chromaticity for this measurement was set to a negative value of -0.8. Shown is the offset of the beam position data as offset from the mean position over the full 2^{17} turns. After the initial kick the most excessive oscillations are quickly damped but significant oscillations still persist that are varying in amplitude and are not directly linked to synchrotron motion as the frequencies do not match. Even without a kick significant oscillations with varying amplitude are visible in the bottom image.

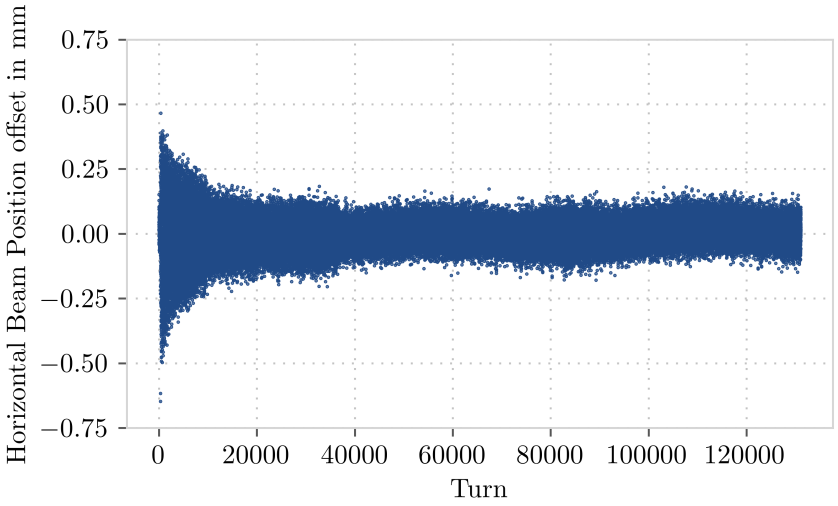

Figure 6.3: Beam position data after a horizontal kick with one of the injection kickers measured at a dispersive position for negative α_c. The horizontal chromaticity for this measurement was set to a negative value of -3.1. Shown is the offset of the beam position data as offset from the mean position over the full 2^{17} turns. A clear damping process is visible, followed by a relatively smooth beam that only shows effects consistent with coherent synchrotron motion.

For further investigation, a measurement without kick at negative chromaticity has been performed. The result is shown in Fig. 6.2b. In this measurement strong oscillations are visible that are, due to the lack of a kick, not artificially created. These oscillations vary in amplitude and are not linked to coherent synchrotron motion as again the frequency is higher. The fact that these oscillations arise strongly at $\xi/\alpha_c < 0$ and are not visible at $\xi/\alpha_c > 0$ matches with expected oscillations caused by head-tail motion.

One of the main ideas behind operation of light sources at negative α_c is the possibility to reduce the sextupole strengths in order to increase the dynamic aperture. Therefore, the negative α_c operation at KARA was implemented using a negative chromatiticy through greatly reduced sextupoles compared to the normal positive α_c operation. The beam position after a kick for these settings is shown in Fig. 6.3. After the horizontal kick a clear damping process is visible followed by a relatively smooth beam position. The remaining oscillations of about $\pm 0.1\,\mathrm{mm}$ are fairly constant and correspond to longitudinal oscillations due to coherent synchrotron motion. Compared to the same effect shown for positive α_c at positive chromaticity in Fig. 6.1 the oscillations caused by coherent synchrotron motion are enlarged for negative α_c. This is due to the fact that the dispersion is greatly enlarged and the value at the position of the BPM is a factor of about 7.3 larger at negative α_c with a an absolute value of about $1.25\,\mathrm{m}$. The lack of additional strong oscillations in this case indicates that the cause of the

effects present for negative chromaticity and positive α_c shown in Fig. 6.2b is not present for a negative sign of α_c. This in turn indicates that the possible head-tail motion is also not present when switching the sign of α_c from positive to negative for negative chromaticities, which is expected as then $\xi/\alpha_c > 0$ and oscillations should be damped. Therefore, it can be confirmed that the use of negative α_c allows to reduce the sextupole strength significantly without strong coherent beam oscillations and therefore allows operation at negative chromaticities.

6.2 Head-Tail Damping

The head-tail growth rate, according to Eq. (6.1), or in the case of damped head-tail motion the head-tail damping rate is depending on the number of particles in a bunch. Since the damping of an excitation is also caused by radiation damping, see Section 2.6, excitations are damped with an effective damping time. However, while the head-tail damping effect is current-dependent, the radiation damping effect is independent of bunch current. Therefore, measurements of the effective damping rate and its current dependency can be used as indication for the presence of head-tail effects in the damped case. If the effective damping rate shows a bunch current dependency, the damping effect is caused by the superposition of the radiation damping and a current-dependent damping effect. In the measurements shown here a bunch current dependency can therefore reveal the presence of head-tail effects.

From the beam position measurements described in the previous section, a damping rate can be extracted by fitting an exponential damping function to the excitation amplitude, see Section 5.1. For positive α_c and two positive values of the chromaticity the fitted damping rates at various bunch currents are shown in Fig. 6.4. The large spread of the measurement results for similar bunch currents is caused by the significant jitter on the beam position data as can be seen in the plots of the previous section. Nonetheless, a clear current dependency is visible. This dependency seems to be linear and results in an increased damping rate with increasing bunch current. Both, the linearity and direction of the dependency is in accordance with the expected current dependency of the head-tail effects as given in Eq. (6.1). Therefore, these measurements expose the existence of head-tail effects at positive α_c at KARA that lead to a damping effect. This is corroborated by the fact that the slope of the current dependency increases with increasing horizontal chromaticity as predicted in Eq. (6.1).

The same measurements were also conducted at negative α_c and two different negative values of the chromaticity. The results of the damping rate extraction are shown in

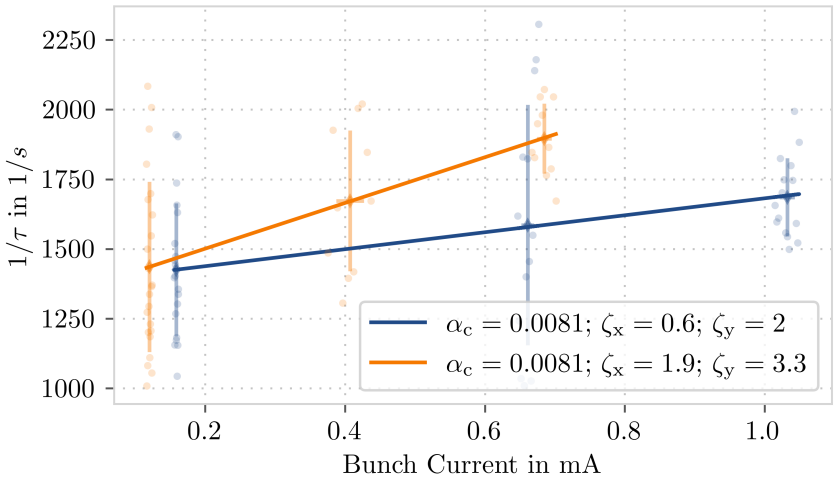

Figure 6.4: Bunch current dependency of the effective damping rate caused by the superposition of radiation damping and head-tail damping at positive α_c for two different values of the chromaticity. Each dot corresponds to the damping rate extracted from a single measurement after a horizontal kick. Solid lines show a linear fit of the damping rate as function of bunch current. As the measurements were done in three different current ranges each, the standard deviation of the determined damping rate for each bunch current range is also shown (vertical lines in the centre of the corresponding bunch current range).

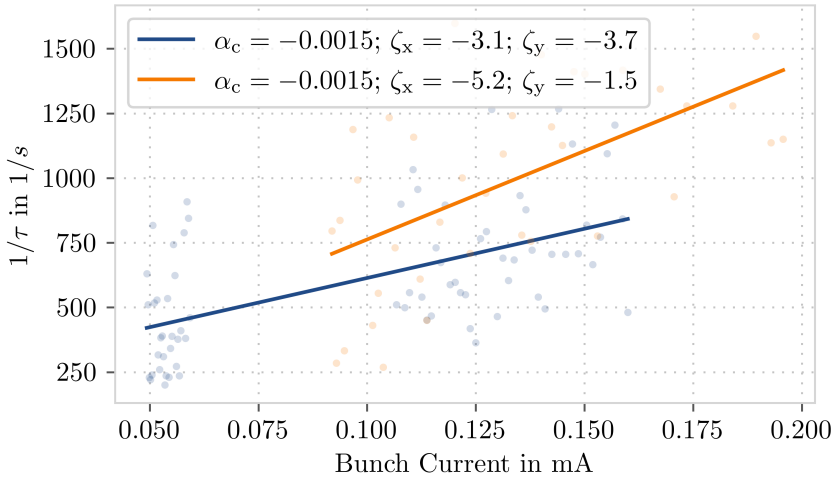

Figure 6.5: Bunch current dependency of the effective damping rate caused by the superposition of radiation damping and head-tail damping at negative α_c for different values of the chromaticity. Each dot corresponds to the damping rate extracted from a single measurement after a horizontal kick. Solid lines show a fit of the damping rate as function of bunch current for each value of the chromaticity.

Fig. 6.5. Similar to the measurements at positive α_c the damping rate at negative α_c shows a current dependency. The existence and direction of the bunch current dependency is in accordance with the expectation for negative chromaticity at negative α_c from Eq. (6.1). This is therefore a strong indication that at negative α_c the head-tail effects are present and result in a damping effect for negative values of the chromaticity.

The presented measurements at positive and negative α_c show a current-dependent damping effect after the excitation by a horizontal kicker. In both cases the current dependency is in accordance with the expectation from head-tail effects as in both cases the chromaticity and α_c were of the same sign. For both signs of α_c the slope of the current dependency of the damping rate increases with increasing absolute value of the horizontal chromaticity which fits to Eq. (6.1) and is therefore another indication for the presence of head-tail effects. This means the negative α_c mode successfully allows the reduction of sextupole magnets strengths that result in a negative chromaticity without the danger of head-tail excitation and beam loss.

7 Bunch Length

In a synchrotron there is the concept of the natural bunch length, as described in Section 2.6. This is the bunch length at very low bunch currents originating from the equilibrium between excitation through statistically emitted photons and the resulting damping effect. At higher currents however the natural bunch length is only an indication of the actual bunch length. Through various effects such as Coulomb forces or interactions of electrons with their surroundings, the bunch length changes. Counteracting a possible increase in bunch length is the effect of phase focusing as described in Section 2.3. This chapter discusses the differences expected and observed for the bunch length at positive and negative α_c. The main results presented in this chapter have also been published in [Sch22, Sch21].

The equilibrium bunch length in an electron storage ring is influenced by phase focusing which in turn is depending on the gradient of the electric potential seen by the individual particles. The simplest approach would only consider the RF potential, as is done for the bunch length in the zero current limit in Eq. (2.31). This simplification results in no bunch length changes over current as the potential is constant. However, this changes when taking the longitudinal wakefields, generated by the interaction of the bunch with its environment, into account. Thus, the effective potential V_{eff} as the sum of RF potential and wakefields[1] is considered

$$V_{\text{eff}}(I) = V_{\text{RF}} + V_{\text{Wake}}(I). \tag{7.1}$$

As the wakefield of a bunch is dependent on the bunch charge so is the effective potential, which means the bunch length is changing with bunch current I.

The wakefields can be calculated from the longitudinal bunch profile and the impedance. Since the underlying form of the longitudinal bunch profile is a Gaussian shape for positive and negative α_c the underlying form of the wakefields is the same in both cases. Especially at low currents where the deformations of the profile caused by the wakefields are weak the total wakefields for positive and negative α_c are similar.

[1] A similar concept was used to study the synchrotron motion during the micro-bunching instability in [Bol19].

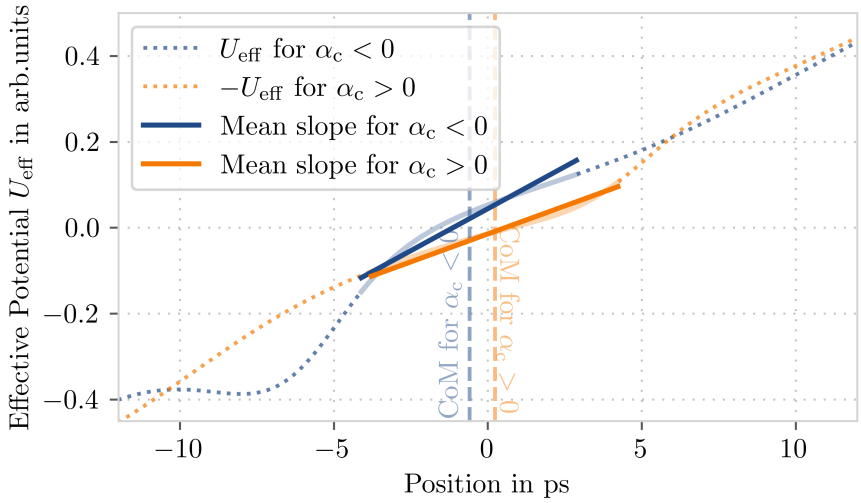

Figure 7.1: Effective potential of a sample case for positive and negative α_c. The potential for positive α_c was flipped in the display to simplify comparison. Here the dotted lines represent the effective potential while the solid, light lines represent the potential in the area where the bunch is located. The solid, intense lines show the average gradient over the bunch as an aide. Two dashed, vertical lines indicate the location of the center of mass for both signs of α_c. The wakepotential used here was calculated with Inovesa [Sch19a] using the CSR parallel plates impedance.

In order to maintain phase focusing, operation with negative α_c uses an RF phase shifted by about π, which means the RF potential is reversed with respect to the one experienced by a bunch during operation at positive α_c. This results in a different gradient of the effective potential V_{eff} and therefore in a different bunch length.

Considering the CSR parallel plates impedance for short bunches, as this is the dominant impedance at KARA (due to small absolute values of α_c), the average gradient of the effective potential is larger for negative than for positive α_c at low currents. In fact, at negative α_c it is larger than for the unperturbed pure RF potential and smaller at positive α_c. An example is shown in Fig. 7.1 where the potential for positive α_c is flipped vertically to simplify the comparison. It is clearly visible that the line representing the average gradient for negative α_c is steeper compared to the one for positive α_c in the area where the bunch is located. Since with increasing current the wakepotential increases, the average gradient of the effective potential increases for negative α_c and decreases for positive α_c. Consequently, the bunch length should increase with current for positive α_c and decreases for negative α_c.

It is therefore expected to observe a different current-dependent behaviour of the bunch length for different signs of α_c.

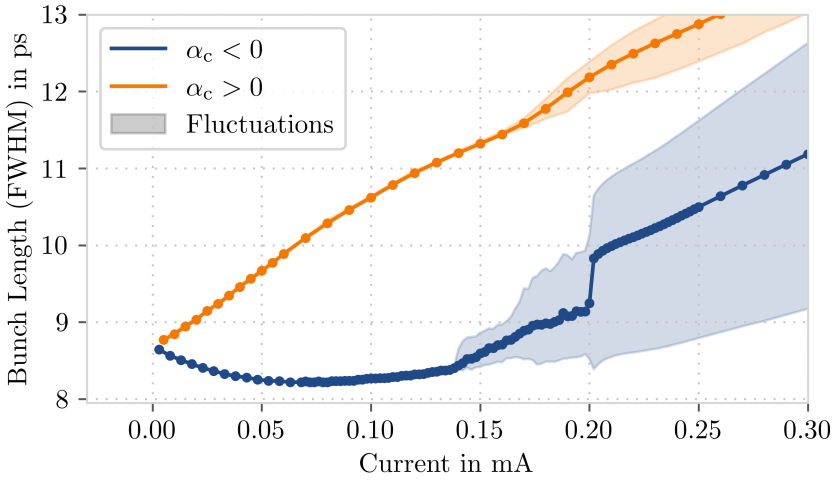

Figure 7.2: Bunch length simulated with Inovesa for both signs of α_c with the same absolute value. Solid lines denote the mean bunch length over time while the shaded area denote the fluctuation region over time.

7.1 Simulations

Most experiments conducted in this thesis use a low absolute value of α_c during negative α_c operation at KARA (in the order of 10^{-4}), as this means a less extreme dispersion. This also makes measurements and experiments comparable to existing ones at positive α_c, which were mostly conducted at low absolute values of α_c as well. Beam stability and again comparability to existing measurements at positive α_c are the reason why the studies in this section focus on an energy of 1.3 GeV. Therefore, only the case of short electron bunches is considered in the following section. Previous studies at positive α_c have shown that for short bunches at KARA the parallel plates CSR impedance is the most prominent longitudinal impedance present [45].

Using Inovesa [Sch19a], see also Section 5.7, the charge distribution in the longitudinal phase space was simulated with the same absolute value $|\alpha_c| \approx 4 \times 10^{-4}$ once for a positive and once for a negative sign of α_c.

Inovesa simulates a given time range for a fixed bunch current, therefore one simulation run was performed for each bunch current. The bunch length is calculated as full width half maximum from the resulting bunch profiles and averaged over time for each simulated bunch current. The fluctuation range is calculated above and below the mean individually by calculating the standard deviation with respect to the overall mean for just the data points above or below the mean respectively.

The resulting bunch length as function of bunch current is shown in Fig. 7.2. For positive α_c it is clearly visible that the bunch length increases with current. This confirms

the expectation in this case as the wakepotential effectively lowers the gradient of the effective potential.

However, for negative α_c at low currents the bunch length shows bunch shortening. For those low currents the bunch profile is almost of Gaussian shape and almost identical for positive and negative α_c, apart from the aforementioned difference in bunch length. Therefore, also the wakepotential is similar. Due to the reversed RF voltage necessary at negative α_c the gradient of the effective potential is increased there. This results in lower bunch lengths. For low bunch currents, the bunch profile is only slightly distorted compared to a Gaussian shaped profile. Therefore, in the shown simulation approximately up to 0.06 mA, the wakepotential roughly scales with bunch current. Hence, the bunch length reduces with current as seen from the simulation in Fig. 7.2. Similar results for bunch shortening were found in [51] where they considered wakefields resulting from geometric and resistive wall effects.

At higher currents the bunch is deformed due to the self-interaction with its own wakefield. This perturbs the previous behaviour by changing the shape of the wakefield and leads to an increase in bunch length. While at low currents no fluctuations in the bunch length are visible this is not the case at higher currents. Such fluctuations were already seen in [52] and in conjunction with coherent synchrotron radiation emission bursts in [53]. For positive α_c these fluctuations start at roughly 0.160 mA and for negative α_c they start at about 0.137 mA for the simulated parameters. More on the instability and the bunch current where the fluctuations start is addressed in Chapter 8. These fluctuations are caused by the micro-bunching instability, which leads to non-static deformations of the bunch profile [53]. For negative α_c at about 0.20 mA a sharp increase in bunch length is visible. This is due to a change of the behaviour of the instability, which manifests in even larger deformations of the bunch profile and corresponding bunch length. A closer inspection of the instability is given in Chapter 8.

The simulations presented above confirm the expectation of different current-dependent bunch length for positive and negative α_c arising from the inverted slope of the RF voltage. A shorter bunch length has been observed at negative α_c compared to positive α_c over the entire shown bunch current range. Additionally, at lower bunch currents the bunch length at negative α_c decreases with increasing bunch current which again is in accordance to the expectation from theoretical considerations. Furthermore, a bunch length increase has been observed even at negative α_c due to deformations of the bunch profile and wakefields. Coupled with the occurrence of an instability caused by these deformations abrupt changes of the bunch length were observed at negative α_c. The observations in this chapter were based on simulations using the parallel plates CSR

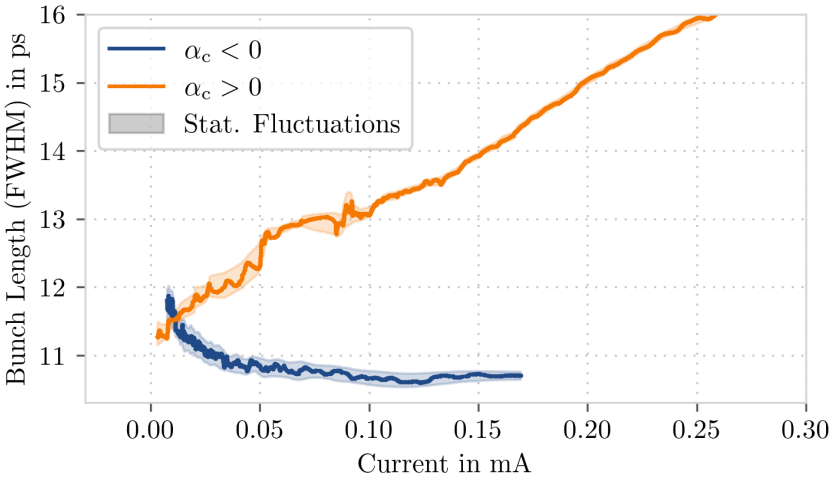

Figure 7.3: Bunch length measured using a streak camera for positive α_c and negative α_c with the same absolute value of α_c. Solid lines represent a moving average and the shaded areas represent the statistical fluctuations calculated from multiple measurements for similar currents. The discrepancy of the bunch length towards zero current is discussed in Section 7.3.

impedance and could differ when considering different impedances. The behaviour in measurements will be presented in the following section.

7.2 Measurements

Bunch length measurements were conducted for the same absolute value of α_c as used in the simulations for positive as well as negative α_c. All measurements were performed during single-bunch operation to exclude effects of bunch interaction or overlapping images on the streak camera. The measurements were conducted using the techniques described in Section 5.2 at a beam energy of 1.3 GeV. Every 10 s a sequence of 100 pictures was taken during the natural current decrease. Each sequence took roughly 8 s. The full width half maximum bunch lengths after center-of-mass movement correction is calculated for the average bunch profile of each sequence. The results are shown in Fig. 7.3.

Solid lines in Fig. 7.3 refer to a moving average of the bunch length. Shaded areas display the statistical fluctuations calculated as moving standard deviation from a few points[2] for very similar bunch currents assuming the bunch length changes slowly compared to the acquisition repetition rate.

[2]This was chosen as 10 sequences around the corresponding sampling point in a trade-off between low current variation and good statistics for the standard deviation calculation.

At positive α_c the measured bunch length increases with increasing bunch current. For the measured current range the bunch length seems to be roughly linear in current. The measurement at negative α_c shows a completely different behaviour, as it decreases at very low currents. Towards higher currents the bunch length stabilises and shows a roughly constant evolution over current. Above about 0.12 mA an increase in bunch length could be assumed. However, no clear statement can be derived from the data, as the current range of the measurement is limited, due to the limited injectable current (Section 4.3) as well as the time necessary for ramping. Measurements at UVSOR [54] and at the Diamond Light Source [2] gave similar results with a bunch length decrease at low currents followed by a bunch length increase towards higher currents at negative α_c.

Since the slow time axis of the streak camera is chosen to resolve the synchrotron oscillation it cannot resolve single turns. Therefore, the bunch length fluctuations seen in simulations can not be seen in these measurements. However, parallel measurements with KAPTURE and a Schottky diode (see Section 5.3) show that the micro-bunching instability occurred above approximately 0.150 mA for positive α_c, these measurements are presented in Chapter 8. For negative α_c a threshold of the instability at about 0.08 mA was observed. Due to the limited injectable current, described in Section 4.3, and the low lifetime at injection (0.5 GeV) coupled with the time it takes to ramp up the energy (to 1.3 GeV), it was not possible to measure up to higher beam currents in the negative α_c measurements.

7.3 Comparison

Similar to the simulations the positive α_c bunch length increases with current approximately linearly in the measurements. In the area round 0.05 mA and 0.1 mA an additionally increased bunch length was measured. For some conditions (combination of synchrotron frequency and accelerating voltage) resulting in short natural bunch lengths in the order of $\sigma_{z,0} \lesssim 2\,\mathrm{ps}$ (RMS) an additional instable region at low currents has been observed at positive α_c [Bro19b]. This additional instable region could lead to an increase in bunch length. However, the conditions used here (calculated natural bunch length: $\sigma_{z,0,\mathrm{FWHM}} \approx 8.59\,\mathrm{ps} \mathrel{\hat{=}} \sigma_{z,0,\mathrm{RMS}} \approx 3.65\,\mathrm{ps}$) are not expected to result in such an instable region. Another possibility are effects caused by the measurement setup and the analysis performed to determine the bunch length. Temporal changes in the strength of the synchrotron motion, for example, could affect the centre of mass correction and lead to an over or under estimation of the bunch length. Such changes to

the synchrotron motion were previously observed for example for slight variations in the cavity temperatures.

Apart from the localised increase, a general offset of about 2 ps between measurement and simulation is observed. As the correction for centre of mass motion is not perfect a remaining contribution could overestimate the measured bunch length. One of the main causes of centre of mass motion is the synchrotron motion.

The measured bunch length for negative α_c displays a bunch shortening for low bunch currents similar to the shortening seen in simulations. For almost zero current the bunch length for negative α_c seems to be higher than for positive α_c which is not expected from both simulations and theoretical considerations. This effect hints at an offset between the bunch length measurements for the two signs of α_c. It was previously observed, that the synchrotron motion has a higher amplitude at negative α_c. Due to the possibly non-perfect centre of mass correction during the analysis this could explain the additional offset of the measured bunch length between positive and negative α_c.

Further discrepancies have been observed at currents where the longitudinal instability is present the measurements suggest a much smaller influence of the instability on the measurements compared to the influence of the instability on the bunch length in simulations. Particularly at negative α_c an increase in bunch length is expected from simulations at the onset of the instability (measured at about 0.08 mA, see Chapter 8), but almost no increase is visible in the measurements. Slightly above the instability threshold current however a kink in the measurements leading to a slight increase in bunch length could be seen at about 0.12 mA, however this is very weak and well within the estimated fluctuation error-band.

However, for the most part of the current range, the general shape of the measured bunch length over current at positive and negative α_c fits quite well to the simulations. Both show bunch shortening at low currents for negative α_c and a bunch length increase at positive α_c over the entire current range. This good agreement also indicates a good fit of the impedance model used for the simulations.

It seems in general that the bunch length at negative α_c is shorter compared to positive α_c. This has to be taken into account when considering negative α_c operation in new or existing machines. The shorter bunch length can be useful if e.g. experiments require short pulses, however it can also lead to problems such as instabilities. One such instability has been observed at KARA and will be discussed in the next chapter.

8 Longitudinal Instability

At positive α_c as well as negative α_c an instability has been observed above a certain threshold current which manifests not in particle loss, but intensity fluctuations of the coherent synchrotron radiation (CSR) emitted by the beam. For positive α_c the instability was identified as the micro-bunching instability by synchronous measurements of the energy spread, longitudinal bunch profile and CSR intensity and is introduced in the next section. The reason why the same mechanism could be different for negative α_c is explained as well. Indications of the different aspects of the observed instability can be seen on the raw measurement data in time domain of the CSR intensity which is described in Section 8.2. The aspects seen there will be investigated in the sections thereafter in more detail, such as the current-dependent behaviour, the repetition rate of outbursts of intensity caused by the instability and the intensity of the emitted CSR. Furthermore, the effects on the pulse arrival time and the energy-dependence of the observed instability will be discussed. Part of these results have also been published in [Sch22].

8.1 Micro-Bunching at Positive α_c

Reducing the absolute value of the momentum compaction factor leads to shorter bunches. This increases the spectral range of emitted coherent synchrotron radiation (CSR) up to higher frequencies. The emitted CSR intensity scales with the number of emitting particles squared. This intense radiation can enable significant interaction between the bunch and its emitted radiation leading to structures in the longitudinal phase space (spanned by longitudinal position and energy). This subsequently leads to sub-structures on the longitudinal bunch profile, which is the projection of the charge density in the longitudinal phase space on the space dimension. An example phase space density at positive α_c simulated with Inovesa is shown in Fig. 8.2a. Since these structures are short they lead to CSR emission at even higher frequencies and therefore result in further self-interaction of the bunch with its radiation. As the charge density rotates in phase space, see Section 2.4, the resulting structures on the longitudinal bunch profile continuously change over time, leading to temporal fluctuation of the CSR intensity.

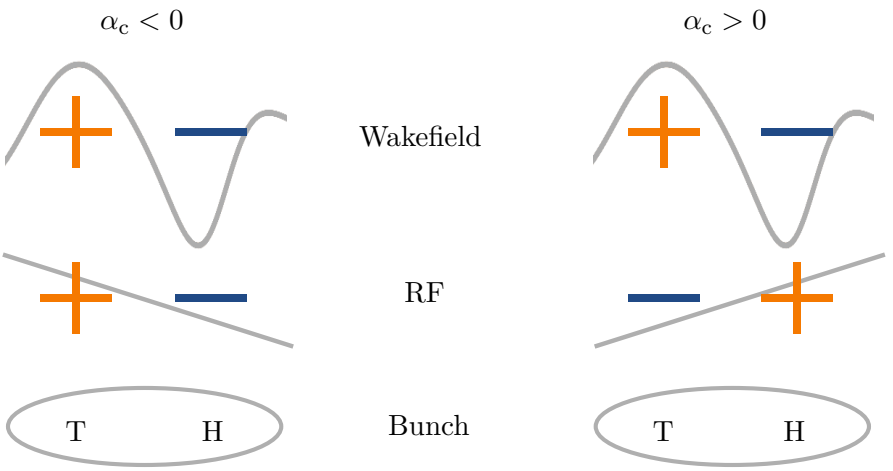

Figure 8.1: Sketch of the energy gain differences at head and tail for positive and negative α_c based on an example wakefield and the RF voltage. Shown is whether particles gain (+) or loose (-) energy at the head (H) and tail (T). In gray in the background a wakefield and RF voltage sketch are shown where higher values represent energy gain.

The substructures lead to a lengthening of the bunch. As the driving self-interaction for these sub-structures is then reduced, a smearing out of the sub-structures happens. The new smoother bunch profile leads to a bunch shortening again, due to radiation damping, and thus the CSR interaction increases again resulting in growing sub-structures. After reaching a critical bunch length a cycle evolves and the process starts anew by lengthening the bunch again. It is important to note that this instability does not necessarily lead to immediate beam loss. A more detailed description of the micro-bunching instability is given in [38].

This instability has been thoroughly studied for the positive momentum compaction regime e.g. in [26, 55, 56] (for an overview see [38]). The interaction between the bunch and its radiation can be described by wakefields produced by the emitted radiation. These wakefields are longitudinally not symmetric around the centre of the bunch as seen e.g. in Fig. 2.10 in Section 2.7. With a typical bunch shape this results in an energy loss in areas towards the head of the bunch and gain in areas towards the tail of the bunch. This is illustrated in Fig. 8.1 in the top row. For positive α_c the RF voltage leads to a relative energy gain at the head of the bunch and to relative energy loss at the tail compared to the synchronous particle. For negative α_c, however, it is the other way around. The net energy change of the head and tail of the bunch is therefore different for the two signs of α_c (see Fig. 8.1). The reversed RF voltage also leads to the previously described dependency of the rotation direction of the phase space density of a bunch in a synchrotron on the sign of α_c. The rotation direction is visualised in Fig. 8.2. Together

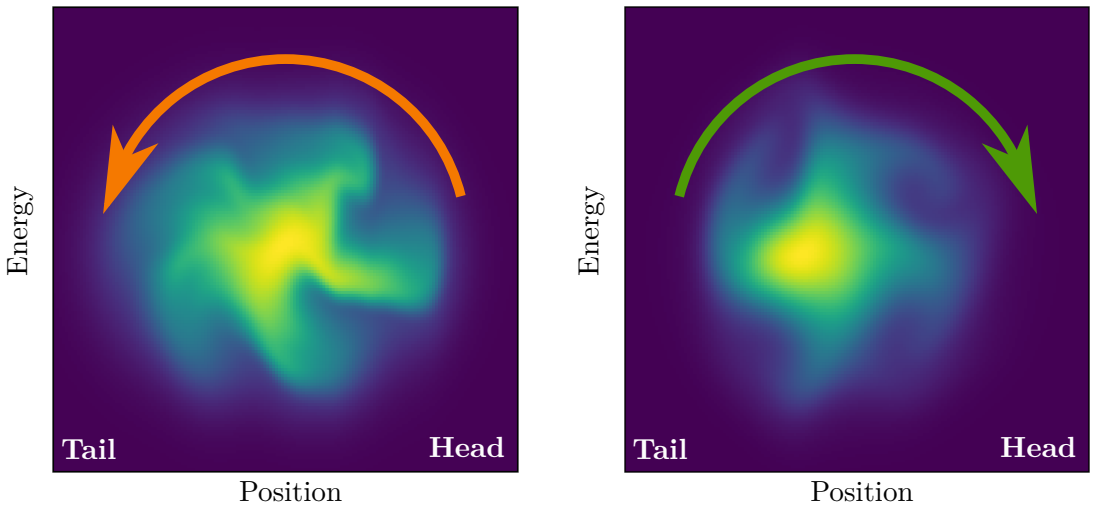

(a) $\alpha_c > 0$ (b) $\alpha_c < 0$

Figure 8.2: Examplary simulated charge densities in the longitudinal phase space at positive α_c (a) and negative α_c (b). The substructures on the charge density are clearly visible. In this visualisation the head of the bunch is to the right and the tail to the left side. The rotation direction for both signs of α_c is shown as well.

with the asymmetric wakefields a different behaviour caused by the CSR self interaction is expected for a change in sign of α_c. Figures 8.2a and 8.2b show a simulated example charge density in the longitudinal phase space at positive and negative α_c respectively. In both cases the structures point roughly in rotation direction, however, as this direction is reversed at negative α_c the structures point in the other direction compared to positive α_c. Furthermore, the area with the highest particle density is shifted towards the head of the bunch at positive α_c and towards the tail of the bunch at negative α_c. While both charge densities show similarities such as structures pointing outwards, already from these simple illustrations differences are visible. The consequences of this will be discussed in the following sections.

8.2 Observed Dynamics in emitted CSR

The emitted CSR intensity exhibits interesting features during the occurrence of the instability at positive α_c as well as negative α_c. The behaviour is depending on bunch current and the actual value of α_c amongst other parameters. In Fig. 8.3 a typical time domain signal of the peak intensity emitted at each turn observed at positive α_c is shown for a current well above the instability threshold. The measurement method is described in Section 5.3. There are times with increased radiation intensity called “bursts”. The

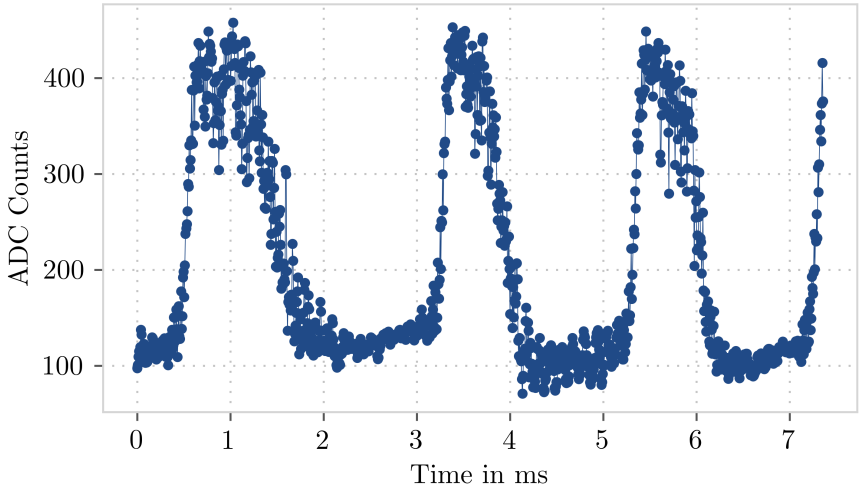

Figure 8.3: Time domain measurement of the CSR radiation intensity for positive α_c. The values are displayed as ADC counts from the data acquisition system KAPTURE since the detection chain is not calibrated. Clearly visible are the outbursts of intense radiation. Between these bursts the intensity slowly raises until the next outburst rapidly increases the intensity.

temporal development of the radiation intensity can be linked to the individual steps in the explanation before. The bursts occur when the bunch is short and the substructures on the phase space density, and therefore on the longitudinal bunch profile are strong. The decrease at the end of the bursts is linked to the smearing out of the substructures which reduces the form factor and reduces the emitted CSR intensity. Between the bursts the intensity slowly increases until a sharp raise is visible and the next burst occurs. This slow increase happens during the bunch shortening phase described in the previous chapter and the sharp increase is caused by the occurrence of the substructures on the phase space density. Due to the described relation to the temporal development of the phase space density, the CSR intensity reveals insights into the dynamics happening in the phase space and is thus an important tool in characterising and understanding the dynamics during the instability. The following chapters will be based on CSR intensity data measured at positive and negative α_c which at KARA is emitted in the low THz regime (80 GHz to 1 THz).

The case for negative α_c is shown in Fig. 8.4, where bursts are visible as well. However, while at positive α_c slow increases between bursts and sharp increases at the beginning of the bursts were visible, at negative α_c fast increases between the bursts are followed by a short, sharp increase at the beginning of the bursts. After the burst the steepness of the drop in intensity is of the same order of magnitude as the steep increase for both signs of α_c. Furthermore, the repetition rate of the bursts is visibly lower at negative

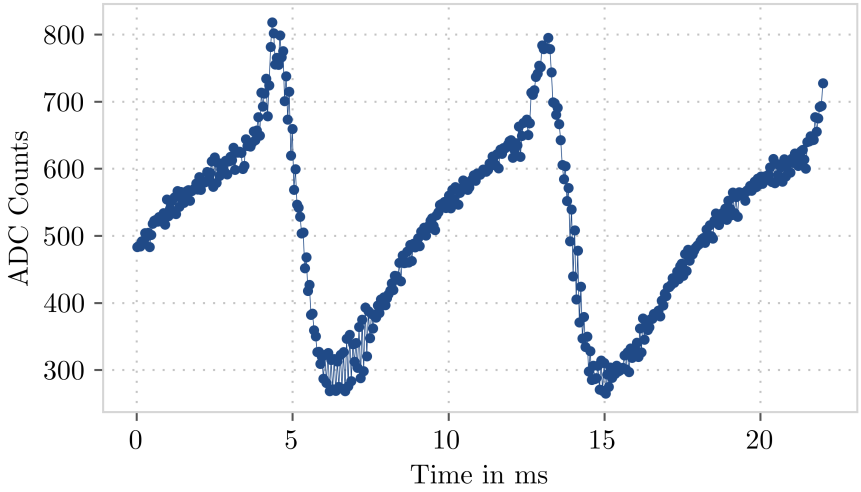

Figure 8.4: Time domain measurement of the CSR radiation intensity for negative α_c. The values are displayed as ADC counts from the data acquisition system KAPTURE since the detection chain is not calibrated. Clearly visible are the outbursts of intense radiation. Between the burst the intensity raises and quickly drops at the end of each burst.

α_c compared to positive α_c. Nevertheless, the occurrence of bursts and roughly similar behaviour between positive and negative α_c indicates a similar behaviour in phase space as described for positive α_c in the previous chapter for negative α_c as well. This hints at a similar cause of the instability observed at positive and negative α_c.

In Fig. 8.5 and Fig. 8.6 measurements of the CSR intensity in time domain for various bunch currents at the same momentum compaction factor but with different signs are shown. From this the current-dependent behaviour is clearly visible. The different temporal structure and lower repetition rate of bursts at negative α_c is also clearly visible from these plots. For positive α_c the shape of the bursts seen in the panels for the five highest bunch currents in Fig. 8.5 seems to change significantly. In contrast to that the bursting behaviour for negative α_c seen in the four top panels in Fig. 8.6 does not drastically change in shape. Note the plots for positive α_c in Fig. 8.5 show a bigger current range than the plots for negative α_c in Fig. 8.6. Nevertheless, when considering a range of e.g. 0.02 mA right above the lowest current where the bursts occur (≥ 0.15 mA for positive α_c and ≥ 0.12 mA for negative α_c) a significant change in the shape of the bursts is visible for positive α_c while almost no change is visible for negative α_c. Even when considering the whole shown current range above 0.12 mA at negative α_c the visible changes are almost negligible.

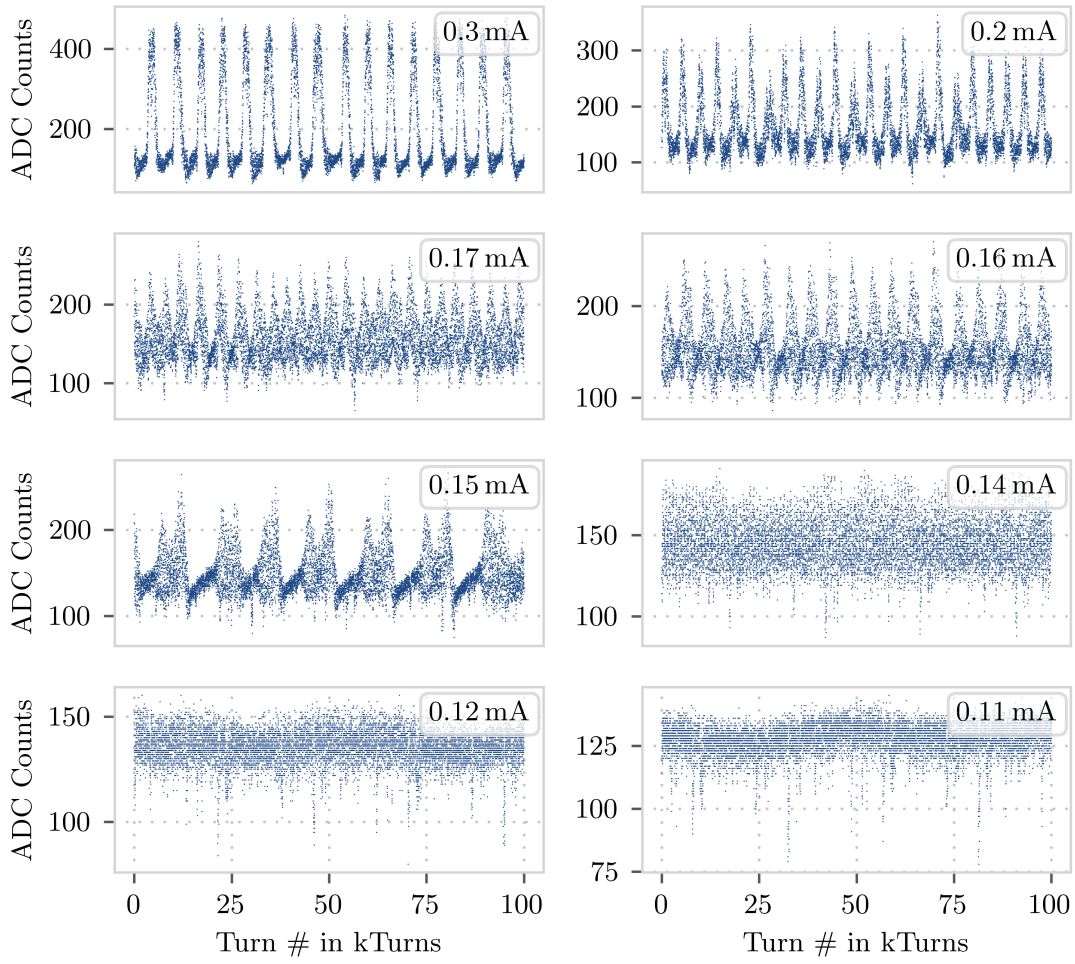

Figure 8.5: Time domain measurements of the THz radiation intensity for a measurement at a positive momentum compaction factor of $\alpha_c \approx 3.90 \times 10^{-4}$ at various bunch currents. Visible is the different behaviour for high and low bunch currents.

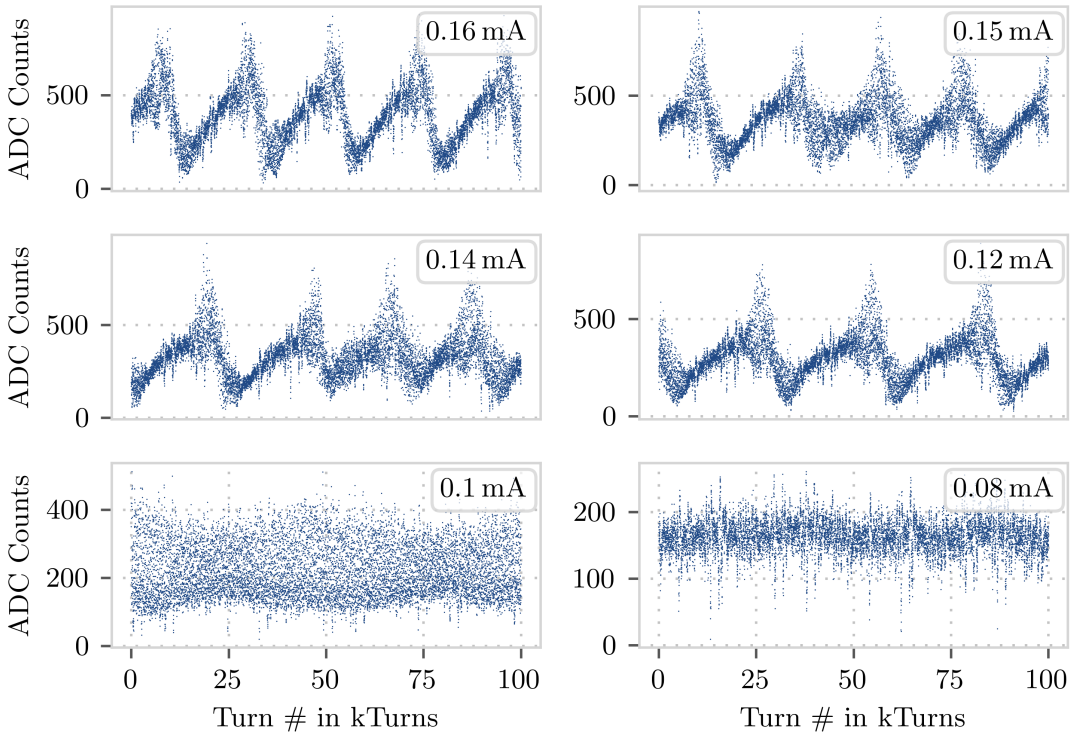

Figure 8.6: Time domain measurements of the THz radiation intensity for a measurement at a negative momentum compaction factor of $\alpha_c \approx -3.99 \times 10^{-4}$ at various bunch currents. Visible is the different behaviour for high and low bunch currents.

It is also visible that the bursts vanish for low bunch currents, however, the current at which they disappear is different. At negative α_c the bursts seem to be present for lower bunch currents than at positive α_c.

The current-dependent behaviour will be discussed in sections 8.3 and 8.4 in more detail. The higher repetition rate of the bursts for positive α_c compared to negative negative α_c will be discussed in Section 8.5. The minimum and maximum ADC counts are also higher at negative α_c than at positive α_c. This will be discussed in Section 8.8.

8.3 Current Dependency

A useful and widely used technique [38] to visualise the current-dependent dynamics during a longitudinal instability leading to CSR emission is the use of CSR intensity fluctuation spectrograms. Employing the techniques described in Chapter 5 a set of CSR measurements consisting of multiple data sets corresponding to different bunch currents was acquired for each setting, such as α_c and acceleration voltage at an energy of 1.3 GeV. By calculating the fast Fourier transform and displaying as function of bunch current the current-dependent frequency content of the fluctuations in the CSR intensity can be visualised in so-called spectrograms as seen in Fig. 8.7. Each horizontal line corresponds to one measurement[1] and the width of each line is determined by the bunch current at the time of measurement (lower edge) and the next higher current for which a measurement exists (upper edge). This technique was already used for analysis of the micro-bunching instability [55, 56, 27]. A typical spectrogram measured at positive α_c is shown in Fig. 8.7. Certain characteristic features of the instability are visible. An important feature is the threshold of the instability, which is the bunch current below which close to no fluctuations are observed (e.g. 0.115 mA in Fig. 8.7). Further visible features include the frequency of the fluctuations at the threshold (e.g. 25.4 kHz in Fig. 8.7) and the current-dependent behaviour of the dominant fluctuation frequencies.

Measurements at equivalent parameters but negative sign of α_c were conducted and the corresponding spectrogram is shown in Fig. 8.8. This spectrogram differs drastically from the one in Fig. 8.7 for positive α_c. While both show a threshold of the instability (0.089 mA at negative α_c in Fig. 8.8), for positive α_c the structure starting from the threshold upwards changes greatly over current and the equivalent structure for negative α_c just broadens a little with higher currents. It is important here to note that due

[1] CSR intensity signal measured over 1 s for one bunch.

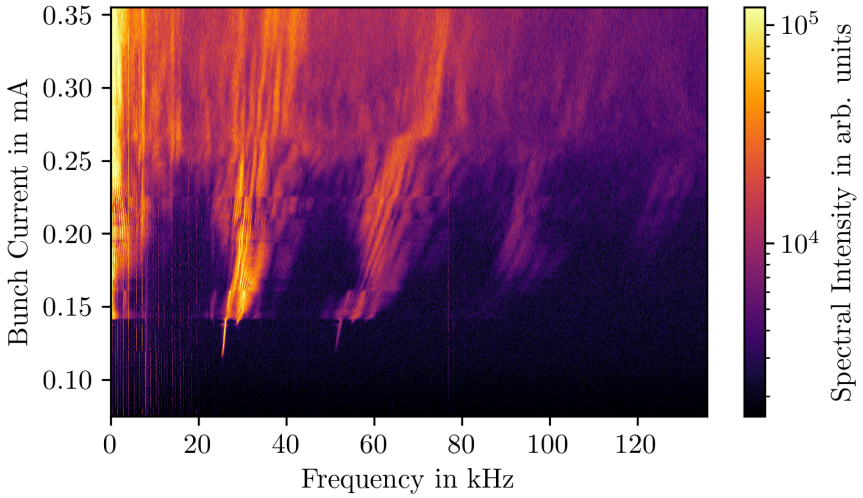

Figure 8.7: CSR intensity fluctuation spectrogram measured at positive α_c for an accelerating voltage of 1000 kV and $\alpha_c = 3.90 \times 10^{-4}$. The spectrogram shows the fluctuation frequencies of the emitted CSR intensity as a function of bunch current, allowing an insight into the dynamics under the micro-bunching instability.

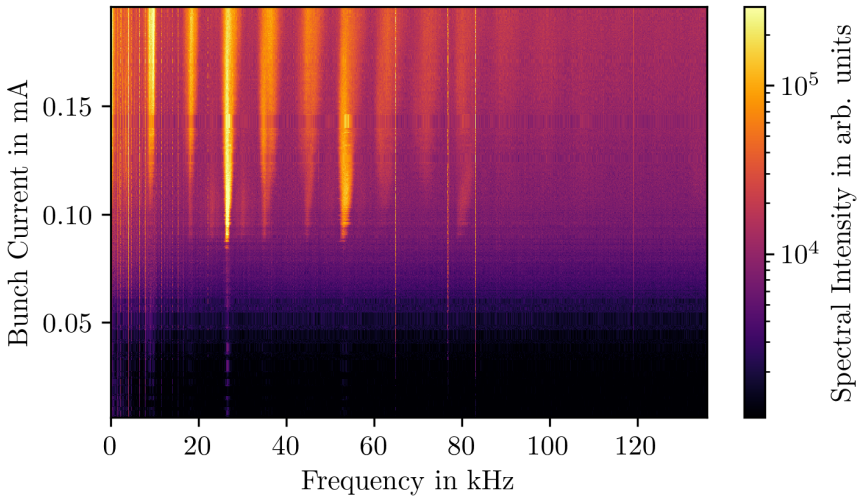

Figure 8.8: CSR intensity fluctuation spectrogram measured at negative α_c for an accelerating voltage of 1000 kV and $\alpha_c = -3.99 \times 10^{-4}$. This spectrogram was acquired as snapdecay measurement, which is a new measurement method developed in the framework of this thesis, see Section 5.4.

to technical difficulties[2] the measurements for negative α_c are limited in current range and do not reach as high currents as the measurements for positive α_c. Measurements at the Diamond Light Source [57] show a similar change from complex structures to more or less simple vertical lines when switching from positive to negative momentum compaction factors. This strong difference in the measurements at positive and negative momentum compaction factors hints at a different behaviour in the longitudinal phase space. Furthermore, the spectrogram shows that the dynamics are relatively independent on the bunch current over the measured region. This observation leads to the conclusion, that while different bunch currents lead to different strengths of the wakefield, this does not seem to affect the evolution of the phase space density. At positive α_c this is not the case and the dynamics strongly depend on the bunch current and therefore on the strength of the wakefield. Therefore, at negative α_c, it seems the wakefield only increases in strength with increasing bunch current without modifying and distorting its shape as is seen for positive α_c.

The behaviour at positive α_c seen in Fig. 8.7 is caused by the micro-bunching instability and can be completely described by longitudinal beam dynamics [38]. The negative α_c measurements in Fig. 8.8 show a different behaviour to the positive α_c ones. Based on these measurements alone no definitive statement can be given whether the differences are caused directly by the different sign of α_c, by longitudinal effects that are not considered in the micro-bunching instability or by completely unrelated effects that might be present. To further investigate if the differences are caused by the change in sign of α_c simulations with Inovesa were made. These purely longitudinal simulations, shown in Fig. 8.9 and Fig. 8.10, for both signs of α_c agree and differ from each other in similar ways than the measurements. This strongly indicates a mostly longitudinal cause of the dynamics seen at negative α_c and limits the possible causes to the effects simulated with Inovesa which is dominantly the interaction of the bunch with the RF and the self interaction due to coherent synchrotron radiation. Furthermore, as between the simulations only the sign of α_c was changed, the simulations indicate, that the observed behaviour changes are indeed mostly caused by the change in sign of α_c. Additionally, the simulations at higher bunch currents (0.2 mA to 0.5 mA) reveal more complex dynamics also in the negative α_c case.

At a slightly higher bunch length, measurements show a change in the width of the dominant structure. Figure 8.11 shows a zoom-in into the relevant spectrogram where the change is visible at about 0.153 mA. This could hint at more complex behaviour

[2] As described in Section 4.3 the bunch current for these measurements was limited. Furthermore, did the ramping procedure result in some additional bunch current reductions, mostly as the lifetime before and at the beginning of the ramp was quite low.

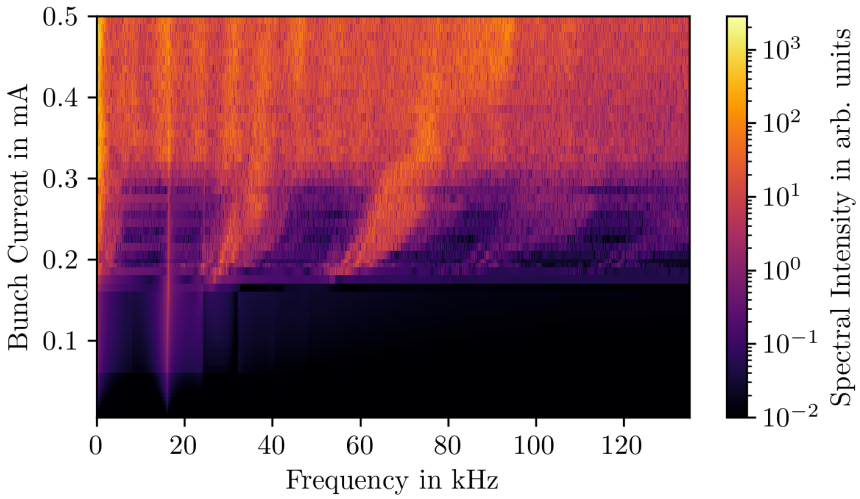

Figure 8.9: Simulated CSR intensity fluctuation spectrogram at positive α_c for an accelerating voltage of 1000 kV and $\alpha_c = 3.95 \times 10^{-4}$

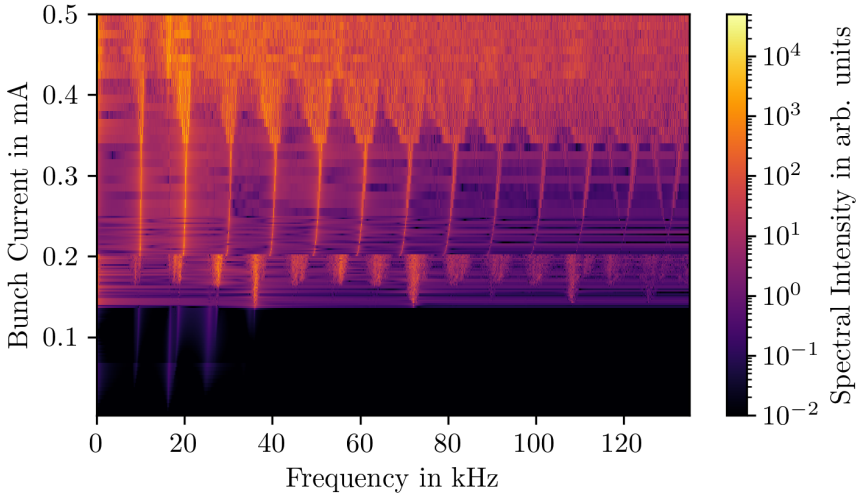

Figure 8.10: Simulated CSR intensity fluctuation spectrogram at negative α_c for an accelerating voltage of 1000 kV and $\alpha_c = -3.95 \times 10^{-4}$

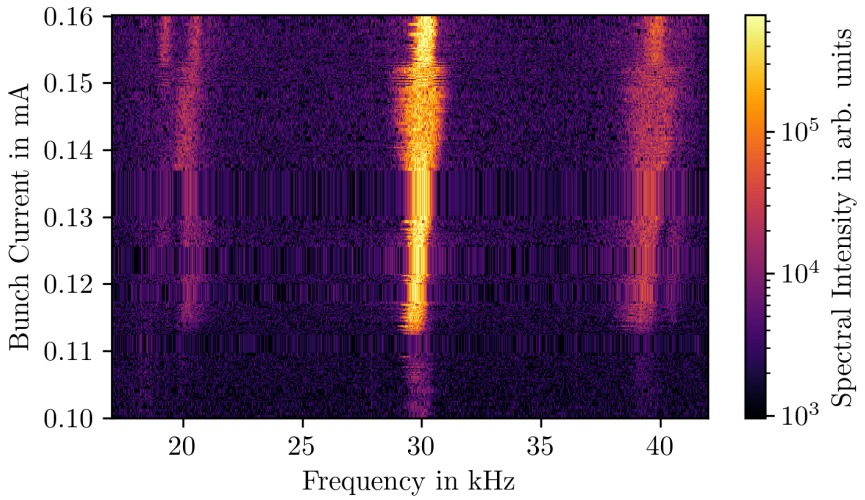

Figure 8.11: CSR intensity fluctuation spectrogram measured at negative α_c for $\alpha_c \approx -5.0 \times 10^{-4}$ and an acceleration voltage of 1000 kV. At higher currents at about 0.153 mA the structures get slimmer hinting at more complex dynamics and behaviour with increasing current.

occurring at higher currents and could be related to the change visible in the simulation in Fig. 8.10 at about 0.2 mA. Note, because of the snapdecay method, the measurements shown in Fig. 8.11 where not taken with uniformly distributed bunch currents leading to single higher "pixels", e.g. at 0.13 mA, where the measurement below was stretched up. These lines seem to contain more narrow structures than the surrounding lines, however as it is only a single measurement and to establish an effect more measurements investigating this behaviour are necessary.

The significantly lower threshold current of the instability at negative α_c visible in these spectrograms will be discussed in the following section.

Spectrograms were also measured at 1500 kV acceleration voltage to compare the dynamics at different acceleration voltages. One such spectrogram is shown in Fig. 8.12. This spectrogram shows the same characteristic features as the previous spectrograms at negative α_c with an accelerating voltage of 1000 kV in Fig. 8.8. There is again an instability threshold visible. Furthermore, these structures are again quite vertical and with little variation apart from getting broader with higher currents. The most prominent difference between the measurements at 1000 kV and 1500 kV, is the visibility of structures at higher frequencies. Also, the frequency and distance of these structures is slightly larger at 1500 kV where for 1000 kV the frequency of the main structure is at 26.8 kHz and for 1500 kV at 31.0 kHz. Furthermore, the instability threshold is lower, which will be discussed in the next section.

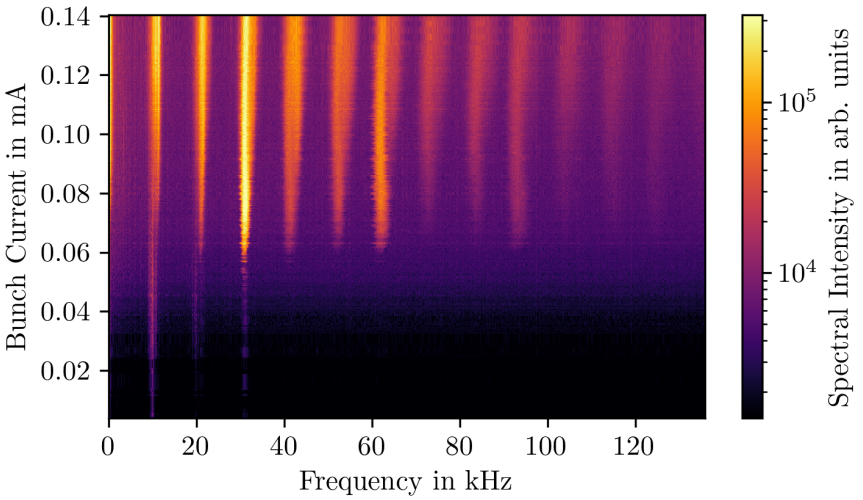

Figure 8.12: CSR intensity fluctuation spectrogram measured at negative α_c at $\alpha_c \approx -3.8 \times 10^{-4}$ and an acceleration voltage of 1500 kV. Note again, due to technical limitations the bunch current range for the negative α_c measurements is lower than for positive α_c measurements. Due to the low threshold still a range up to over twice the threshold current is visible.

The relatively small differences between the measurements at the two different voltages, compared to the differences observed between positive and negative α_c indicate that the origin of the instability dynamics is not strongly dependent on the acceleration voltage. Furthermore, the fact that the higher acceleration voltage leads to shorter bunches, does not seem to alter the driving mechanics behind the dynamics.

The measurements of the fluctuations in the emitted CSR intensity at 1.3 GeV show a significantly different behaviour for positive and negative α_c. While for positive α_c a strong complex bunch current dependence is observed in the fluctuation frequencies, at negative α_c these frequencies seem to be more constant as function of bunch current. The drastic difference between positive and negative α_c has also been confirmed with longitudinal beam dynamics simulations. This allows the conclusion that the differences mainly originate from differences of longitudinal effects due to the change of the sign of α_c. The mostly constant with beam current, and therefore predictable, behaviour of the fluctuation frequencies at negative α_c might be more easily utilised by applications sensitive to high intensity CSR.

8.4 Instability Threshold

The instability threshold is the lowest bunch current above which the instability occurs. For several negative values of α_c and accelerating voltage the instability threshold

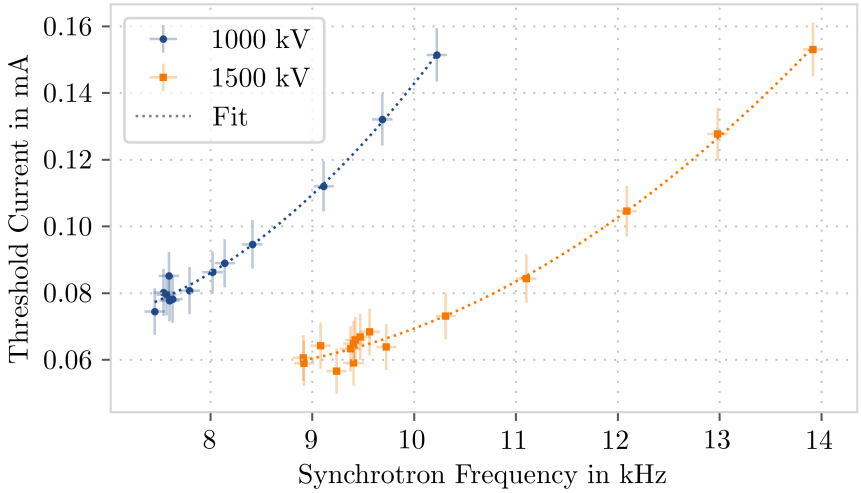

Figure 8.13: Threshold current at negative α_c as a function of synchrotron frequency for acceleration voltages of 1000 kV and 1500 kV. The threshold is higher for the lower voltage as the bunch is longer compared to the higher voltage case. Dotted lines show a second order polynomial fit.
The fit results for the fit function $I_{\mathrm{th}}(f_s) = a + b \cdot f_s + c \cdot f_s^2$ are
$a_1 = 0.254(\pm 0.103)$ $b_1 = 0.060(\pm 0.024)$ $c_1 = 0.0049(\pm 0.0013)$
$a_2 = 0.205(\pm 0.042)$ $b_2 = 0.039(\pm 0.009)$ $c_2 = 0.0025(\pm 0.0003)$
where the index 1 indicates values for 1000 kV and the index 2 for 1500 kV.

was determined. Since both parameters influence the natural bunch length as seen in Section 2.6 Eq. (2.31) it is expected that they have an influence on the threshold current which has also previously been observed at positive α_c. Figure 8.13 shows the threshold currents at negative α_c for two values of the accelerating voltage as function of synchrotron frequency. Here the synchrotron frequency serves as measurable indication of the momentum compaction factor. The synchrotron frequency is influenced by the acceleration voltage as well as the momentum compaction factor. For a fixed acceleration voltage an increase in α_c manifests as an increase in synchrotron frequency. Some spectrograms corresponding to the measurements used to determine the threshold current are shown for different values of α_c and accelerating voltages in appendix A.1.

The uncertainty on the synchrotron frequency was determined as 100 Hz effective resolution accounting also for signal-to-noise ratio of the bunch-by-bunch system [23, 14]. The current error on the threshold currents was determined as maximum error of 7-9 µA consisting of 5 µA reading error from the determination of the threshold from the spectrograms and the Poisson error of the current measurement.

The measurements for both voltages shown in Fig. 8.13 seem to follow a second order polynomial and the dotted line in Fig. 8.13 depicts a second order polynomial fit. The

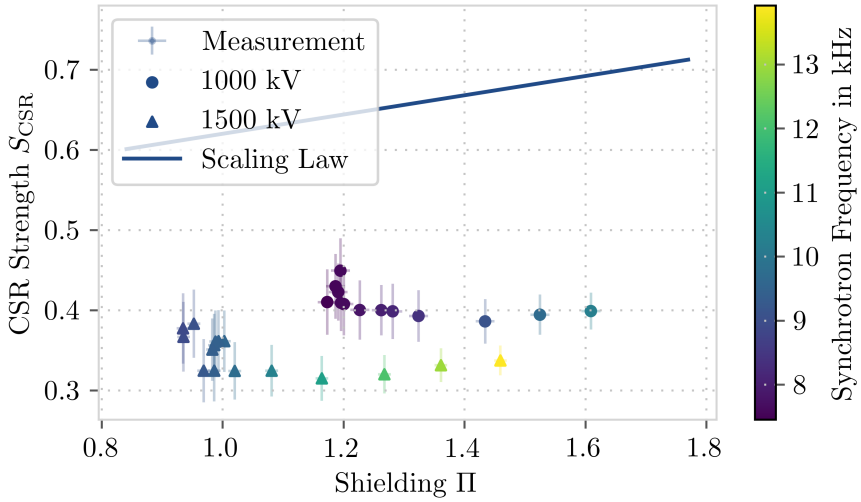

Figure 8.14: Instability thresholds at negative α_c in units of S_{CSR} as a function of Π. The solid line marks the scaling law for positive α_c as reference. The colour of measurement points indicates the synchrotron frequency for each measurement and the shape of the points indicates the voltage for each measurement. Errors shown here are the result of error propagation from the values shown in Fig. 8.13.

different coefficients in the fitted polynomials reveal a dependency on acceleration voltage of the correlation between the synchrotron frequency and instability threshold current. However, as expected, in both cases the threshold current increases with increasing bunch length indicated by an increasing synchrotron frequency (for a fixed voltage). Also, the thresholds for 1500 kV are lower compared to those for 1000 kV which is expected since the bunch length is shorter in that case, resulting in a higher charge density as well as an additional emission of CSR up to higher THz frequencies.

As previously seen in Fig. 8.7, corresponding measurements at positive α_c of the micro-bunching instability show a clear threshold as well [26, 55, 58]. In that regime a prediction for the instability threshold was derived from simulations at positive α_c in [59]. This prediction will be called “scaling law” in this thesis. Often the dimensionless parameters Shielding Π and CSR strength S_{CSR} are used, for which the threshold of the instability takes the linear form [59]

$$S_{\mathrm{CSR}} = 0.5 + 0.12\,\Pi \tag{8.1}$$

with

$$\Pi = \frac{\sigma_{\mathrm{z},0} R^{1/2}}{h^{3/2}} \tag{8.2}$$

$$S_{\mathrm{CSR}} = \frac{r_e N_\mathrm{b}}{2\pi\nu_\mathrm{s}\gamma\sigma_{\delta,0}} \cdot \frac{R^{1/3}}{\sigma_{z,0}^{4/3}} = \frac{cI_\mathrm{b}R^{1/3}}{2\pi\gamma f_\mathrm{s}\sigma_{\delta,0} I_\mathrm{A}\sigma_{\mathrm{z},0}^{4/3}}, \tag{8.3}$$

where r_e is the classical electron radius, ν_s the synchrotron tune, $\sigma_{\mathrm{z},0}$ is the natural bunch length, R is the local bending radius, h is half the height of the vacuum chamber, I_b is the bunch current, γ is the relativistic Lorentz factor, $\sigma_{\delta,0}$ is the natural energy spread and I_A is the Alfvén current[3]. The instability thresholds for the negative α_c measurements are shown in Fig. 8.14 using these dimensionless parameters.

For positive α_c it has been shown that measurements correspond quite well to the scaling law [26]. For negative α_c, however, it is easily visible from Fig. 8.14 that the threshold currents are significantly lower than the scaling law. Previous measurements of the energy spread [54] at UVSOR at negative α_c for longer bunches indicated a lower threshold as well. This was also seen in direct measurements of the instability threshold for negative α_c at MLS [60].

The measurements in Fig. 8.14 show a non-linear dependency of the threshold CSR strength on the shielding parameter in the negative α_c case. Furthermore, the threshold does not only depend on the resulting value of Π, as it is the case at positive α_c, but shows additional direct dependence on the voltage. However, measured threshold currents at both voltages behave similarly and only seem to be shifted with regard to each other. Therefore, the behaviour of the dynamics at negative α_c is significantly different to the one at positive α_c and most likely no scaling law based on Π and S_{CSR} can be found.

Complementary to the measurements the behaviour of the threshold currents as function of synchrotron frequency was simulated using Inovesa (see Section 5.7). For the determination of the thresholds in simulations a range of 100 µA around the corresponding measured thresholds was simulated and the onset of the fluctuation frequencies in the CSR emission determined. Both simulated and measured threshold currents are shown in Fig. 8.15. The simulated thresholds show a different slope than the measurements. Results in [Bro19b, Bro20b] for positive α_c show the simulated thresholds systematically above the measured thresholds with the deviations increasing for higher values of Π (and therefore bunch length). For negative α_c this effect is even bigger. In Fig. 8.15 the simulations come close to the measurements at low values of the synchrotron frequency and differ more at higher values.

[3] Alfvén current $I_\mathrm{A} = 4\pi\epsilon_0 m_e c^3/e = 17\,045\,\mathrm{A}$

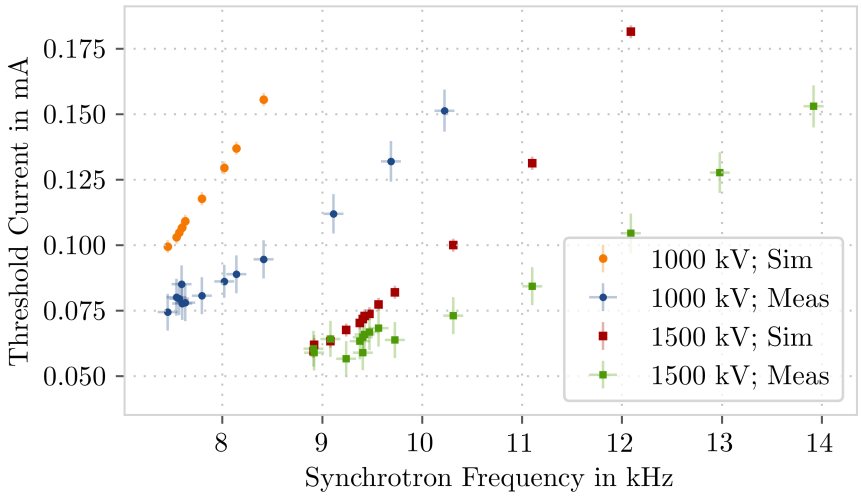

Figure 8.15: Instability thresholds as function of synchrotron frequency for 1000 kV and 1500 kV. The simulated thresholds show a different slope and differ more from the measurements at higher values of the synchrotron frequency. Note that not for all measurement points a simulation is shown.

The simulations use a pure parallel plates impedance model which might not completely describe the real machine. Also, the simulations were carried out using a purely linear α_c neglecting all higher orders. As the sextupoles were changed drastically compared to positive α_c the higher orders differ significantly as seen in Section 4.2. Both could be reasons for the mismatch between simulation and measurement and should be verified in the future.

In summary, it was shown that the instability threshold current at negative α_c is significantly lower compared to positive α_c. Additionally, the dependence on the shielding parameter Π does not follow the established scaling law valid for positive α_c and shows additional dependence on the accelerating voltage. This decrease in threshold current should be considered when aiming towards stable beam conditions at negative α_c operation.

8.5 Low Frequency Dynamics

The biggest fluctuations of CSR intensity are caused by the so-called bursts as seen in Section 8.2. These bursts occur with a characteristic repetition rate that is visible in the fluctuation spectrograms when zooming in on the lower frequency part. Studies about this low frequency for positive α_c were already published in [Bro18].

Figure 8.16 and Figure 8.17 show low frequencies in spectrograms for negative α_c and positive α_c respectively. The bright structures in both spectrograms show the dominant

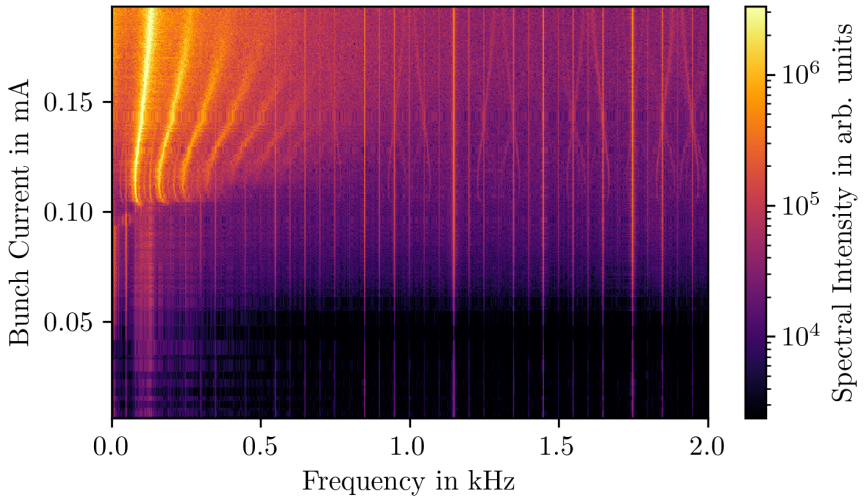

Figure 8.16: Synchrotron radiation spectrogram at a beam energy of 1.3 GeV, negative $\alpha_c \approx -3.99 \times 10^{-4}$ and an acceleration voltage of 1000 kV. This is a zoom into low frequencies of the previously shown spectrogram in Fig. 8.8.

fluctuation frequency that is associated to the repetition of the CSR intensity bursts and multiples thereof. The frequency of these structures will be called "low bursting frequency" throughout this thesis.

One of the most prominent distinctions between the spectrograms for the two signs of α_c is the location of the main structures. The low bursting frequency for negative α_c is located around about 80 Hz with a variation of about 50 Hz. In contrast to that the low bursting frequency for positive α_c is located at significantly higher frequencies around 450 Hz and with a significantly higher variation of about 300 Hz.

The low frequency fluctuations at negative α_c are visible down to 0.103 mA close to the instability threshold current at 0.089 mA. This indicates bursts of CSR intensity are present over almost the entire measured current range above the instability threshold current. However, at positive α_c the low frequency fluctuations stop significantly above (between 0.141 mA and 0.176 mA) the instability threshold at 0.115 mA, indicating the switch to another regime. In fact, the remaining fluctuations of the CSR intensity at positive α_c are almost sinusoidal in the area just above the instability threshold current without explicit bursts. They correspond to the structures seen in Fig. 8.7 and are located at higher frequencies. These two points are the main disparity between positive α_c and negative α_c when observing the low fluctuation frequency.

The course (over bunch current) of the low frequency fluctuations follows a certain pattern with increasing current. At low currents for negative α_c, just above the threshold current, the dominant fluctuation frequency slightly decreases at first. Towards higher

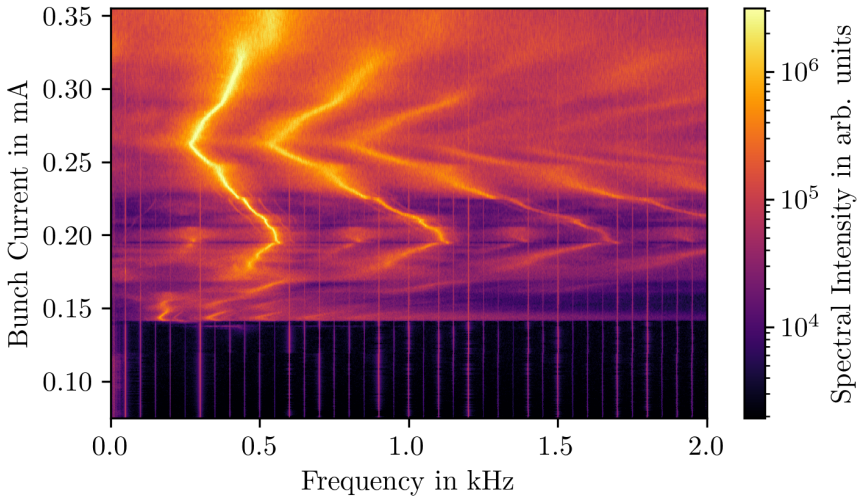

Figure 8.17: Synchrotron radiation spectrogram at a beam energy of 1.3 GeV, positive $\alpha_c \approx 3.90 \times 10^{-4}$ and an acceleration voltage of 1000 kV. This is a zoom into low frequencies of the previously shown spectrogram in Fig. 8.7.

currents the dominant fluctuation frequency increases again, in the example in Fig. 8.16 from approximately 0.11 mA upwards. The main trend is therefore an increase in fluctuation frequency with current. There are also no further changes in direction of the fluctuation frequency change visible. For positive alpha in Fig. 8.17 the dominant fluctuation frequency exhibits a much more complex behaviour. Multiple kinks and changes in the movement direction of the fluctuation frequency with increasing current are visible.

A much lower repetition rate of the CSR bursts was observed at negative α_c compared to positive α_c. Furthermore, the behaviour of the bursts of CSR intensity at negative α_c was seen to be fairly constant in bunch current compared to positive α_c and is therefore much more predictable. This is similar to what was seen for the fluctuations in CSR intensity at higher frequencies in Section 8.3. Again, this could simplify the utilisation of the high intensity CSR during the instability by exploiting the slow predictable time structure.

8.6 Energy-Dependent Behaviour

The energy of electrons plays an important role in the longitudinal dynamics of a bunch. For example is the incoherently radiated power, see Eq. (2.18), depending on the fourth power of the energy. With the radiation power also the damping time, see Eq. (2.27), changes for different energies. The bursts in the CSR emission originate from

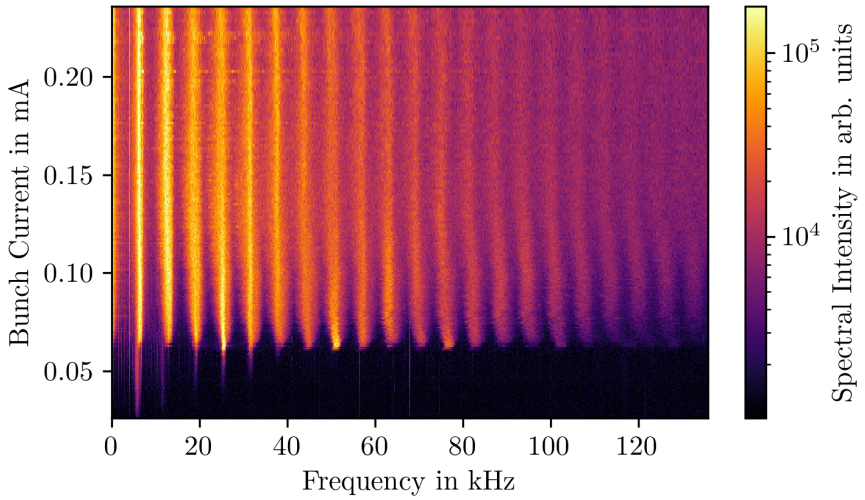

Figure 8.18: CSR intensity fluctuation spectrogram measured at negative α_c for 0.9 GeV at an accelerating voltage of 300 kV and $\alpha_c \approx -4.5 \times 10^{-4}$.

substructures in the longitudinal phase space which are smeared out and damped down through radiation damping. Therefore, the behaviour of the instability is expected to depend on the energy of the electrons.

This section will investigate the changes to the dynamics of the instability between the three energies of 1.3 GeV, 0.9 GeV and 0.5 GeV. At first the current-dependent dynamics as well as the repetition rate of bursts is compared for the two higher energies 1.3 GeV and 0.9 GeV. Subsequently, measurements at these energies will be compared to measurements at injection energy of 0.5 GeV in terms of current-dependent dynamics and repetition rate as well.

Figure 8.18 shows a spectrogram measured at negative α_c and 0.9 GeV for conditions with a corrected orbit down to below 3 mm maximum orbit deviation. A similarity to the spectrograms measured at 1.3 GeV, shown in Fig. 8.8, is clearly visible. One obvious difference is the frequency and harmonics of the main structures visible in the spectrograms. These originate from the rotation of substructures in the longitudinal phase space, as described in Section 8.1. Therefore, the position and distance of these structures depends on the synchrotron frequency as the main contribution to the rotation frequency of the charge distribution in the longitudinal phase space. Since the accelerating voltage for the measurement in Fig. 8.18 is comparably low at 300 kV (compared to e.g. 1000 kV for the measurement at 1.3 GeV, Fig. 8.8), the synchrotron frequency is also comparably low with $f_s \approx 5.7$ kHz ($f_s \approx 8.1$ kHz in Fig. 8.8). The structures start at lower frequencies and are closer together with a distance of ≈ 6.3 kHz compared to the structures visible in the measurement at 1.3 GeV with a distance of ≈ 8.8 kHz. Apart

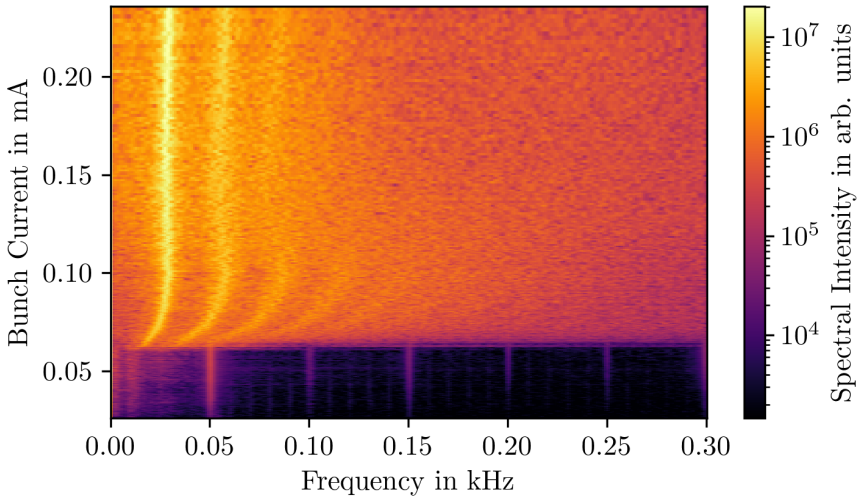

Figure 8.19: CSR intensity fluctuation spectrogram measured at negative α_c for 0.9 GeV at an accelerating voltage of 300 kV and $\alpha_c \approx -4.5 \times 10^{-4}$. This is a zoom into low frequencies of the same data shown in Fig. 8.18.

from this difference there is no further significant difference visible in the displayed data. This hints at no significant effect of the energy between 1.3 GeV and 0.9 GeV affecting the major structures in the spectrograms.

However, as the energy clearly changes the damping time ($\tau_d \propto {}^{U_0}/_{E} \propto E^3$, see Section 2.6) and the damping time influences the washing out and damping of the substructures in the charge density in the longitudinal phase space, it is expected that the repetition rate of the bursts is affected by the damping time. Figure 8.19 shows the low frequency structures of Fig. 8.18 as zoom into the lower frequencies. The main structure represents the repetition rate of the bursts as described in Section 8.5 which is for this measurement at about 25 Hz. In Section 8.5 it was found that the measurements at 1.3 GeV resulted in a repetition rate of roughly 80 Hz or about three times the frequency seen for the measurements here at 0.9 GeV. Estimating the ratio of the damping times between the two energies as ${}^{(1.3\,\mathrm{GeV})^3}/_{(0.9\,\mathrm{GeV})^3} \approx 3$ leads to the conclusion that the repetition rate of bursts roughly scales with the inverse damping time.

At positive α_c these observations are not as easy, as the burst repetition rate here shows a strong dependency on the bunch current. Measurements at positive α_c and 0.9 GeV were performed and the resulting spectrogram is shown in Fig. 8.20. A zoom into low frequencies is shown in Fig. 8.21. While no singular frequency can be given for the burst repetition rate due to the current dependency, when considering the extremes (min/max) of the repetition rate it roughly scales with the inverse damping time as well.

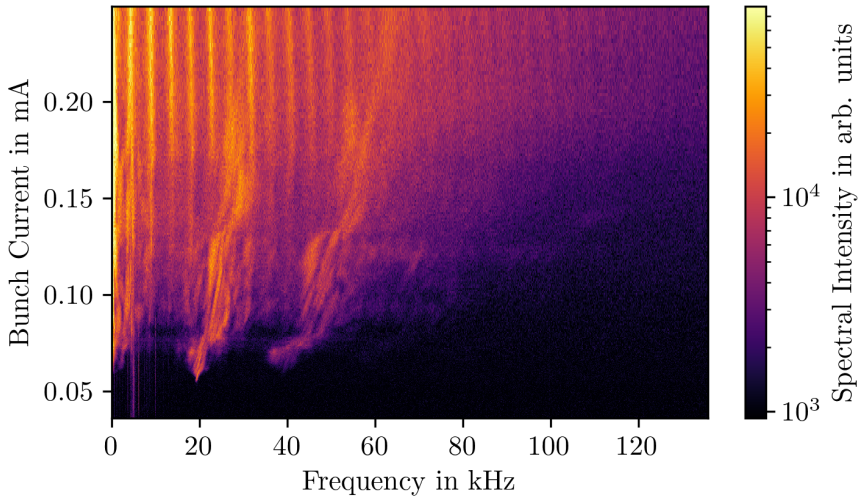

Figure 8.20: CSR intensity fluctuation spectrogram measured at positive α_c for 0.9 GeV at an accelerating voltage of 300 kV and $\alpha_c \approx 3.6 \times 10^{-4}$.

With regard to positive α_c these results have already jointly been published in [Bro21b]. The maximum frequency for 1.3 GeV seen in Fig. 8.17 is roughly 600 Hz and here at 0.9 GeV in Fig. 8.21 the maximum is roughly 200 Hz, exhibiting the same factor of 3 as previously seen at negative α_c. As the same factor of 3 has been found for positive and negative α_c it shows a similar scaling of the burst repetition rate with beam energy.

Concerning the structures at higher frequencies, the spectrograms for positive α_c show similar complex structures at 1.3 GeV (Fig. 8.7) and 0.9 GeV (Fig. 8.20). Additionally, vertical structures, comparable to the structures seen at negative α_c are visible, down to roughly two times the threshold current. The structures themselves are not necessarily caused by the reduced energy, since they are also seen for high enough currents in some positive α_c measurements at 1.3 GeV. Spectrograms to visualise this are shown in appendix A.2. The fact, however, that these vertical structures reach into the lower current regions of the spectrogram could be caused by the reduced energy, as such a behaviour seems unique to the measurements at the lower energy.

Such measurements were also conducted at the injection energy of 0.5 GeV. Figure 8.22 shows a measurement at 0.5 GeV for a positive α_c of $\alpha_c \approx 1.5 \times 10^{-3}$. The dominant structures visible are far less complex than what was seen for positive α_c measurements at higher energies, such as 0.9 GeV in Fig. 8.20 and 1.3 GeV in Fig. 8.7. The structures show similarities to those of measurements at negative α_c and 1.3 GeV. However, the visible structures are washed out and relatively low in intensity compared to the background. In Fig. 8.23 a spectrogram for a measurement at negative α_c and 0.5 GeV is shown for the same absolute value of $|\alpha_c| \approx 1.5 \times 10^{-3}$. Similar to the positive α_c measurement the

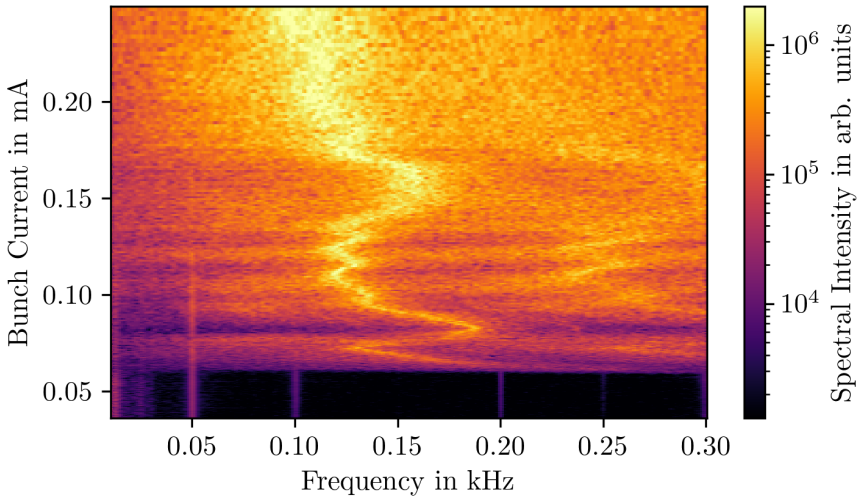

Figure 8.21: CSR intensity fluctuation spectrogram measured at positive α_c for 0.9 GeV at an accelerating voltage of 300 kV and $\alpha_c \approx 3.6 \times 10^{-4}$. This shows a zoom into low frequencies of Fig. 8.20.

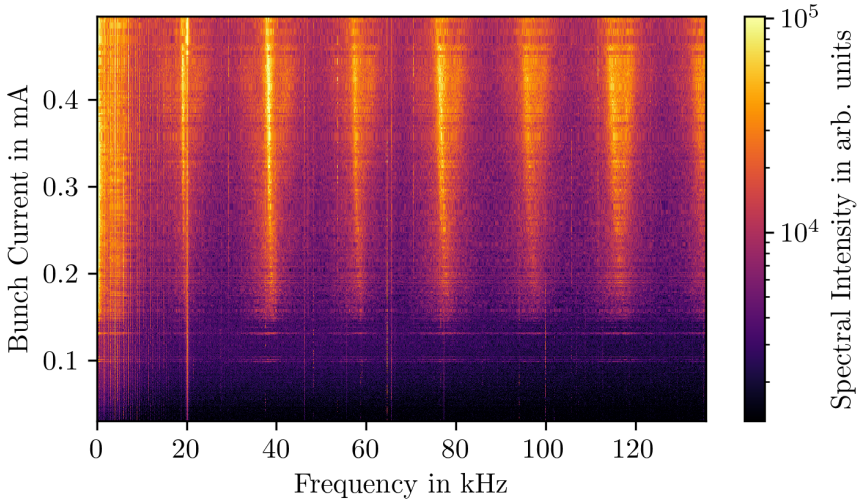

Figure 8.22: CSR intensity fluctuation spectrogram measured at positive α_c for 0.5 GeV at an accelerating voltage of 600 kV and $\alpha_c \approx 1.5 \times 10^{-3}$.

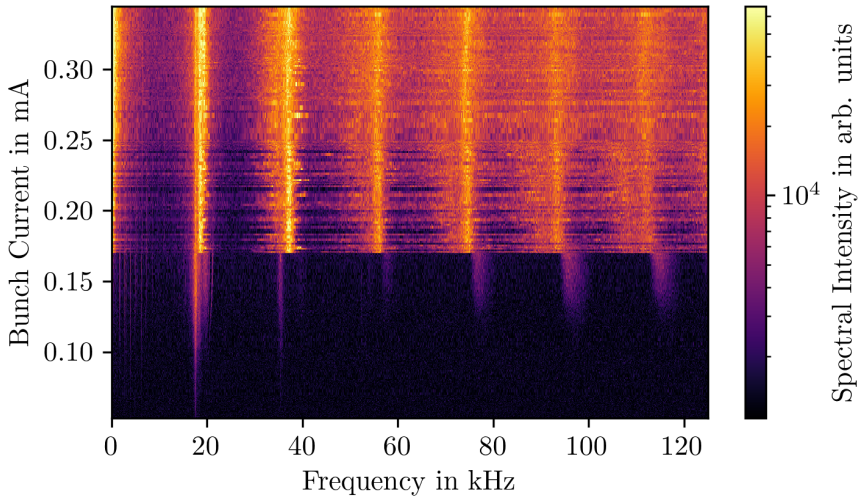

Figure 8.23: CSR intensity fluctuation spectrogram measured at negative α_c for 0.5 GeV at an accelerating voltage of 600 kV and $\alpha_c \approx -1.5 \times 10^{-3}$.

visible structures are washed out and low in intensity compared to the background. At this energy the behaviour of the longitudinal instability seems to differ only little between the two signs of α_c, at least for currents above a certain threshold. Below this threshold the negative α_c measurement abruptly changes behaviour while the behaviour at positive α_c slowly weakens. Such an abrupt change as seen in the negative α_c measurement is also a great difference to the measurements at higher energies. It seems that the instability for both signs of α_c behaves significantly different at 0.5 GeV than it does for 0.9 GeV and 1.3 GeV. This suggests, either that an additional effect manifests stronger at higher energies or that an effect significant at low energies diminishes in significance at higher energies.

The drastic change from 0.9 GeV and 1.3 GeV to 0.5 GeV in the behaviour of the instability for both signs of α_c could be caused by the extremely large damping time at 0.5 GeV of about $\tau_d \approx 182$ ms. This is expected to influence how the structures in phase space form and wash out and could therefore significantly alter the resulting behaviour of the instability. Effects of the damping time on the instability behaviour were previously observed in simulations [61]. Another possible reason for the big difference in the observed behaviour of the instability in the measurements at 0.5 GeV, is the relatively high value of α_c. However, it was not observed that similar changes in α_c at 1.3 GeV had such a strong influence on the observed behaviour. Furthermore, for the measurements at 0.5 GeV and negative α_c the orbit shows quite large deviations from the reference orbit (see also Section 3.3) which is not the case at higher energies. This might have an influence on the observed behaviour of the instability. On the other hand,

for positive α_c the orbit is small at all three energies and still a big difference is visible. The resulting effect is most likely caused from a combination of these effects where the drastic change in damping time is expected to be the most dominant.

To estimate the low frequency structure position the damping time increase from 0.9 GeV to 0.5 GeV might be used. This would result in a factor of ${}^{(0.9\,\mathrm{GeV})^3}/_{(0.5\,\mathrm{GeV})^3} \approx 5.8$. Following the same almost linear scaling of the low frequency that was observed between 1.3 GeV and 0.5 GeV for negative α_c, a low frequency of a few Hz would be expected: $25\,\mathrm{Hz}|_{0.9\,\mathrm{GeV}}/5.8 \approx 4.3\,\mathrm{Hz}|_{0.5\,\mathrm{GeV}}$. This is close to the frequency resolution of the measurements, as the measurement duration was 1 s per current resulting in a resolution of ≥ 1 Hz. The previous measurements all showed a certain spread in frequency of the low frequency structures of at least a few Hz. Therefore, the low frequency structures are not clearly visible. By calculating the mean of the Fourier transform of several 1 s measurements[4] a weak structure can be made visible at negative α_c which is shown in Fig. 8.24a. A peak in this plot is visible at about 2 Hz which is in the same order of magnitude as the expected 4.3 Hz, especially when considering the frequency resolution of these measurements. At positive α_c the mean low frequency structures for 0.9 GeV could be placed at about 120 Hz (with a variation of about ± 50 Hz) which would put the low frequency structure for 0.5 GeV by scaling with a factor of 5.8 at a frequency of about 20 Hz. In Fig. 8.24b also the mean of the Fourier transformed signal for a few measurements is shown. A peak at about 5 Hz is visible. This is lower than the expected 20 Hz, however, it is in the same order of magnitude. Two facts are important to note here, first, the measurements for 0.9 GeV show a large frequency span over current (about $\pm 40\,\%$). And second, the data for 0.5 GeV only represents a small current range. These, coupled with the limited frequency resolution indicates that the seen 5 Hz is roughly compatible to the expected frequency range. Therefore, when considering both signs of α_c, even though the higher frequency structures differ significantly between the previous observations and the measurements at 0.5 GeV, the repetition rate of the burst like intensity fluctuations seem to follow a similar scaling with damping time.

The measurements at the three presented energies allowed the observation that at both signs of α_c the higher frequency structures in the behaviour of the instability only differ slightly between the higher energies of 1.3 Gev and 0.9 GeV. A significant change to these structures was observed between the higher energies (1.3 GeV and 0.9 GeV) and the injection energy of 0.5 GeV. The slow repetition rate of the burst like intensity variations, on the other hand, could be shown to follow the same scaling with the longitudinal

[4] This means a mean of several horizontal lines in the spectrogram (here 5 lines were used).

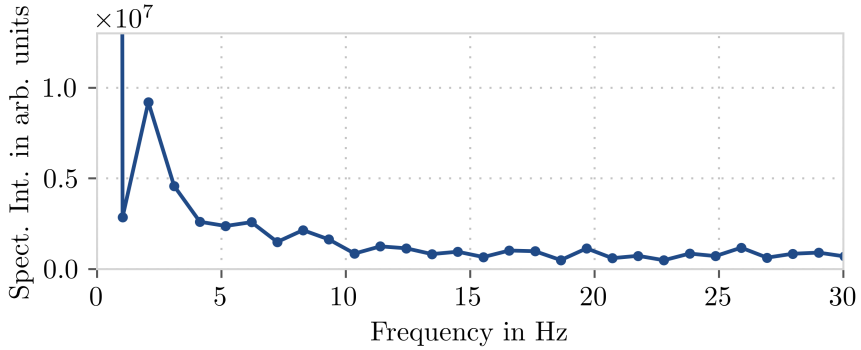

(a) negative α_c

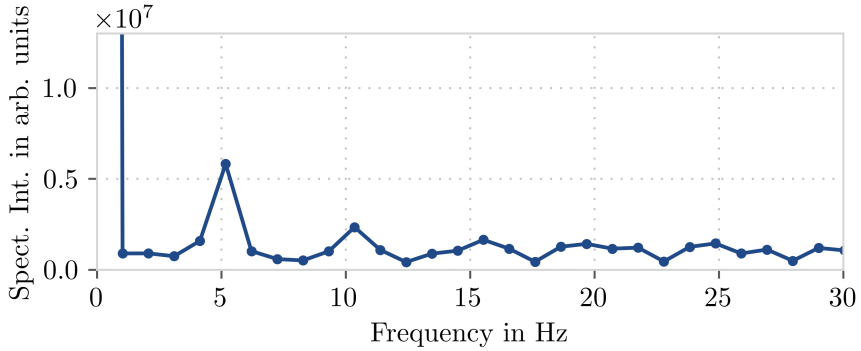

(b) positive α_c

Figure 8.24: Fourier transformed signals measured at positive and negative α_c. The mean value over a small current range was calculated to reduce the background noise fluctuations.

damping time for all three observed energies from 1.3 GeV down to 0.5 GeV. This scaling can be used for both signs of α_c to estimate the burst repetition rate from a given repetition rate to the rate at a different energy. Furthermore, the repetition rate at negative α_c can be roughly estimated from the damping time as $f_{rep} \approx \frac{1}{\tau_d}$.

8.7 Arrival Time of CSR Pulses at Negative α_c

Observations of the arrival time of detector signals could allow additional insights into the dynamics from a different perspective than the pure observation of the amplitude fluctuations. This can be done by using an oscilloscope to digitise the detector pulse shape[5]. Such measurements were conducted for positive and negative α_c to extract the

[5]The arrival time could also be extracted from measurements with KAPTURE when using a fast signal splitter. However, as the arrival time variation amplitudes were not known and the four sampling points of KAPTURE would limit the resolution, the approach with an oscilloscope was chosen. In the future this would be possible using KAPTURE-2 and 8 channels as well. Another possibility was used at the Diamond Light Source [62] which employed a streak camera with special reflective optics.

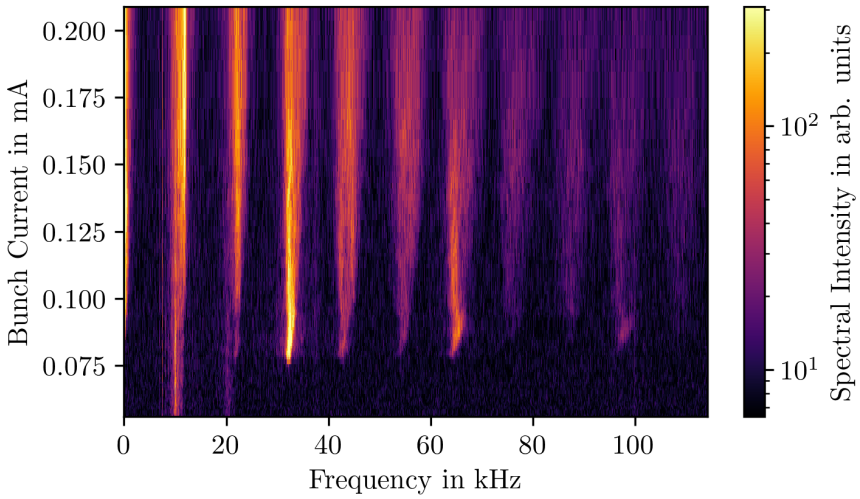

Figure 8.25: Intensity fluctuation spectrogram measured using an oscilloscope at 1.3 GeV and $\alpha_c \approx -4 \times 10^{-4}$ with an acceleration voltage of 1400 kV. Due to the use of segments in the oscilloscope the intensity fluctuations should be almost free of errors due to arrival time fluctuations.

pulse amplitude as well as the arrival time of the detector signal. Compared to the previously used method (using KAPTURE in single channel configuration), the method using the oscilloscope shows strong limitations in the temporal repetition rate of the measurements as well as the measurement duration, originating from the limited memory depth. This leads to a limited resolution of the Fourier transformed fluctuations as well as the current resolution of resulting fluctuation spectrograms. To circumvent these limitations at least for the amplitude measurements, in parallel to the oscilloscope (arrival time and amplitude) KAPTURE was used to measure the amplitude. An additional benefit of this approach is the possibility to verify that the previously shown KAPTURE measurements are not significantly influenced by arrival time fluctuations.

The measurement technique is described in Section 5.6. Measurements were performed using the segmented mode of an 4 GHz oscilloscope. This allowed to record the detector response with 20 GS per second. The detector system consists of the actual detector and an internal amplifier. As the amplifier has a video bandwidth of 4 GHz the pulse is effectively passed through a low-pass filter that affects the shape of the pulse. This should, however, not affect the recorded relative arrival time of the detector pulses. Post-processing the data by interpolating the data points via the Whittaker-Shannon interpolation scheme [44] allowed to reconstruct the actual peak value and arrival time of the peak.

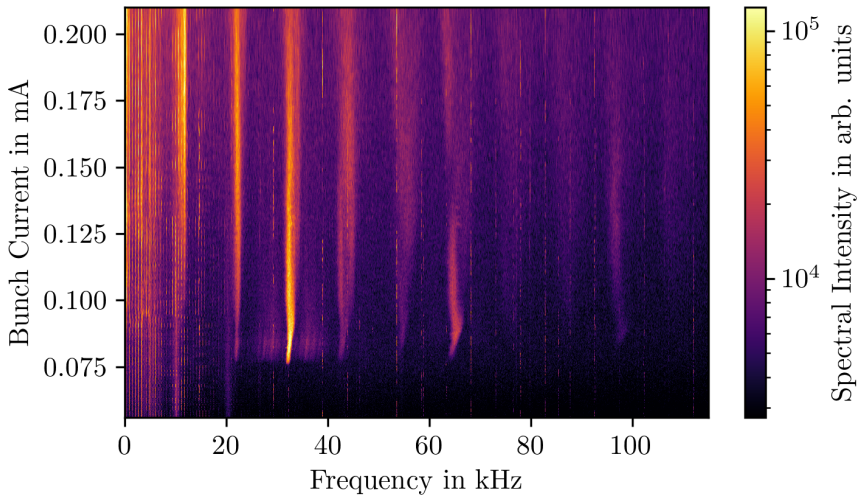

Figure 8.26: Intensity fluctuation spectrogram measured using KAPTURE at 1.3 GeV and $\alpha_c \approx -4 \times 10^{-4}$ with an acceleration voltage of 1400 kV.

Analogously to the measurements using KAPTURE an intensity fluctuation spectrogram can be calculated using the peak height extracted from the oscilloscope measurements. Such a spectrogram is shown in Fig. 8.25. By using a signal splitter the oscilloscope and KAPTURE were connected in parallel and both devices sampled the same signal in parallel. The spectrogram acquired with the oscilloscope is almost identical to the spectrogram acquired with KAPTURE, shown in Fig. 8.26. This is direct validation for the assumption that the 4 GHz detector system combined with KAPTURE is not significantly affected by arrival time fluctuations due to the relatively broad peak of the detector response compared to the small arrival time fluctuations. The spectrogram acquired with an oscilloscope seems to have less spectral intensity between the dominant structures. This might be a remnant from the influence of arrival time on digitised signal height for the measurements with KAPTURE, especially in regions towards lower frequencies. Additionally, the frequency resolution is higher for the KAPTURE measurements, potentially making it more susceptible to background. For the important areas defining the main structures in the spectrograms as well as the instability threshold, however, these additional fluctuations are clearly identified as background and do not hinder the evaluation. As a result, this means the previously shown KAPTURE measurements are not significantly affected by arrival time fluctuations and can be interpreted as amplitude fluctuations. Therefore, the effects seen in previous sections are indeed based on amplitude fluctuations as assumed. The comparably long time for saving data required by the oscilloscope restricts the number of measurements per time interval to a significantly lower value (about $\frac{1}{10}$) than what is possible with

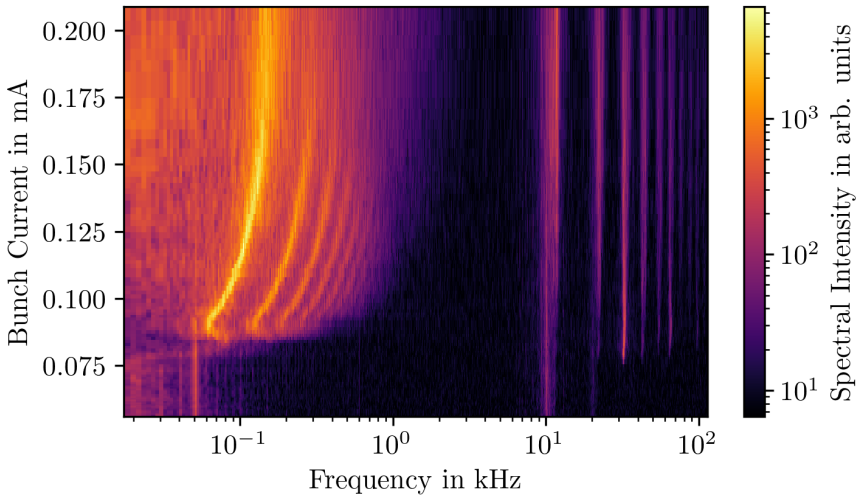

Figure 8.27: Intensity fluctuation spectrogram measured using an oscilloscope at 1.3 GeV and $\alpha_c \approx -4 \times 10^{-4}$ with an acceleration voltage of 1400 kV. Due to the use of segments in the oscilloscope the intensity fluctuations should be almost free of errors due to arrival time fluctuations. This uses a logarithmic scale for the frequency axis to show the low frequency structures.

KAPTURE [6]. Therefore, the bunch current resolution of these measurements is quite coarse compared to the KAPTURE measurements (compare e.g. Fig. 8.25 and Fig. 8.26).

To visualise the low frequency structures Fig. 8.27 shows the data from Fig. 8.25 with a logarithmic scale for the frequency axis. The structures are nearly identical to the structures acquired with KAPTURE, shown in Fig. 8.28 which shows the data from Fig. 8.26 with a logarithmic frequency scale. Therefore, even though at lower frequencies the noise in the KAPTURE measurements is higher compared to the oscilloscope measurements, the important structures are again clearly visible.

From the oscilloscope data the arrival time of the detector pulse can be extracted and a spectrogram from this data can be calculated. In Fig. 8.29 such a spectrogram is shown. The distinct features seen in the intensity fluctuation spectrograms are not visible here. This is not unexpected as the main structures in an intensity fluctuation spectrogram are caused by the rotation of the substructures on the charge density in the longitudinal phase space which changes the longitudinal bunch profile. This should not significantly affect the measured arrival time as the detector used is not fast enough to resolve the bunch profile. The strong vertical line at about 75 kHz is not associated with a known frequency originating from bunch arrival time oscillations and is probably

[6] For recordings of 2^17 segments (equivalent to 0.57 s for one segment every 12. turn), the measurements can be repeated approximately every 40 seconds. For KAPTURE, for example for recording every 10. turn for a duration of 1 second, the measurement can be repeated every 3 seconds.

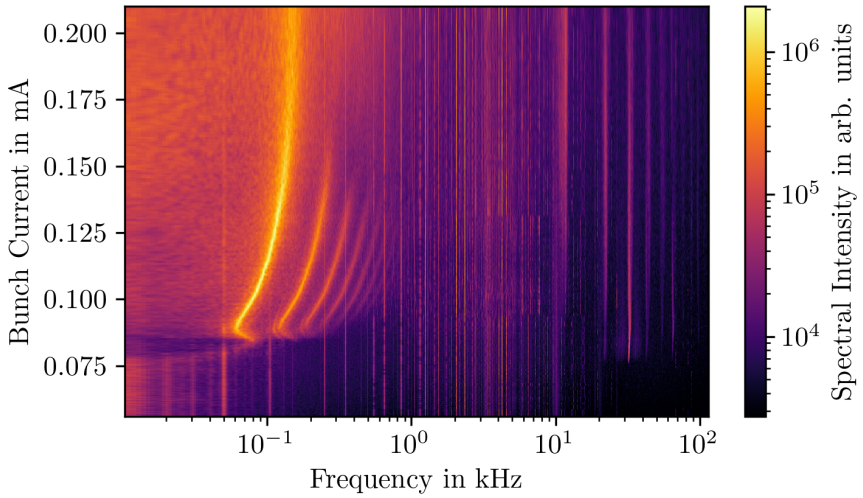

Figure 8.28: Intensity fluctuation spectrogram measured using KAPTURE at 1.3 GeV and $\alpha_c \approx -4 \times 10^{-4}$ with an acceleration voltage of 1400 kV. This uses a logarithmic scale for the frequency axis to show the low frequency structures.

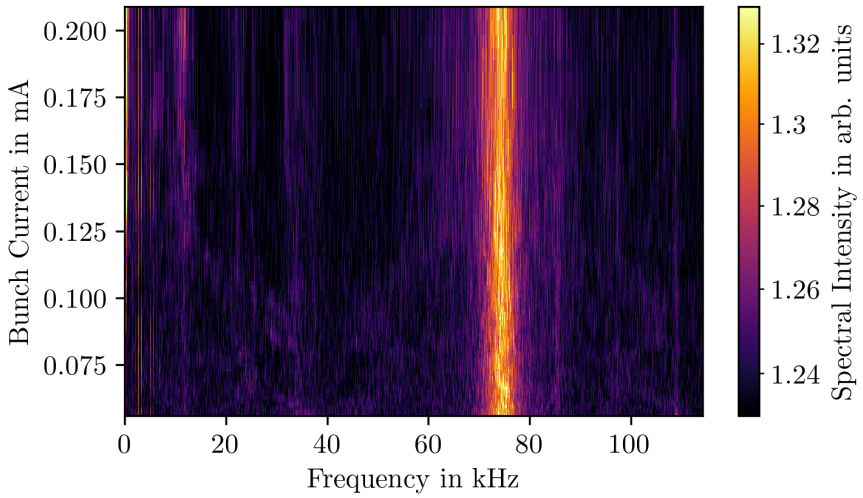

Figure 8.29: Arrival time fluctuation spectrogram measured using an oscilloscope at 1.3 GeV and $\alpha_c \approx -4 \times 10^{-4}$ with an acceleration voltage of 1400 kV.

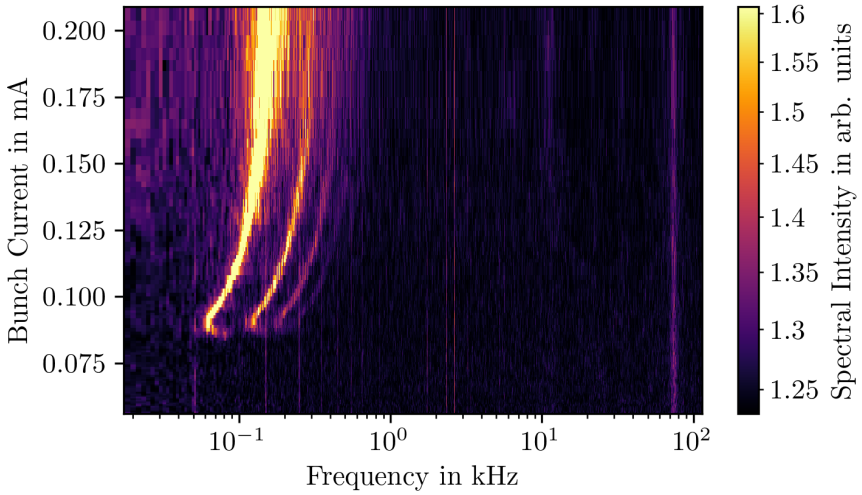

Figure 8.30: Arrival time fluctuation spectrogram measured using an oscilloscope at 1.3 GeV and $\alpha_c \approx -4 \times 10^{-4}$ with an acceleration voltage of 1400 kV. This uses a logarithmic scale for the frequency axis to show the low frequency structures.

caused by jitter in the timing signals that are used to synchronise the oscilloscope to the electron bunches.

A plot of the arrival time spectrogram measured with the oscilloscope using a logarithmic scale on the frequency axis, however, reveals some arrival time fluctuations, as shown in Fig. 8.30. These are the same structures as the ones visible on the intensity fluctuation spectrogram acquired with the oscilloscope (Fig. 8.27) as well as on the spectrogram acquired with KAPTURE (Fig. 8.28). The fact that it is visible on both types of spectrograms shows a correlation between the arrival time fluctuations and the intensity fluctuations. In fact, these fluctuations are correlated with the repetition rate of the CSR bursts as described in Section 8.5 which lead to an additional temporal energy loss and thus to changes in the RF phase and therefore to arrival time fluctuations.

Particles that lose additional energy have a longer path length per revolution for negative α_c according to the momentum compaction factor Eq. (2.12). Due to the almost constant speed of the particles at about the speed of light these particles arrive at later times compared to the particles that do not lose additional energy. The later arrival time in the cavities leads to an increased energy gain which compensates the additional energy loss. Caused by this shift relative to the RF phase synchrotron oscillations could be excited around this new phase. These synchrotron oscillations would be subsequently damped down to normal levels through radiation damping (c.f. Section 2.6). As from the measurements no significant increase of the arrival time fluctuations with the synchrotron

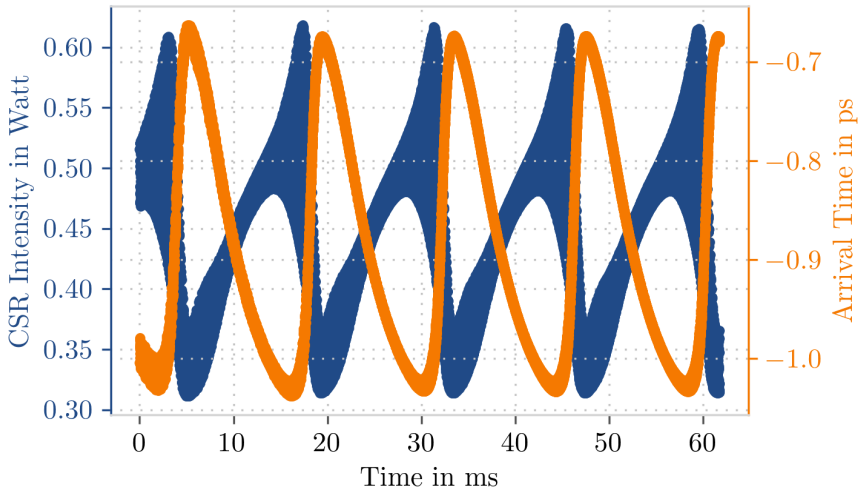

Figure 8.31: Bunch position and CSR intensity as function of time from Inovesa simulations at negative α_c. A clear inverse correlation between both quantities is visible. This data is for the same values as Fig. 8.10, an accelerating voltage of 1000 kV, $\alpha_c = -3.95 \times 10^{-4}$ and an energy of 1.3 GeV with a bunch current of 0.16 mA.

frequency is visible, it seems this process is an over damped oscillation. Therefore, for the measurements dominantly the repetition rate of bursts and its multiples are visible from the arrival time fluctuation spectrograms such as Fig. 8.27.

The connection between the CSR outbursts and arrival time variances can also be very nicely visualised by using simulated data. Figure 8.31 shows the arrival time and CSR intensity as function of time for the same simulation data shown in Section 8.3 (Fig. 8.10). An inverse correlation is clearly visible from this data. Particles loosing energy due to additional emission during a burst, arrive later[7] in the cavities due to the longer path length caused by a negative sign of α_c. Therefore, the observed inverse correlation between CSR intensity and arrival time is expected. Figure 8.32 shows the equivalent case for positive α_c. Here the situation is reversed. Due to the positive sign of α_c particles loosing additional energy will arrive earlier at a reference position. Therefore, there is a positive correlation between arrival time and CSR intensity, which can be clearly seen from Fig. 8.32. The amplitude of the arrival time oscillations seen in the simulations is very small and would probably not be resolvable with the used measurement method. However, as the simulation uses a simplified model and assumes an isomagnetic ring, unconsidered additional CSR emission, e.g. due to edge radiation at the edges of bending magnets, would lead to an increased arrival time fluctuation amplitude. Additionally, due to dispersion at the beamline an energy offset would result

[7] For Inovesa simulations lower arrival time values correspond to a later arrival.

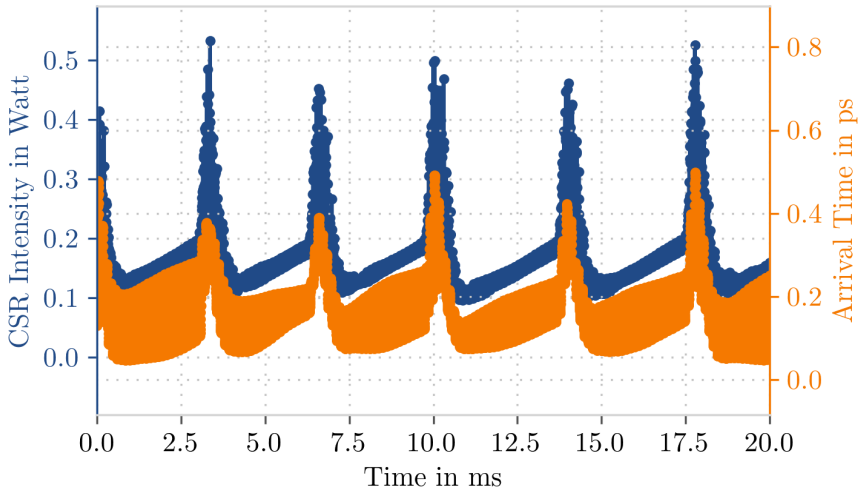

Figure 8.32: Bunch position and CSR intensity as function of time from Inovesa simulations at positive α_c. A clear inverse correlation between both quantities is visible. This data is for the same values as Fig. 8.10, an accelerating voltage of 1000 kV, $\alpha_c = 3.95 \times 10^{-4}$ and an energy of 1.3 GeV with a bunch current of 0.32 mA.

in a horizontal position offset that could lead to a longer path for the emitted radiation from emission point to detector and could increase the measured arrival time offset of the THz pulse. Furthermore, previous measurements using electro optical spectral decoding (EOSD) [63] at positive α_c showed an arrival time fluctuation amplitude in the order of at least a quarter of the bunch length [Bro19a]. This is substantially higher than what is seen in these simulations, where the bunch length (temporal mean) for positive $\alpha_c$is $\sigma_z \approx 3.7$ ps and for negative α_c is $\sigma_z \approx 5.1$ ps. All these indications hint at additional effects not considered in the simulation which increase the arrival time fluctuation amplitude. It is therefore concluded that the basic principle is simulated correctly, but the amplitude of the oscillations is underestimated in the simulations.

From the observations in this section it is clear that the arrival time of the CSR pulses fluctuate in correlation to the emission intensity of the CSR. Therefore, the emitted radiation especially during bursts has a great impact on the longitudinal dynamics as the changes to the position and phase of the bunch are well visible.

8.8 Intensity of emitted CSR

While the previous sections focussed on the fluctuation of the CSR intensity, it can also be of interest to consider the amplitude of the emitted radiation intensity. The detectors used for CSR intensity detection are not calibrated. It is therefore hard to estimate the

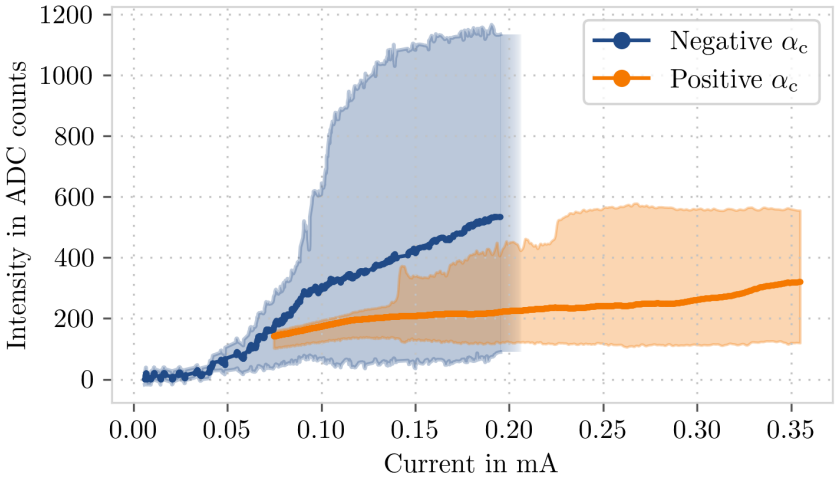

Figure 8.33: Detected radiation intensities for positive and negative α_c with a value of $|\alpha| \approx 4 \times 10^{-4}$ at 1000 kV accelerating voltage. The solid lines indicate the mean values for each current. The top of the shaded areas marks the maximum intensity per current and the bottom of the shaded areas marks the minimum per current. The data shown here is the same as used in figures 8.7 and 8.8.

absolute value of the intensity. However, as the same detector and acquisition system[8] was used for both positive and negative α_c measurements the digitised detector signals can be compared in amplitude. Such a comparison can be done in multiple ways. One way would be to compare the detector signal amplitude for positive and negative α_c for measurements at the same bunch current. For this comparison the signal does not have to be scaled with bunch current. However, as the thresholds at positive and negative α_c differ significantly the same bunch current does not typically result in the same instability behaviour. This has to be kept in mind when comparing these measurements.

Comparisons of the intensity between measurements at different parameters but the same sign of α_c should be performed for currents in comparable instability regimes[9]. Ideally this should also be considered for comparisons between the two signs of α_c. However, the instabilities differ quite drastically, as seen in Section 8.3, and it is hard to define equivalent regimes for the instability at positive and negative α_c. Therefore, the intensity as function of the whole bunch current range is considered here. Figure 8.33 shows the intensity for each measurement as function of bunch current for positive and negative α_c. The shaded area is bounded by the peak and minimum intensity per current. The peak intensity increases fast at the respective instability threshold for both signs.

[8] In fact, the same setup consisting of detector, cables, amplifiers, DAQ system, etc was used.
[9] Instability regimes for positive α_c at KARA were previously discussed in [64]

This is expected as the instability leads to an increased emission of CSR. At positive α_c this fast increase is more pronounced as expected from the spectrograms. On the other hand, it is clearly visible that the mean and peak value for negative α_c is significantly above the values for positive α_c over the total bunch current range above 0.08 mA[10]. At higher currents the signal is up to a factor of 2 higher for negative α_c than positive α_c. The minimum, however, is lower for negative α_c than the minimum for positive α_c. The observed higher mean intensity at negative α_c is connected to the observed lower bunch length seen in Chapter 7. This results in higher frequency components in the form factor of the bunch and therefore results in higher coherent synchrotron radiation intensity in the corresponding frequencies.

For both signs of α_c the detected radiation intensity fluctuates also below the instability threshold (0.089 mA for negative α_c and 0.115 mA for positive α_c), even though the fluctuations are smaller. Below the threshold current the mean values are closer to the peak values indicating the lower intensity is only radiated during a fraction of the time. Above the threshold current, however, the mean radiation intensity seems to show a kink and increases slower. The peak intensity above the threshold current is in both cases rising faster than the mean value, while the minimum stays more or less constant with current. This shows that the instability leads to increased radiation but also to increased fluctuation. Extrapolating the mean value from below the threshold current to values above, assuming no instability would occur, would therefore result in higher mean values than those actually present. This implies the instability increases the peak intensity but decreases the mean intensity compared to the theoretical intensity at the same bunch current without instability, at least in the frequency range measured here. A reduced mean intensity is expected, as during the instability the bunch length varies over time increasing the mean bunch length (Chapter 7). The effect is more pronounced in the measurement for negative α_c. It is also visible, albeit significantly weaker, in the simulations shown in Fig. 8.34.

Similar to the measurements the power in simulations for negative α_c is significantly higher compared to positive α_c. The simulations show a kink at the instability threshold as well. For the power determination from the simulations the entire simulated frequency range (0 Hz $-$ $\sim$ 2.9 THz) is considered, meaning the frequency responsivity of the detector is not considered. Nevertheless, the beamline cut-off for the radiation transport pipe present at the port where the measurements were taken is considered.

[10] Measurements at the Diamond Light Source indicated a higher CSR intensity at negative α_c as well [65].

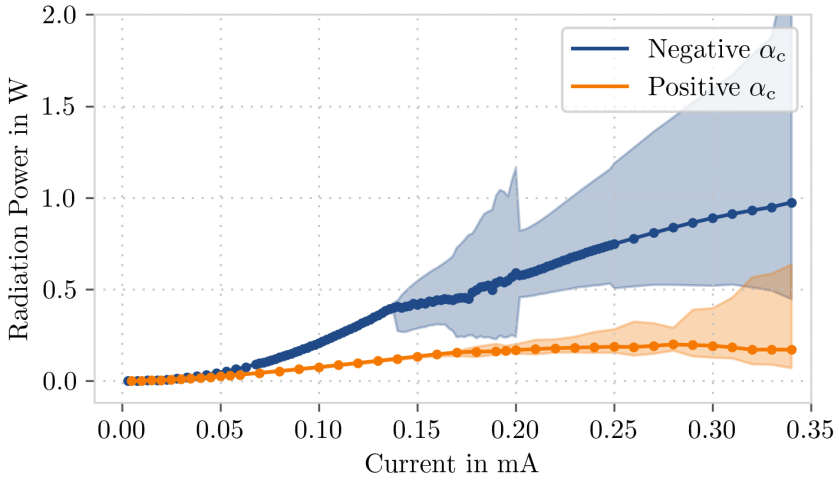

Figure 8.34: Radiation power simulated with Inovesa for positive and negative α_c with a value of $|\alpha| = 3.95 \times 10^{-4}$ at 1000 kV accelerating voltage. The solid lines indicate the mean values for each current. The top of the shaded areas marks the peak power per current and the bottom of the shaded areas marks the minimum per current. The data shown here is from the same simulations as used for figures 8.9 and 8.10.

The strong kink at negative α_c (at about 0.14 mA) suggests a significantly lowered mean radiation intensity with the instability compared to the expected intensity without the instability. As this kink is stronger at negative α_c, it might render the negative α_c regime an interesting candidate for control experiments that suppress the formation of substructures, for example using machine learning as done in [Bol21, Wan21]. The potential gain in CSR intensity if the instability could be suppressed would be substantial. Even if such control experiments would result in a mean intensity as seen with instability and not the expected intensity without instability, the achieved resulting intensity would be significantly higher for negative α_c compared to positive α_c.

In general, the negative α_c regime is a promising candidate to consider for experiments requiring high intensities of CSR. The simulations also show a more violent occurrence of substructures in the phase space density and longitudinal bunch profile at negative α_c compared to positive α_c. These structures, at times during bursts when they are strong, increase the form factor at corresponding frequencies in addition to the increase due to the shorter bunch length. Therefore, the radiation intensity measured in the frequency range corresponding to these substructures is increased further and the peak intensity overall increases. Even the mean intensity for negative α_c is higher than the peak intensity for positive α_c in both simulations and measurements. This significantly higher intensity makes the negative α_c regime particularly attractive to applications of

CSR at synchrotrons, especially as this could be used as an intense radiation source in the low THz range.

9 Summary and Conclusion

The perpetual improvements to synchrotron light sources and to the quality of the produced radiation require new approaches. As a result, new schemes are being considered for new and potential upgrades to existing machines mainly aiming towards ultra low emittances. One of these schemes, the use of multibend achromats, comes with the downside of a reduced dynamic aperture due to the necessity of strong sextupole magnets to keep the chromaticity positive. This can be circumvented through the usage of a negative momentum compaction factor optics which allows the operation with negative chromaticities and thus relaxed sextupole strengths.

In this thesis the impact of a switch in sign of α_c on the beam dynamics in a synchrotron light source has been studied. An optics with a negative momentum compaction factor has been successfully implemented at KARA for the first time. Based on this optics multiple measurements of the beam dynamics were performed and analysed.

For the implementation of the new optics the following hybrid approach between simulation and manual tuning of the optics was successfully employed. At first a low α_c optics was iteratively established while maintaining direct injection possible. From there a negative α_c optics was simulated based on the extrapolation of the necessary changes to magnet strengths from normal to low α_c. Using these simulations an optics with a negative momentum compaction factor was implemented in KARA and manually tuned and optimised for injection rate and accumulable beam current. Afterwards a successful ramping procedure to raise the beam energy to 1.3 GeV was established increasing the lifetime of the stored beam at negative α_c.

Subsequently, some basic properties of the beam and the optics have been studied. In order to allow injection into the negative α_c optics a negative chromaticity was necessary. In addition, the exact value of the chromaticity was found to only play a minor role for injection rate and accumulable beam current and can therefore be adjusted to other requirements. Studies on the higher orders of α_c, for optics with a positive and negative α_c, showed an influence of the sextupole strengths, defining the chromaticity, on the first and second order of α_c. Furthermore, it was found that the maximum beam current non-linearly depends on the number of bunches. The beam lifetime has been

measured for various values of the accelerating voltage as it influences the bunch length and Touschek losses. It was found to be higher for lower voltages and therefore longer bunches. In general, the beam lifetime was found to be shorter at negative α_c compared to positive α_c at KARA.

The transverse beam stability was investigated by observing the transverse beam position after an artificial horizontal excitation in the form of a kick. These investigations showed a damping of the excitations and a stable beam at positive α_c with positive chromaticities as well as at negative α_c with negative chromaticities. At positive α_c with negative chromaticities, however, increased oscillations were measured, with and without artificial excitation. This hints, as predicted, at the presence of undesired effects at negative chromaticities for positive α_c and the absence thereof for negative α_c and negative chromaticities. Therefore, stable operation at KARA with reduced sextupole strengths was successfully shown. Further analysis of the associated current-dependent damping time after the kick revealed indications for the presence of head-tail effects contributing to the damping of the oscillations.

A strong implication of the switched sign of α_c on the longitudinal beam dynamics was seen in the study of the current-dependent bunch length. Due to the required shift in acceleration phase on the accelerating voltage associated with the move from a positive to a negative sign of α_c the effective potential seen by the electrons is changed. This results in a generally shorter bunch length at negative α_c and furthermore in a different current-dependent behaviour. For low current a bunch shortening was observed while at positive α_c a monotone bunch length increase with current was measured. Simulations of this behaviour showed a good agreement to the measurements.

Analysing time resolved dynamics, particularly using the emitted radiation, a longitudinal instability was observed. This instability was studied and the behaviour compared to the equivalent instability at positive α_c, which is the so-called micro-bunching instability. This instability results from the interaction between the bunches with their own emitted coherent synchrotron radiation (CSR). The shift in the phase of the acceleration voltage leads to a reversed rotation of the charge density in the longitudinal phase space. Therefore, a different behaviour at positive α_c and negative α_c was to be expected. In both cases strong fluctuations in the emitted CSR intensity can be observed. Therefore, time and bunch current resolved measurements of the emitted coherent synchrotron radiation at positive and negative α_c were conducted to analyse the underlying dynamics. Based on the fast data acquisition system KAPTURE and a pre-existing method called snapshot measurements, a new measurement method called snapdecay measurements was developed. The method records the individual detector signal of all bunches each

containing an intentionally different bunch current. By repeating the measurement after a short delay, where the bunch currents naturally decrease ("decay"), the gaps in the bunch currents of the previous measurements are filled. This harvests the short measurement duration from the snapshot method while simultaneously increasing the resolution in bunch current.

These measurements revealed a current dependency of the behaviour of the instability. While this was previously seen at positive α_c the dependency at negative α_c was found to be systematically less complex and significantly more predictable with an almost constant behaviour over bunch current down to a specific bunch current where the instability shows a threshold. Nevertheless, similar regimes in the observed fluctuation frequencies between positive and negative α_c were identified. These fluctuation frequencies are the result of periodic outbursts of CSR intensity that can be observed in the time evolution of the CSR intensity at positive and negative α_c. The temporal structure of these outbursts however differs between the two signs. Additionally, at negative α_c the repetition rate is significantly lower. Measurements at different beam energies indicate an inverse dependency of the repetition rate to the damping time affected by the beam energy at negative α_c. At both signs of α_c the behaviour of the instability drastically changes at the lowest measured energy of 0.5 GeV.

Systematic studies of the instability threshold current for multiple values of α_c at two different accelerating voltages show a systematically lower threshold current at negative α_c compared to positive α_c. In addition, the dependence of the instability threshold current on the value of α_c was found to differ drastically between positive and negative α_c. Especially, the scaling law, established for positive α_c in literature, does not seem to describe the behaviour seen at negative α_c which shows a more complex dependency on the accelerating voltage.

In addition, a clear correlation between the emitted CSR intensity as well as the measured arrival time of the CSR pulse could be established. This correlation was inverse for positive α_c compared to negative α_c which can be explained by the different phase in acceleration voltage for the two operation modes. At negative α_c an increased CSR intensity was observed compared to positive α_c which can be explained by the shorter bunches leading to an increased charge density. The mean as well as the peak intensity was observed to be higher. Furthermore, for both signs of α_c it was seen that the increase in the mean intensity with bunch current is lower for currents above the instability threshold current. This gives rise to the assumption that a stabilisation of the instability could potentially increase the mean emitted CSR intensity especially at negative α_c.

In conclusion it can be said, the implementation of an optics with a negative momentum compaction factor at the accelerator test facility KARA was successful. It was possible to investigate the implications of the negative sign of α_c on beam dynamics. The results and gained insights can aid in the assessment of this regime for future synchrotron light sources. As a main motivation behind this thesis was to support future light sources and experiments, the central results and conclusions in this regard are addressed below.

Investigations of transverse beam stability showed a stable beam at negative α_c with negative chromaticities and further analysis of the associated current-dependent damping times indicated the cause to be head-tail damping effects. This supports the hypothesis that light sources can be successfully operated with negative chromaticities when operating at negative momentum compaction factors, thus easing the use of multibend achromats in future light sources.

Measurements of the current-dependent bunch length revealed a bunch shortening at low beam currents and more importantly an overall significantly shorter bunch length at negative α_c compared to positive α_c. While future machines that are limited in the charge density within the bunches might suffer from this and require additional measures to elongate bunches, machines that require shorter bunches, e.g. for the production of shorter light pulses, might benefit without additional requirements.

For the investigated longitudinal instability a lower threshold current and higher predictability of the fluctuation frequencies has been found at negative α_c compared to positive α_c. The lower threshold as well as the higher predictability should facilitate an easier utilisation of this instability for applications using the produced high intensity CSR in the THz range. Furthermore, a higher radiation intensity at negative α_c compared to positive α_c has been measured and a higher potential intensity gain has been revealed for feedback applications reducing the intensity fluctuations.

In conclusion, this thesis shows the validity of using negative momentum compaction factor optics to enable greatly reduced sextupole magnet strengths without risking beam loss due to the head-tail instability. The potentials as well as problems of this unconventional operation mode shown by the investigations provide important advancements towards utilising the negative momentum compaction factor optics for future synchrotron light sources.

A Appendix

A.1 Various Spectrograms at negative α_c

For the systematic determination of the threshold current as function of synchrotron frequency and α_c, multiple measurements were conducted. Some spectrograms corresponding to these measurements are shown here.

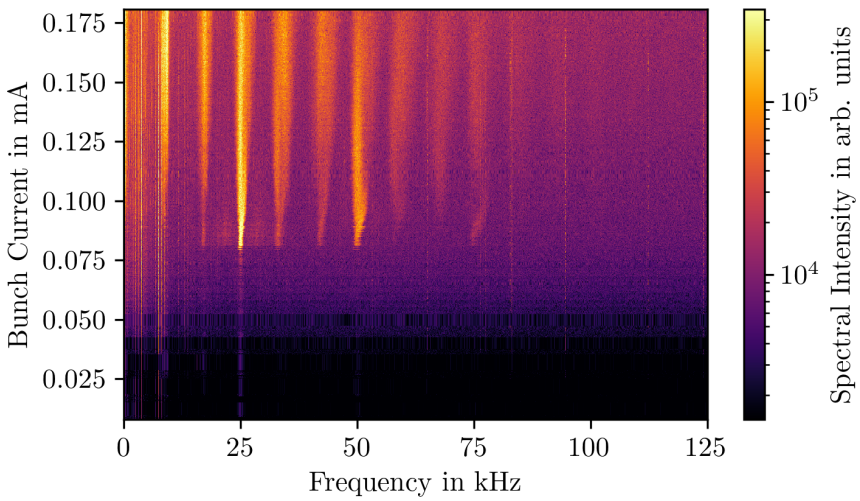

Figure A.1: CSR intensity fluctuation spectrogram measured at negative α_c for 1.3 GeV at an accelerating voltage of 1000 kV, $\alpha_c \approx -3.4 \times 10^{-4}$ and $f_s \approx 7.5$ kHz.

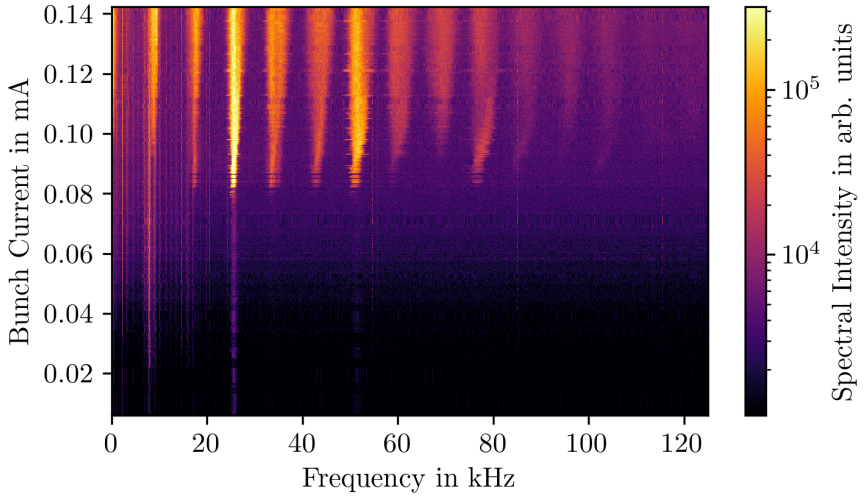

Figure A.2: CSR intensity fluctuation spectrogram measured at negative α_c for 1.3 GeV at an accelerating voltage of 1000 kV, $\alpha_c \approx -3.7 \times 10^{-4}$ and $f_s \approx 7.8$ kHz.

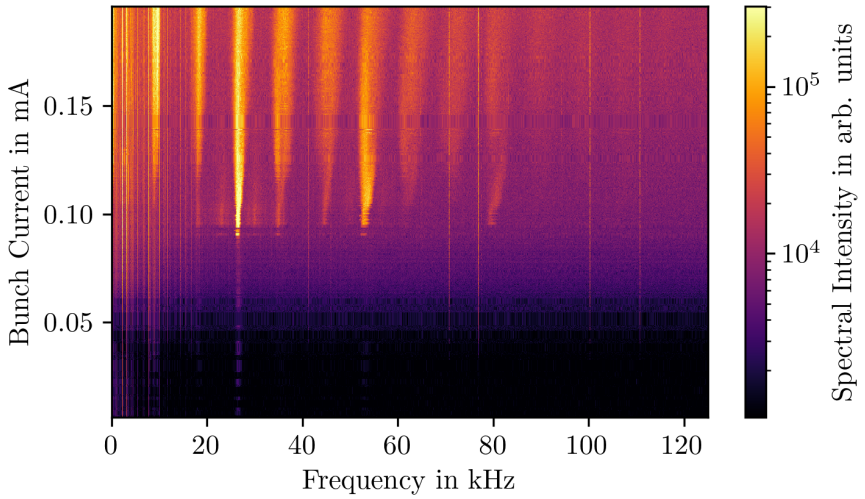

Figure A.3: CSR intensity fluctuation spectrogram measured at negative α_c for 1.3 GeV at an accelerating voltage of 1000 kV, $\alpha_c \approx -4.0 \times 10^{-4}$ and $f_s \approx 8.1$ kHz.

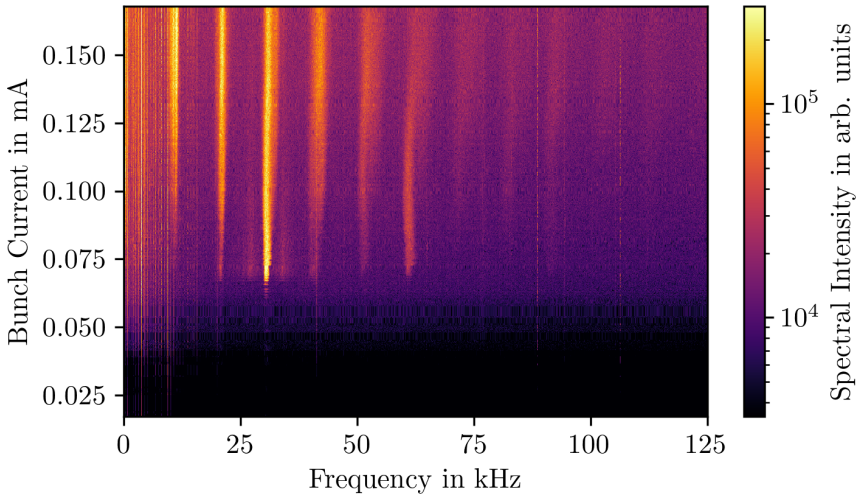

Figure A.4: CSR intensity fluctuation spectrogram measured at negative α_c for 1.3 GeV at an accelerating voltage of 1500 kV, $\alpha_c \approx -3.6 \times 10^{-4}$ and $f_s \approx 9.5$ kHz.

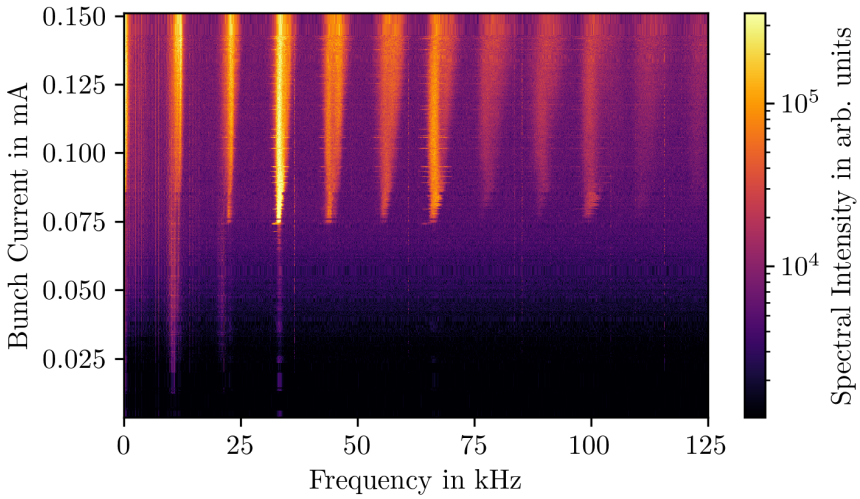

Figure A.5: CSR intensity fluctuation spectrogram measured at negative α_c for 1.3 GeV at an accelerating voltage of 1500 kV, $\alpha_c \approx -4.2 \times 10^{-4}$ and $f_s \approx 10.3$ kHz.

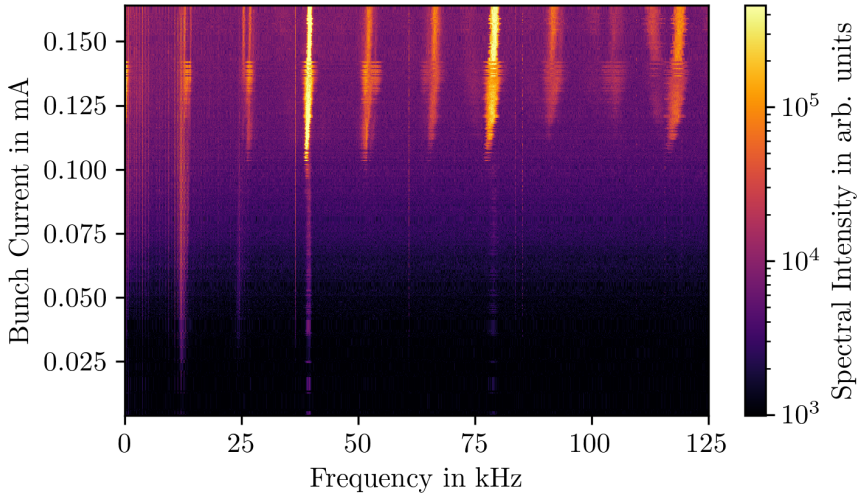

Figure A.6: CSR intensity fluctuation spectrogram measured at negative α_c for 1.3 GeV at an accelerating voltage of 1500 kV, $\alpha_c \approx -5.9 \times 10^{-4}$ and $f_s \approx 12.1$ kHz.

A.2 Vertical Structures in Spectrograms

At positive α_c and 0.9 GeV vertical structures are visible in the measured spectrogram in Fig. 8.20 in Section 8.6. Measurements at 1.3 GeV and positive α_c, however, also show these vertical lines in some measurements reaching to high bunch currents. An example is shown in Fig. A.7.

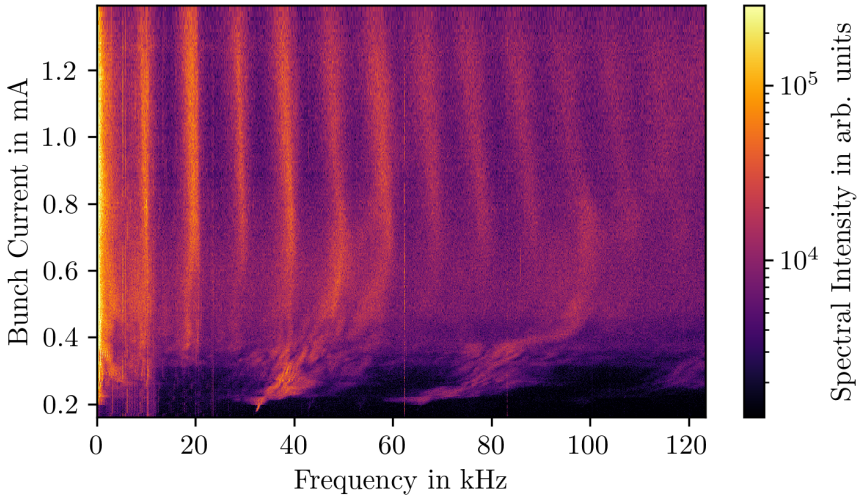

Figure A.7: CSR intensity fluctuation spectrogram measured at positive α_c for 1.3 GeV at an accelerating voltage of 1222 kV and $\alpha_c \approx 5.2 \times 10^{-4}$. Data courtesy of Miriam Brosi.

Publications

[Sch19a] Schönfeldt, P.; Schreiber, P.; Brosi, M.; Schestag, J.; Boltz, T.; Blaicher, M.; Gethmann, J. *Inovesa/Inovesa: Gamma Three*. Zenodo, Apr. 29, 2019. DOI: 10.5281/zenodo.2653504.

[Sch19b] Schreiber, P.; Boltz, T.; Brosi, M.; Härer, B.; Mochihashi, A.; Müller, A.-S.; Papash, A.; Schuh, M.: "Status of Operation With Negative Momentum Compaction at KARA". In: *Proc. of IPAC19*. Melbourne, Australia: JACoW Publishing, June 2019. Pp. 878–881. DOI: 10.18429/JACoW-IPAC2019-MOPTS017.

[Sch20] Schreiber, P.; Boltz, T.; Brosi, M.; Haerer, B.; Mochihashi, A.; Papash, A.; Schuh, M.; Müller, A.-S.: "Status of Negative Momentum Compaction Operation at KARA". In: *CERN Yellow Reports: Conference Proceedings*. Vol. 9. Dec. 16, 2020. 297 Pages. DOI: 10.23732/CYRCP-2020-009.297.

[Sch21] Schreiber, P.; Boltz, T.; Brosi, M.; Härer, B.; Mochihashi, A.; Müller, A.-S.; Papash, A.; Ruprecht, R.; Schuh, M.: "Effect of Negative Momentum Compaction Operation on the Current-Dependent Bunch Length". In: *Proc. of IPAC21*. JACoW Publishing, Geneva, Switzerland, Aug. 2021. Pp. 2786–2789. DOI: 10.18429/JACoW-IPAC2021-WEPAB083.

[Pap21a] Papash, A.; Brosi, M.; Huttel, E.; Mochihashi, A.; Müller, A.-S.; Ruprecht, R.; Schreiber, P.; Schuh, M.; Smale, N.: "Different Operation Regimes at the KIT Storage Ring KARA (Karlsruhe Research Accelerator)". In: *Proc. of IPAC21*. JACoW Publishing, Geneva, Switzerland, Aug. 2021. Pp. 163–166. DOI: 10.18429/JACoW-IPAC2021-MOPAB036.

[Pap21b] Papash, A.; Brosi, M.; Schreiber, P.; Boltz, T.; Smale, N.; Ruprecht, R.; Schuh, M.; Müller, A.-S.: "Alpha-Buckets in High Energy Electron Storage Rings (Review of Existing Experiments and Feasibility Studies for Future Developments)". *Advances in Theoretical & Computational Physics* 4, 2021. DOI: 10.33140/ATCP.04.02.08.

[Pap21c] Papash, A.; Boltz, T.; Brosi, M.; Müller, A.-S.; Ruprecht, R.; Schreiber, P.; Schuh, M.; Smale, N.: "On Possibility of Alpha-Buckets Detecting at the KIT Storage Ring KARA (Karlsruhe Research Accelerator)". In: *Proc. of IPAC21*. JACoW Publishing, Geneva, Switzerland, Aug. 2021. Pp. 167–170. DOI: 10.18429/JACoW-IPAC2021-MOPAB037.

[Bro19a] Brosi, M.; Boltz, T.; Bründermann, E.; Funkner, S.; Kehrer, B.; Müller, A.-S.; Nasse, M.; Niehues, G.; Patil, M.; Schreiber, P.; Schönfeldt, P.; Steinmann, J.: "Synchronous Measurements of Electron Bunches Under the Influence of the Microbunching Instability". In: *Proc. of IPAC19*. Melbourne, Australia: JACoW Publishing, June 2019. Pp. 3119–3122. DOI: 10.18429/JACoW-IPAC2019-WEPTS015.

[Sch22] Schreiber, P.; Boltz, T.; Brosi, M.; Haerer, B.; Mochihashi, A.; Papash, A.; Schuh, M.; Müller, A.-S.: "Influence of Negative Momentum Compaction Factors on Longitudinal Beam Dynamics in an Electron Synchrotron". *to be published*, 2022.

[Bol19] Boltz, T.; Brosi, M.; Bründermann, E.; Härer, B.; Müller, A.-S.; Schreiber, P.; Schönfeldt, P.; Yan, M.: "Perturbation of Synchrotron Motion in the Micro-Bunching Instability". In: *Proc. of IPAC19*. Melbourne, Australia: JACoW Publishing, June 2019. Pp. 108–111. DOI: 10.18429/JACoW-IPAC2019-MOPGW018.

[Bro19b] Brosi, M.; Steinmann, J. L.; Blomley, E.; Boltz, T.; Bründermann, E.; Gethmann, J.; Kehrer, B.; Mathis, Y.-L.; Papash, A.; Schedler, M.; Schönfeldt, P.; Schreiber, P.; Schuh, M.; Schwarz, M.; Müller, A.-S.; Caselle, M.; Rota, L.; Weber, M.; Kuske, P.: "Systematic Studies of the Microbunching Instability at Very Low Bunch Charges". *Physical Review Accelerators and Beams* 22, p. 020701, 2019. DOI: 10.1103/PhysRevAccelBeams.22.020701.

[Bro20b] Brosi, M.; Blomley, E.; Boltz, T.; Bründermann, E.; Caselle, M.; Gethmann, J.; Kehrer, B.; Papash, A.; Rota, L.; Schönfeldt, P.; Schreiber, P.; Schuh, M.; Schwarz, M.; Steinmann, J.; Weber, M.; Müller, A.-S.: "Systematic Studies of the Microbunching and Weak Instability at Short Bunch Lengths". *CERN Yellow Reports: Conference Proceedings* Vol. 9, 335 Pages, 2020. DOI: 10.23732/CYRCP-2020-009.335.

[Bro18] Brosi, M.; Gethmann, J.; Bernhard, A.; Kehrer, B.; Papash, A.; Schönfeldt, P.; Schreiber, P.; Steinmann, J. L.; Müller, A.-S.: "Studies of the Micro-Bunching Instability in the Presence of a Damping Wiggler". *Journal of*

Physics: Conference Series 1067, p. 062017, 2018. DOI: 10.1088/1742-6596/1067/6/062017.

[Bro21b] Brosi, M.; Schreiber, P.; Schuh, M.; Müller, A.-S.: "Influence of Different Beam Energies on the Micro-Bunching Instability". In: *Proc. of IPAC21*. JACoW Publishing, Geneva, Switzerland, Aug. 2021. Pp. 3209–3212. DOI: 10.18429/JACoW-IPAC2021-WEPAB246.

[Bol21] Boltz, T.; Blomley, E.; Brosi, M.; Bründermann, E.; Härer, B.; Mochihashi, A.; Müller, A.-S.; Schreiber, P.; Schuh, M.; Yan, M.: "Excitation of Micro-Bunching in Short Electron Bunches Using RF Amplitude Modulation". In: *Proc. of IPAC21*. JACoW Publishing, Geneva, Switzerland, Aug. 2021. Pp. 3173–3176. DOI: 10.18429/JACoW-IPAC2021-WEPAB233.

[Wan21] Wang, W.; Caselle, M.; Boltz, T.; Blomley, E.; Brosi, M.; Dritschler, T.; Ebersoldt, A.; Kopmann, A.; Garcia, A. S.; Schreiber, P.; Weber, E. B. M.; Muller, A.-S.; Fang, Y.: "Accelerated Deep Reinforcement Learning for Fast Feedback of Beam Dynamics at KARA". *IEEE Transactions on Nuclear Science*, pp. 1–1, 2021. DOI: 10.1109/TNS.2021.3084515.

Bibliography

[1] Eriksson, M.: "The Multi-Bend Achromat Storage Rings". In: New York, NY USA, 2016. P. 020001. DOI: 10.1063/1.4952780.

[2] Martin, I. P. S. et al.: "Experience with Low-Alpha Lattices at the Diamond Light Source". *Physical Review Special Topics - Accelerators and Beams* 14, p. 040705, 2011. DOI: 10.1103/PhysRevSTAB.14.040705.

[3] Feikes, J. et al.: "Specific Operation Modes at the Metrology Light Source". *Proc. of IPAC16*, 2016. DOI: 10.18429/JACOW-IPAC2016-WEPOW008.

[4] Nadji, A. et al.: "Experiments with Low and Negative Momentum Compaction Factor with Super-ACO". *Proc. of EPAC96*, 1996. URL: http://accelconf.web.cern.ch/Accelconf/e96/PAPERS/WEPG/WEP090G.PDF.

[5] Wille, K.: *Physik Der Teilchenbeschleuniger Und Synchrotronstrahlungsquellen*. Teubner Studienbücher Physik. Wiesbaden: Vieweg+Teubner Verlag, 1996. DOI: 10.1007/978-3-663-11039-2.

[6] Wiedemann, H.: *Particle Accelerator Physics*. Graduate Texts in Physics. Cham: Springer International Publishing, 2015. DOI: 10.1007/978-3-319-18317-6.

[7] Jackson, J. D.: *Classical Electrodynamics*. 3rd ed. New York: Wiley, 1999. 808 pp. ISBN: 978-0-471-30932-1.

[8] Sands, M. *The Physics of Electron Storage Rings: An Introduction*. SLAC-R-121, 1453884. Nov. 1970. DOI: 10.2172/1453884.

[9] Steinmann, J. L.: "Diagnostics of Short Electron Bunches with THz Detectors in Particle Accelerators". PhD thesis. Karlsruhe Institute of Technology, 2019. DOI: 10.5445/KSP/1000090017.

[10] Chao, A. W. et al.: *Handbook of Accelerator Physics and Engineering*. 2nd ed. WORLD SCIENTIFIC, May 2013. DOI: 10.1142/8543.

[11] Schönfeldt, P.: "Simulation and Measurement of the Dynamics of Ultra-Short Electron Bunch Profiles for the Generation of Coherent THz Radiation". PhD thesis. Karlsruhe Institute of Technology, 2018. DOI: 10.5445/IR/1000084466.

[12] Cai, Y.: "Theory of Microwave Instability and Coherent Synchrotron Radiation in Electron Storage Rings". In: *Proc. of IPAC11*. JACoW Publishing, 2011. P. 3774.

[13] *Karlsruhe Research Accelerator (KARA)*. KIT - IBPT - Discover - Test Facilities - KARA. URL: https://www.ibpt.kit.edu/kara.php (visited on 01/25/2022).

[14] Blomley, E.: "Investigation and Control of Beam Instabilities at the Karlsruhe Research Accelerator Using a 3-D Digital Bynch-By-Bunch Feedback System". PhD thesis. Karlsruhe Institute of Technology, 2021. DOI: 10.5445/IR/1000137621.

[15] Kramer, S. L.: "Direct Observation of Beam Impedance above Cutoff". *Physical Review Special Topics - Accelerators and Beams* 5, p. 112001, 2002. DOI: 10.1103/PhysRevSTAB.5.112001.

[16] Papash, A. et al.: "New Operation Regimes at the Storage Ring KARA at KIT". In: *Proc. of IPAC19*. Melbourne, Australia: JACoW Publishing, June 2019. Pp. 1422–1425. DOI: 10.18429/JACoW-IPAC2019-TUPGW016.

[17] Klein, M. et al.: "Modeling the Low-Alpha-Mode at ANKA with the Accelerator Toolbox". In: *Proc. of PAC11*. Mar.-Apr. 2011. New York, USA. URL: https://accelconf.web.cern.ch/AccelConf/PAC2011/papers/WEP005.PDF.

[18] Huttel, E. et al.: "Operation with a Low Emittance Optics at ANKA". In: *Proc. of PAC05*. 2005. Pp. 2467–2469. URL: https://accelconf.web.cern.ch/p05/PAPERS/RPAE037.PDF.

[19] Papash, A. et al.: "High Order Magnetic Field Components and Non-Linear Optics at the ANKA Storage Ring". In: *Proc. of IPAC17*. Copenhagen, Denmark: JACoW Publishing, May 2017. Pp. 2586–2588. DOI: 10.18429/JACoW-IPAC2017-WEPAB011.

[20] Müller, A. S. et al.: "Experimental Aspects of CSR in the ANKA Storage Ring". *ICFA Beam Dyn. Newslett.* 57, pp. 154–165, 2012. URL: https://icfa-usa.jlab.org/archive/newsletter/icfa_bd_nl_57.pdf.

[21] Streun, A. *OPA*. Version 3.39. Mar. 14, 2012. URL: https://ados.web.psi.ch/opa/opa.pdf.

[22] Gethmann, J.: "Systematic Studies of the Beam Dynamics with a Superconducting Damping Wiggler at KARA". PhD thesis. Karlsruhe Institute of Technology, 2021. DOI: 10.5445/IR/1000137351.

[23] *Dimtel, Inc.* URL: https://www.dimtel.com/ (visited on 09/03/2021).

[24] *Ocelot*. URL: https://github.com/ocelot-collab/ocelot.

[25] *MAD-X*. URL: http://madx.web.cern.ch/madx/.

[26] Brosi, M.: "In-Depth Analysis of the Micro-Bunching Characteristics in Single and Multi-Bunch Operation at KARA". PhD thesis. Karlsruhe Institute of Technology, 2020. DOI: 10.5445/IR/1000120018.

[27] Brosi, M. et al.: "Fast Mapping of Terahertz Bursting Thresholds and Characteristics at Synchrotron Light Sources". *Physical Review Accelerators and Beams* 19, p. 110701, 2016. DOI: 10.1103/PhysRevAccelBeams.19.110701.

[28] Schönfeldt, P. et al.: "Fluctuation of Bunch Length in Bursting CSR: Measurement and Simulation". In: *Proc. of IPAC14*. JACOW Publishing, Geneva, Switzerland, July 2014. Pp. 237–239. DOI: 10.18429/JACoW-IPAC2014-MOPRO068.

[29] Chang, C.: "Precise Determination of the Electron Beam Energy with Compton Backscattered Laser Photons at ANKA". PhD thesis. Karlsruhe Institute of Technology, 2016. DOI: 10.5445/IR/1000051914.

[30] Einfeld, D.: "Entwurf und Aufbau des Speicherrings ANKA". 2001. DOI: 10.5445/IR/120049066.

[31] *Bergoz Instrumentation*. High-precision current transformers and analog electronics. URL: https://www.bergoz.com/ (visited on 12/20/2021).

[32] Lee, S. Y.: *Accelerator Physics*. 3rd ed. World Scientific, Nov. 2011. DOI: 10.1142/8335.

[33] Mahgoub, M. et al.: "Longitudinal Phase Space Studies at the PITZ Facility". In: *Proc. of IPAC12*. JACoW Publishing, May 2012. Pp. 631–633.

[34] *ACST GmbH*. ACST GmbH | Technology solutions for terahertz electronics. URL: https://acst.de/ (visited on 08/26/2021).

[35] Caselle, M. et al.: "A Picosecond Sampling Electronic 'kapture' for Terahertz Synchrotron Radiation". In: *Proc. of IBIC14*. JACoW Publishing, 2015. Pp. 24–28. ISBN: 978-3-95450-141-0.

[36] Caselle, M. et al.: "KAPTURE-2. A Picosecond Sampling System for Individual THz Pulses with High Repetition Rate". *Journal of Instrumentation* 12, p. C01040, 2017. DOI: 10.1088/1748-0221/12/01/c01040.

[37] Steinmann, J. L. et al.: "Continuous Bunch-by-Bunch Spectroscopic Investigation of the Microbunching Instability". *Physical Review Accelerators and Beams* 21, p. 110705, 2018. DOI: 10.1103/PhysRevAccelBeams.21.110705.

[38] Brosi, M.: “Overview of the Micro-Bunching Instability in Electron Storage Rings and Evolving Diagnostics”. In: *Proc. of IPAC21*. JACoW Publishing, Geneva, Switzerland, Aug. 2021. Pp. 3686–3691. DOI: 10.18429/JACoW-IPAC2021-THXA02.

[39] Kehrer, B. et al.: “Filling Pattern Measurements Using Dead-Time Corrected Single Photon Counting”. In: *Proc. of IPAC18*. JACoW Publishing, 2018. DOI: 10.18429/JACOW-IPAC2018-WEPAL027.

[40] *idQuantique*. idQuantique. URL: http://idquantique.com.

[41] *PicoQuant*. PicoQuant. URL: http://picoquant.com.

[42] Kehrer, B. et al.: “Visible Light Diagnostics at the ANKA Storage Ring”. In: *Proc. of IPAC15*. JACoW Publishing, 2015. DOI: 10.18429/JACOW-IPAC2015-MOPHA037.

[43] Hope, G. *Fsinc: Fast Sinc Transform Implementation in Python*. URL: https://github.com/gauteh/fsinc (visited on 12/20/2021).

[44] Whittaker, E. T.: “XVIII.—On the Functions Which Are Represented by the Expansions of the Interpolation-Theory”. *Proceedings of the Royal Society of Edinburgh* 35, pp. 181–194, 1915. DOI: 10.1017/S0370164600017806.

[45] Schönfeldt, P. et al.: “Parallelized Vlasov-Fokker-Planck Solver for Desktop Personal Computers”. *Physical Review Accelerators and Beams* 20, p. 030704, 2017. DOI: 10.1103/PhysRevAccelBeams.20.030704.

[46] Ng, K.-Y.: *Physics of Intensity Dependent Beam Instabilities*. Hackensack, N.J: World Scientific, 2006. 776 pp. ISBN: 978-981-256-342-2.

[47] Khronos Group. *OpenCL*. URL: https://www.khronos.org/opencl/.

[48] Paterson, J. M.: “The ’Head-Tail’ Instability”. *IEEE Transactions on Nuclear Science* 20, pp. 850–850, 1973. DOI: 10.1109/TNS.1973.4327262.

[49] Chao, A. W.: *Physics of Collective Beam Instabilities in High Energy Accelerators*. Wiley Series in Beam Physics and Accelerator Technology. New York: Wiley, 1993. ISBN: 978-0-471-55184-3.

[50] Gareyte, J.; Sacherer, F. J.: “Head-Tail Type Instabilities in the CERN PS and Booster”. 5 p, 1974. URL: http://cds.cern.ch/record/322647.

[51] Heifets, S.; Novokhatski, A.: “Coherent Beam Stability in the Low Momentum Compaction Lattice”. *Physical Review Special Topics - Accelerators and Beams* 9, p. 044402, 2006. DOI: 10.1103/PhysRevSTAB.9.044402.

[52] Rakowsky, G.; Hughey, L. R.: "SURF's up at NBS: A Progress Report". *IEEE Transactions on Nuclear Science* 26, pp. 3845–3847, 1979. DOI: 10.1109/TNS.1979.4330628.

[53] Arp, U. et al.: "Spontaneous Coherent Microwave Emission and the Sawtooth Instability in a Compact Storage Ring". *Physical Review Special Topics - Accelerators and Beams* 4, p. 054401, 2001. DOI: 10.1103/PhysRevSTAB.4.054401.

[54] Hosaka, M. et al.: "Longitudinal Beam Dynamics on an Electron Storage Ring with Negative Momentum Compaction Factor". In: *Proc. of APAC98*. JACoW Publishing, 1998. URL: https://accelconf.web.cern.ch/a98/APAC98/5D018.PDF.

[55] Shields, W. et al.: "Microbunch Instability Observations from a THz Detector at Diamond Light Source". *Journal of Physics: Conference Series* 357, p. 012037, 2012. DOI: 10.1088/1742-6596/357/1/012037.

[56] Judin, V.: "Untersuchung von Bunch-Bunch-Wechselwirkungen und des Einflusses der geometrischen Impedanz bei der Erzeugung kohärenter THz-Strahlung". PhD thesis. Karlsruhe Institute of Technology, 2013. DOI: 10.5445/IR/1000039528.

[57] Martin, I. P. S.; Thomas, C. A.; Bartolini, R.: "Modelling the Steady-State CSR Emission in Low Alpha Mode at the Diamond Storage Ring". In: *Proc. of IPAC12*. JACoW Publishing, May 2012. Pp. 1677–1679. URL: https://accelconf.web.cern.ch/IPAC2012/papers/tuppp031.pdf.

[58] Wüstefeld, G.; Feikes, J.; Hartrott, M. V.: "Coherent THz Measurements at the Metrology Light Source". In: *Proc. of IPAC10*. 2010. P. 3. URL: http://accelconf.web.cern.ch/IPAC10/papers/wepea015.pdf.

[59] Bane, K. L. F.; Cai, Y.; Stupakov, G.: "Threshold Studies of the Microwave Instability in Electron Storage Rings". *Physical Review Special Topics - Accelerators and Beams* 13, 2010. DOI: 10.1103/PhysRevSTAB.13.104402.

[60] Ries, M.: "Nonlinear Momentum Compaction and Coherent Synchrotron Radiation at the Metrology Light Source". PhD thesis. Humboldt-Universität zu Berlin, Mathematisch-Naturwissenschaftliche Fakultät I, 2014. DOI: http://dx.doi.org/10.18452/16979.

[61] Kuske, P.: "Short Bunches at the Transition from Strong to Weak Longitudinal Instability". In: *Proc. of IPAC17*. JACoW Publishing, May 2017. Pp. 3696–3699. DOI: doi:10.18429/JACoW-IPAC2017-THPAB007.

[62] Martin, I. et al.: “Reconstruction of Electron Bunch Motion During CSR Bursts Using Synchronised Diagnostics”. In: *Proc. of IPAC15*. JACoW Publishing, June 2015. Pp. 529–532. DOI: 10.18429/JACoW-IPAC2015-MOPMA003.

[63] Hiller, N. et al.: “A Setup for Single Shot Electro Optical Bunch Length Measurements at the ANKA Storage Ring”. In: *Proc. of IPAC11*. JACoW Publishing, 2011. URL: http://accelconf.web.cern.ch/AccelConf/IPAC2011/papers/tupc086.pdf.

[64] Judin, V. et al.: “Bursting Patterns of Coherent Synchrotron Radiation in the ANKA Storage Ring”. In: *Proc. of IPAC13*. JACoW Publishing, May 2013. Pp. 2516–2518. URL: https://jacow.org/IPAC2013/papers/WEPEA011.pdf.

[65] Martin, I. P. S. *Personal Communication at IPAC21*. May 5, 2021.

Acknowledgements

This thesis would not have been possible without the wonderful support of many people. I would like to use this chapter to thank everyone involved.

First of all, I want to thank Prof. Dr. Anke-Susanne Müller for allowing and enabling me to work on this thesis, for providing me with this interesting topic and for her supervision during my time at KARA. It was great to have the chance to freely work on and modify (at least the optics) such a fascinating and complex machine as KARA.

Furthermore, I want to thank Prof. Dr. Günter Quast who kindly accepted the duty of co-referent, especially for the very pleasant and calming discussion during the stressful time towards the end of my thesis.

I would like to thank Robert Ruprecht for his support in administrative matters and proofreading my publications especially his guidance on correct political wording in publications.

Further thanks I would like to extend to the graduate school KSETA providing me with contact to other PhD students and the opportunity to visit many courses on various scientific topics.

The work in the THz group provided me with a very engaging and fun working environment for which I am very grateful. Thanks to Akira Mochihashi, for always providing support during machine physics shifts for KARA as well as the streak camera, his work on the ARIES project, interesting discussions and for always considering me in the machine physics planning. Edmund Blomley provided me with insights in the BBB system, EPICS controlsystem and was always available for questions. Johannes Steinmann could always answer my questions regarding electronics and signal processing. For everything around the PicoHarp system Benjamin Kehrer was always available for discussions and optimisations. Furthermore, he always had a pun on his lips cheering up the work environment. A lot of simulations would not have been possible without the support of Patrik Schönfeldt and his creation (Inovesa) and his help to get me knowledgeable on the code. Also, a big thanks to Tobias Boltz for always lending a second pair of eyes and hands during the initial implementation phase of the negative α_c operation and for tirelessly optimising the corrector magnets.

A lot of support I received from Alexander Papash during the implementation phase of the negative α_c optics. He supported me with simulations and theoretical considerations, always considered my wild theories on lifetime etc. and pushed me for publications. He was often available for night shifts, and we had many pleasant discussions.

A lot of thanks to Marcel Schuh for his support and his help during machine physics shifts. He was always available when KARA refused to cooperate and we had many discussions on all possible topics.

Special thank also to my supervisor, Bastian Härer, for always having my back and tremendous support especially during the writing phase. He always pushed me to be confident about the significance of my results.

Extra thanks to Miriam Brosi, who supported me basically throughout the entire thesis, during most of the measurement shifts, night and day, for countless discussions and for her continuous reassurance, that I am on the right track.

Last but not least I want to thank my family. They enabled me to study physics in the first place, always encouraged me to follow my interests and provided a safe and relaxed haven to come back to. I can always rely on welcome distractions such as discussions on law, projects around the house and holidays. Thanks for always being there for me!

To everyone directly or indirectly involved: **Thank You!**